Probabilistic Fatigue Damage Diagnostics and Prognostics for Metallic and Composite Materials

by

Tishun Peng

A Dissertation Presented in Partial Fulfillment
of the Requirements for the Degree
Doctor of Philosophy

Approved May 2016 by the
Graduate Supervisory Committee:

Yongming Liu, Chair
Aditi Chattopadhyay
Marc Mignolet
Antonia Papandreou-Suppappola
Pingbo Tang

ARIZONA STATE UNIVERSITY

August 2016

ABSTRACT

In-situ fatigue damage diagnosis and prognosis is a challenging problem for both metallic and composite materials and structures. There are various uncertainties arising from material properties, component geometries, measurement noise, feature extraction techniques, and modeling errors. It is essential to manage and incorporate these uncertainties in order to achieve accurate damage detection and remaining useful life (RUL) prediction.

The aim of this study is to develop an integrated fatigue damage diagnosis and prognosis framework for both metallic and composite materials. First, Lamb waves are used as the in-situ damage detection technique to interrogate the damaged structures. Both experimental and numerical analysis for the Lamb wave propagation within aluminum are conducted. The RUL of lap joints under variable and constant fatigue loading is predicted using the Bayesian updating by incorporating damage detection information and various sources of uncertainties. Following this, the effect of matrix cracking and delamination in composite laminates on the Lamb wave propagation is investigated and a generalized probabilistic delamination size and location detection framework using Bayesian imaging method (BIM) is proposed and validated using the composite fatigue testing data. The RUL of the open-hole specimen is predicted using the overall stiffness degradation under fatigue loading. Next, the adjoint method-based damage detection framework is proposed considering the physics of heat conduction or elastic wave propagation. Different from the classical wave propagation-based method, the received signal under pristine condition is not necessary for estimating the damage information. This method can be successfully used for arbitrary damage location and shape profiling for any materials with higher accuracy

and resolution. Finally, some conclusions and future work are generated based on the current investigation.

DEDICATION

To my Family

ACKNOWLEDGMENTS

I would like to express my deepest gratitude to my advisor, Dr. Yongming Liu, who supports my Ph.D. study at Arizona State University. It is Dr. Liu's inspiration, encouragement, support and understanding that help me get through all the difficulties I came across during research and life. What I have learned from him are not just skills that can contribute to my career, but also personalities that make me a better person.

I would like to give my special thanks to my special family. It is the patience, understanding of my family that allow me to fully concentrate on my research.

I want to thank my committee members, Dr. Chattopadhyay, Dr. Mignolet, Dr. Papandreou, and Dr. Tang. Thanks to the invaluable advice and comments from them that help me to improve my dissertation.

I also would like to thank all of my group members. It is their kind help and invaluable comments that make my papers and dissertation better.

Special thanks to the collaborators, Kai Goebel and Abhinav Saxena, at NASA Ames for their tremendous help and encouragement during my research.

Finally, I would like to express my most sincere love and gratitude to my fiancée, Yan Chen. During my PhD study, she always gave me the warmest support and understanding.

The research reported in this dissertation was partially supported by the NASA project under NRANNX09AY54A and by NASA through Global Engineering and Materials, Inc. (GEM) under the project NNX12CA86C. The support is gratefully acknowledged.

The work was also partially sponsored by the DOT-PHMSA through CAAP and core research programs. I really appreciate the encouragement and technical comments from program managers James Merritt (DOT) and Ernest Lever (GTI).

TABLE OF CONTENTS

Page

LIST OF TABLES

LIST OF FIGURES

Figure Page

Figure Page

Figure Page

Figure Page

Figure Page

Figure Page

1 INTRODUCTION

1.1 Background

Damage can be induced by fatigue, impact, creep or other mechanical loadings during the service of engineering structures, such as bridges, rotorcrafts, aircrafts and space vehicles. Aluminum alloy and composites are widely used in these structures because of their high strength, low weight, and long durability. For metallic materials, such as aluminum or steel, fatigue is the most common failure pattern. For composite materials, the delamination and matrix cracking detection induced by fatigue or impact loading is still an important and challenging issue. Structural health monitoring (SHM) and non-destructive evaluation (NDE) of the current fatigue damage information will avoid significant catastrophic event in many critical systems by performing early prevention or unit replacement.

Because of the small length scale and possible embedded nature of these fatigue damage, visual inspection is not able to detect it easily and, therefore, nondestructive evaluation (NDE) techniques are generally used and extensively investigated for this type of diagnosis problems in metallic and composite materials. Currently, there are many non-destructive techniques (NDT) available for damage diagnosis, such as thermography [1, 2], ultrasonic techniques [3], X-ray [4], and eddy currents [5, 6]. Lamb wave-based structural health monitoring techniques are also widely investigated for the in-situ damage diagnostics. There are two detection techniques that are commonly used in practice, that are pulse-echo method and pitch-catch method [7]. Pulse-echo technique is usually employed to detect the damage position using triangulation [8, 9]. Pitch-catch technique can be used to detect the damage size when prior knowledge about damage is obtained [10]. Simultaneous location and size detection framework is desired by extracting the damage

information from the received sensor signal. In addition, most existing damage detection method cannot systematically include the uncertainties, such as measurement uncertainty and detection model uncertainty.

Lamb wave-based detection technique can be successfully used for 1D (e.g. crack), 2D (e.g. delamination) and single damage detection. Generally speaking, the damage in an arbitrary object can be three dimensional, with arbitrary shapes and at multiple locations. It would be extremely difficult to detect these kinds of damages using such a technique based solely on signal processing and feature extraction. Most existing methods also require the wave propagation information under the pristine condition and damage identification features are usually obtained by comparing the received signal between pristine and damaged conditions. For most practical cases, the wave propagation under the pristine condition may not be available for comparison. Some baseline free techniques, such as X-ray or eddy current are not extensively used because of their high cost and complexity in field applications. Conceptually, more damage information can be extracted from the received signal if the physics of the physical phenomenon is incorporated instead of only considering the waveform change. Therefore, more robust, economical, and generalized damage diagnosis technique should be developed to detect the damage with more generalized configuration by considering the physics of the physical phenomenon.

From the prognosis point of view, prediction of the remaining useful life (RUL) should be continuously updating by incorporating the current damage diagnosis information and other sources of uncertainties, such as mechanism model uncertainty, modeling parameters uncertainty, and future loading uncertainty. Bayesian theorem [11-13] plays an important role in the uncertainty management. It has been extensively used for prognosis in various

engineering fields [14] [15]. The Bayes' theorem allows updating the distribution of parameters of interest based on the condition monitoring system responses, which may come from the damage diagnosis model. The posterior distribution of the parameters can be obtained by combining its prior information and the current system response. More accurate RUL prediction and health management can be achieved by considering the updated physics model and structure heath state.

Because of the complexity of the posterior marginal from Bayesian updating, it is generally required to generate samples from the target distribution. Many Monte Carlo-based sampling algorithms have been used for this purpose since the analytical solution is not available for most engineering problems. Importance sampling method is able to generate samples from a similar distribution rather than the target distribution for which direct sampling is difficult [16-19]. The generated samples are corrected using the weight given by the ratio between the target distribution and the sampling distribution. It is very difficult to find the similar distribution if very little information is known about the problem. As an alternative sampling method, Metropolis-Hastings(M-H) algorithm was first proposed by Metropolis et al. and later extended by Hasting to a more general case [20, 21]. In this algorithm, a candidate is generated sequentially from the previous state using a proposed random walk. The sample is either accepted or rejected based on the computed metropolis ratio. There are several modified versions of M-H sampling algorithm, which are achieved by combining with the Delay Rejection[22, 23], the Adaptive Metropolis[24, 25], or the DRAM[26]. Delay rejection method generates another sample using a different proposal when a candidate is rejected, which may increase the acceptance ratio and sampling efficiency. Adaptive method makes use of the past Markov chain to adaptively

compute the Gaussian proposal distribution, which typically results in a faster convergence of the Markov chain. These modified M-H sampling algorithms can keep the ergodic properties of Markov chain and achieve higher efficiency. The choice a particular algorithm for generating samples depends highly on the nature of the problem. In this dissertation, the classical M-H samples algorithm is used to generate samples from the posterior distribution of Bayesian theorem.

1.2 Research Objectives

The objective of this study is to propose a probabilistic fatigue damage diagnosis and prognosis framework, in which both metallic and composite materials are investigated numerically and experimentally. The experimental results will be used as the validation for finite element simulation and ground truth measurement for proposed fatigue damage diagnosis method. A more advanced damage detection technique is proposed to extend the application fields and improve accuracy and resolution comparing with existing techniques.

The whole task can be organized as five chapters and presented in the rest of the dissertation:

In CHAPTER 2, the fatigue crack growth on the metallic material (e.g. lap joints) is monitored using Lamb wave-based damage detection method. Based on the diagnosis results, the remaining useful life (RUL) is predicted by considering various sources of uncertainties. The prognosis performance is validated using prognosis metrics, such as such as Prognostic Horizon (PH), $\alpha - \lambda$ accuracy. This deterministic crack diagnosis method is extended to simultaneously detect the crack size and location considering various sources of uncertainties using numerical simulation results.

In CHAPTER 3, a finite element model is built to investigate the delamination and

matrix cracking effect on Lamb wave propagation. Damage identification features are extracted from the numerical simulation and compared with the experimental datasets for validation. With the comprehensive understanding of Lamb wave propagation within composites, a Bayesian imaging method (BIM) is proposed to simultaneously detect the delamination size and location based on the Lamb wave signals. To predict the fatigue life of composite materials, an in-situ RUL prognosis framework is proposed based on the overall stiffness degradation of the open-hole specimen. It overcomes the difficulties for explicitly incorporate the detected damage into prognosis framework and is more efficient for real time fatigue life prognosis.

In CHAPTER 4, a more robust and accurate damage diagnosis technique is proposed based on the adjoint formulation. The adjoint method derivation for detecting the heat source location, thermal conductivity, and shear modulus is provided. This developed method can be successfully applied for detecting arbitrary damage configurations in metallic and composite materials. Multiple damage diagnosis can also be successfully achieved by considering physics of wave propagation and heat transfer.

In CHAPTER 5, some conclusions and future research directions are given based on the current study on the probabilistic damage diagnosis and prognosis for both metallic and composite materials.

2 FATIGUE DAMAGE DIAGNOSIS AND PROGNOSIS FOR METALLIC MATERIALS

2.1 Introduction

For metallic structures, fatigue failure is one of the most common failure modes and has significant impact on structure integrity. Fatigue damage diagnosis and even prognosis remains a challenging problem. Due to the invisibility property, the initial small crack is difficult to be detected. It makes it even harder if these cracks comes with the intrinsic material defects, or manufacturing treatments.

Recently, piezoelectric (PZT) ceramic wafers have been extensively used to generate Lamb waves because of its low cost and efficiency characteristics. It is well known that multiple modes will be generated when interacting with the boundaries of flaws [27-30]. It becomes more severe for the lap joint case, because the received signal is polluted by the echoes from the cracks and rivets. Besides that, multiple cracks may appear for a particular specimen and crack may initiate at different locations for different specimens. In this study, damage features are extracted from the received Lamb wave signals using an advanced signal-processing algorithms and these features are combined to reduce the uncertainties introduced by the crack initiation location and boundary reflection. In order to predict the RUL of lap joints, multiple uncertainties, such as measurement uncertainty, model parameter uncertainty, and detection model uncertainty are managed by the Bayesian inference framework.

2.2 Fatigue Testing for Lap Joints

In this section, the whole procedure of lap joint testing is presented and several damage diagnosis models are compared with experimental observations.

2.2.1 Experiment Setup

The experiment setup for damage prognosis of riveted lap joint coupons consists of three major modules: sensing and data acquisition system, optical fatigue crack measurement system, and fatigue cyclic loading system (Fig. 2.1). Sensing and data acquisition system generates a 3.5 cycle tone burst lamb wave from Piezoelectric (PZT) actuators and records the corresponding signal received by PZT sensors. Optical crack measurement system uses a traveling microscope to measure the crack length after a certain number of loading cycles at regular intervals. The specimen is subjected to tensile cyclic loading using a hydraulic testing machine. The coupons were subjected to two types of loading spectrums: constant block loading and variable block loading as shown in Fig. 2.2.

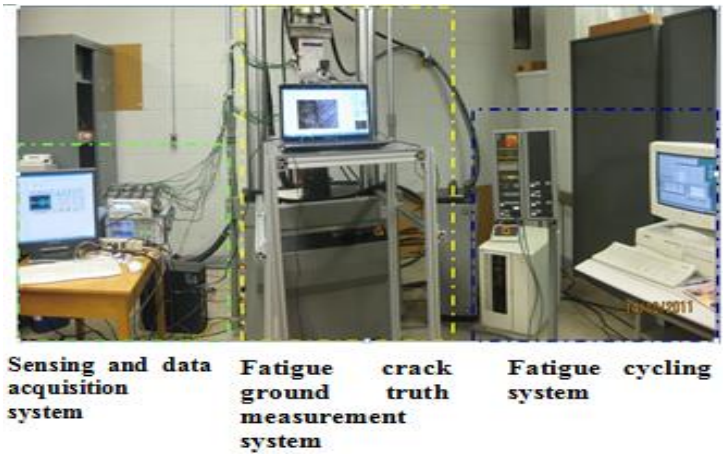

Fig. 2.1 Systematic Representation for the Lap Joint Damage Diagnosis System

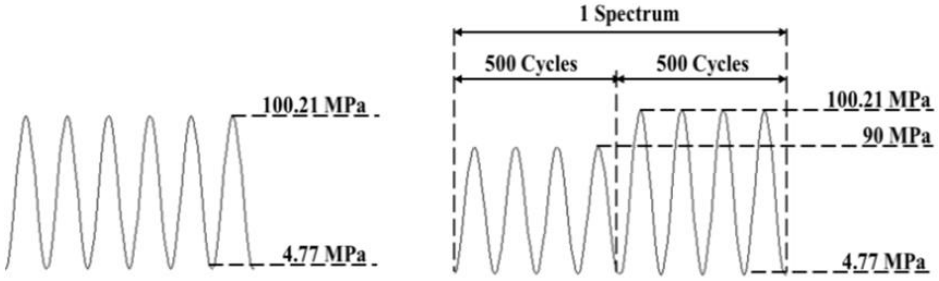

a) b)

Fig. 2.2 Loading Spectrum. a) Constant Loading; b) Variable Loading

2.2.2 Specimen Geometry and Sensor Layout Design

The riveted panels are made of 1.6 mm Al 2024-T3 sheets that were originally provided by NRC, Canada. For repeatability, additional coupons were manufactured at NASA. Three rows of rivets are embedded in the panels. The detailed geometry is shown in Fig. 2.3 and corresponding mechanical properties of the material are listed in Table 2.1. Multiple specimens are tested to show the reproducibility of the proposed method and to include the effect of uncertainties among different specimens. Detailed information for the specimens is given in Table 2.2.

Experimental results have shown that the major crack always appears at the countersunk hole in the first row. Therefore, the first row was considered as the target region for damage detection. Actuators and sensors are placed on the opposite sides of the first row. This ensures the crack would be on the direct wave path of the sensor-actuator pairs whenever it appears. To employ a pitch-catch method [7] , PZTs acting as actuators and sensors are glued on the two sides of the rivet holes. The corresponding sensor network configuration is shown in Fig. 2.4. Red dots represent actuators away from the target region and the green dots represent sensors near the target region. Each pair of sensors can interrogate the damage information on their direct wave path.

Table 2.1 Mechanical Properties of Al2024-T3

Material	Yield strength (Mpa)	Elastic modulus (Mpa)	σ_u (Mpa)	ΔK_{th} ($\mathrm{Mpam}^{0.5}$)
Al2024-T3	360	72000	490	1.1164

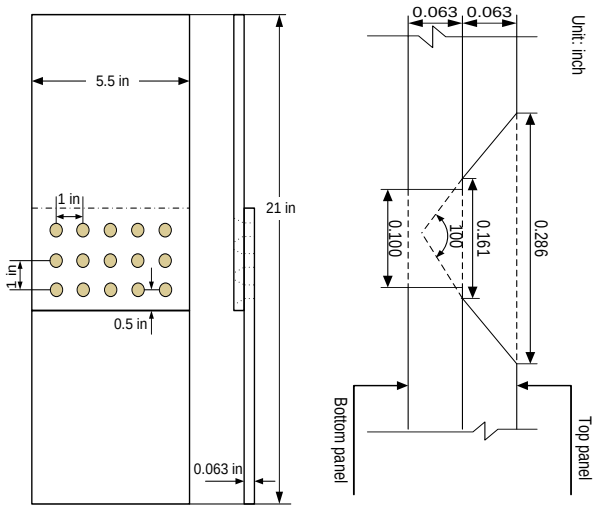

Fig. 2.3 Geometry of the Lap Joint and Detailed Dimension of the Connection Part

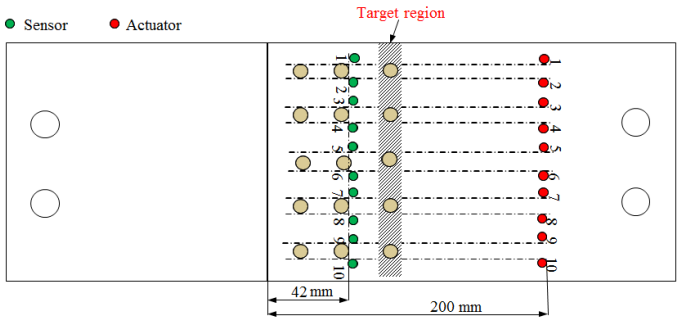

Fig. 2.4 Sensor Network Layout for Damage Detection on Riveted Lap Joint

Table 2.2 Testing Information for Different Specimens

Specimen #	Loading spectrum	Crack initiation wave path
T1	Constant loading	4 ↔ 4
T2	Constant loading	8 ↔ 8
T3	Constant loading	6 ↔ 6
T4	Constant loading	9 ↔ 9
T5	Constant loading	4 ↔ 4
T6	Constant loading	8 ↔ 8
T7	Variable loading	2 ↔ 2

2.3 Fatigue Crack Size Diagnosis

In the above discussion, a Lamb-based damage detection experiment is setup and used

to detect the crack evolution of lap joints between any two rivet holes. In this section, the collected PZT sensor signal is processed and a deterministic damage detection method is proposed based on the extracted damage identification features. Several regression models are compared to investigate the detection model uncertainty, which will be incorporated in the physic fatigue propagation law for predicting remaining life.

2.3.1 Experimental Results and Data Processing

In this study, a Hamming-windowed sinusoidal tone burst with 3.5 cycles was used as the actuating signal. The central frequency of this signal was set at 200kHz, as shown in Fig. 2.5. After installing the specimen on the hydraulic machine, the baseline signal for normal condition is collected first. Further data are collected periodically and the traveling microscope is used to measure the surface crack length at regular intervals. Fig. 2.6 illustrates a typical signal obtained for specimen T4 subjected to the constant amplitude loading. With further signal processing, changes in selected features (phase change, correlation coefficient, and amplitude change) are calculated. The amplitude change reflects the energy dissipation due to the crack. The phase angle change is due to the traveling distance change due to the crack. The correlation coefficient change reflects the signal perturbation due to the new waves generated at the crack surfaces [31]. All of these feature changes can be obtained by comparing the received signal under normal and defect conditions. Detailed description is available from the open literature [32-34]. The relationship between trends in features and crack length is shown in Fig. 2.7.

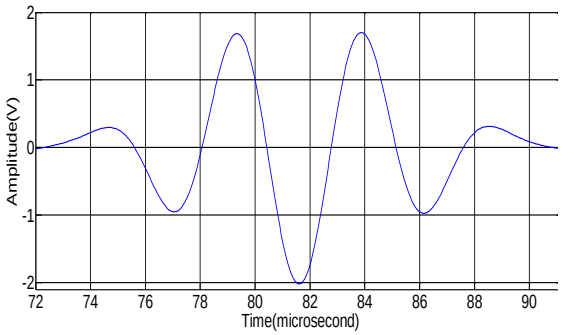

Fig. 2.5 A Tone Burst Signal of 3.5 Cycles with 200 kHz Central Frequency

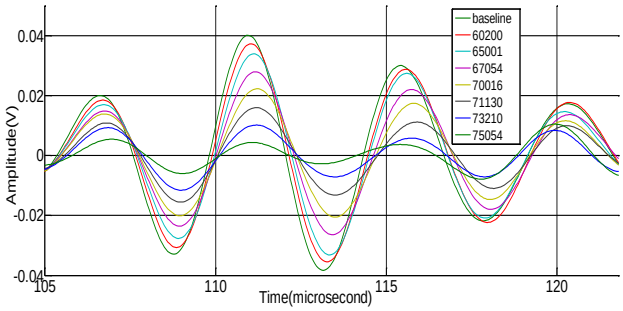

Fig. 2.6 Received Signal for Specimen T4 Shows Amplitude Changes with Increasing Number of Fatigue Cycles, i.e. Increased Crack Lengths

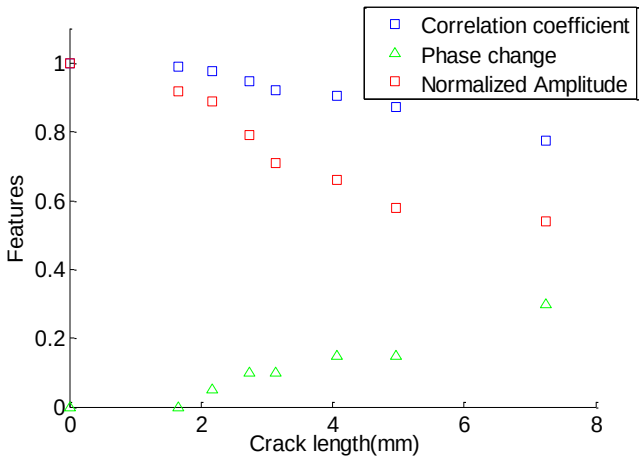

Fig. 2.7 The Relationship between Signal Features and Crack Length

2.3.2 Fatigue Crack Detection Using Extracted Features

2.3.2.1 Linear Regression Model

As shown in Fig. 2.7, all features exhibit monotonic relationships with increasing crack

length. Thus, all three features are potentially good candidates for crack detection and crack length estimation. A linear regression model is used to combine all three features and to predict the crack lengths. Using datasets from several test specimens, a linear regression as shown in Eq.(2-1), is trained using datasets from five different specimens (T1, T2, T3, T4, and T5). Table 2.3 lists the regression coefficients for this formulation.

$$a = \beta + \beta_1 x + \beta_2 y + \beta_3 z \tag{2-1}$$

where a is the detected crack length. x is the correlation coefficient, y is the phase change variable, and z is the normalized amplitude.

Table 2.3 Coefficients for the Linear Regression Model

Coefficients	**Value**
β	4.23
β_1	1.98
β_2	4.23
β_3	-4.79

Using the diagnostic model trained above, crack lengths for other specimens can be obtained. Fig. 2.8 shows experimentally measured crack lengths and the detection results for the two specimens (NRC T6 and variable loading T7). It can be observed that detection results show general agreement with experimentally measured crack length in general.

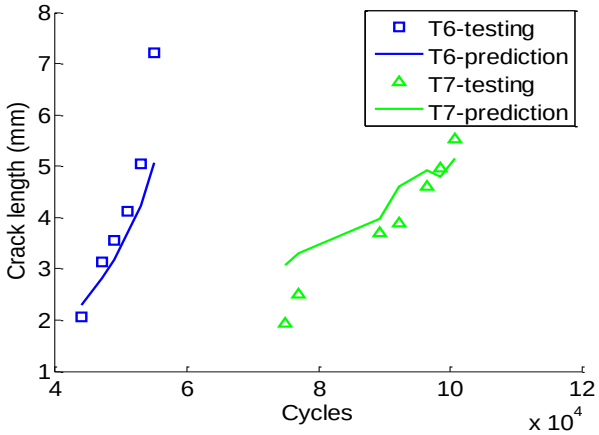

Fig. 2.8 Measurement and Detection Model Prediction Using the Linear Regression Model

2.3.2.2 Quadratic Regression Model

Following the same procedure as the above discussed linear regression model, the quadratic detection model is given as Eq.(2-2) . This model is trained by datasets from five different specimens (T1, T2, T3 T4, and T5). The corresponding coefficients for this model are listed in Table 2.4.

$$a = A + \alpha_1 x + \alpha_2 y + \alpha_3 z + \alpha_4 xy + \alpha_5 xz + \alpha_6 yz + \alpha_7 x^2 + \alpha_8 y^2 + \alpha_9 z^2 \quad (2\text{-}2)$$

Table 2.4 Coefficients for Second Order Multivariate Regression

Coefficients	**Value**
A	7.92
α_1	-2.77
α_2	-2.69
α_3	-9.41
α_4	0.529
α_5	-5.19
α_6	10.0
α_7	6.21
α_8	0.67
α_9	3.50

Using the quadratic regression model described above, crack length estimates for validation specimen can be obtained. The measurement and model prediction of specimen T6 and T7 are shown in Fig. 2.9.

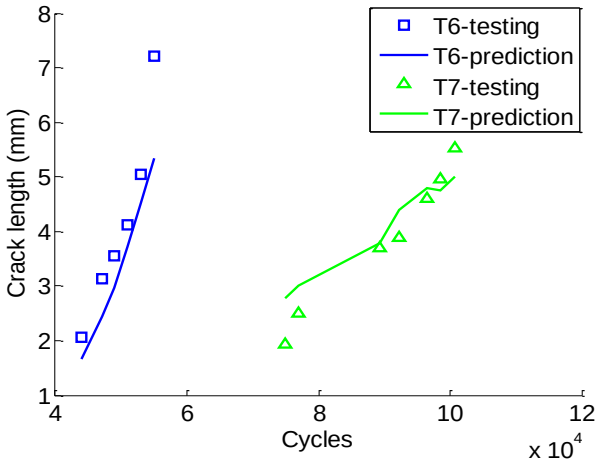

Fig. 2.9 Measurement and Detection Model Prediction Using the Quadratic Regression Model

2.3.2.3 Gaussian Regression Model

Gaussian process regression is a generalization of the Gaussian probability distribution [35]. Random variables, such as scalars or vectors (for multivariate distributions) are considered using a probability distribution. Given a dataset $D = \{X_1, X_2, \dots X_k | X_i \in R^D\}$ and $y = \{y_1, y_2, \dots y_k\}$, the system measurement y can always be related to an underlying function $f(X)$ using a Gaussian noise model,

$$y = f(X) + N(0, k(X, X')) \tag{2-3}$$

where $k(X, X') = E[\big(f(X) - m(X)\big)\big(f(X') - m(X')\big)]$ and $m(X) = E(f(X))$. A quick introduction of Gaussian processes in given in [36].

With an appropriate choice of mean function, covariance function, the function y = g(x) can be defined as $g(x) \sim GP(m(x), k(x, x')$. In comparison with several mean and covariance functions, the mean function and covariance function are chosen as

$$m(X) = ([\gamma_1 \quad \gamma_2 \quad \cdots \quad \gamma_D]X + \gamma_0)^2 \tag{2-4}$$

$$k(X, X') = \sigma_f^2 f_d(r_d) exp(-r_d) \tag{2-5}$$

$$r_d = \sqrt{\frac{d}{l^2}(X - X')^T(X - X')}$$

where $\gamma_0 \cdots \gamma_D$, σ_f, l are parameters need to be tuned to maximize the likelihood function. The detailed discussion of its application can be found in [35]. Since the signal feature space is three dimensional (Correlations coefficient, Phase change, and Amplitude), function $f_d(t)$ is chosen as $f_3(t) = 1 + t$. Following the previous procedure, this model is trained using datasets for (T1, T2, T3, T4, and T5), the datasets for T6 and T7 are used as validation. The results are shown in Fig. 2.10.

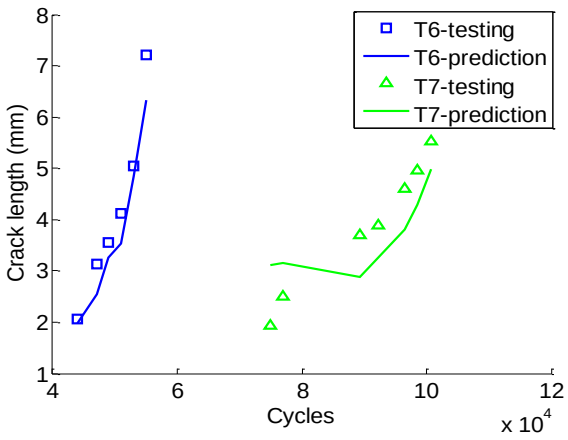

Fig. 2.10 Measurement and Detection Model Prediction for Specimens Using the GP Regression Model

Based on the above discussion of detection models, the relevant measures of goodness of fit statistics can be obtained, which are given as

Table 2.5 Comparison of Regression Statistic for Different Regression Models

	R square	Standard error
Linear regression model	0.909010	0.681268
Quadratic regression	0.961062	0.508134
Gaussian Regression model	NA	0.611133

R square measures the wellness of the fitting model and standard error is obtained by averaging the model prediction error from T6 and T7. By comparing above regression statistics, the Quadratic regression model gives the smallest standard error and the largest R square value. By fusion of three features, the large uncertainties caused by manufacturing, loading, and boundary effect can be significantly reduced.

2.4 Remaining Useful Life (RUL) Prognosis of Lap Joints

2.4.1 Bayes' Theorem and Uncertainties Management

Prognosis of the remaining useful life should be continuously updated using the latest measurement information available from the system. New information should be incorporated to improve the knowledge about the system, including distributions of its model parameters, modeling accuracy, and future loading conditions, all of which directly affect prognostic performance. The Bayes' theorem allows updating the distribution of parameters of interest based on condition monitoring system responses. The posterior distribution of the parameters can be obtained by combining its prior information and the current system response. Assume θ is the vector of parameters of interest, which are considered random variables and are updated using the evidence from monitored data d. The posterior distribution of the parameters can be expressed as

$$q(\theta|d) \propto p(\theta)p(d|\theta) \tag{2-6}$$

where $\mathrm{p}(\theta)$ is the prior distribution of the parameter, which may come from expert opinion, analysis of existing data [37], etc. $p(d|\theta)$ is the likelihood function and $q(\theta|d)$ is the posterior distribution of the parameter. In Bayesian updating, model and measurement uncertainties are incorporated in the construction of the likelihood function. Details are given below.

In the prognosis problem, the sources of uncertainties usually include, but not limited to, the mechanism modeling uncertainty (e.g., Paris law, crack closure model, and other mechanical models), the model parameter uncertainty (e.g., the power coefficients and the initial crack length in a model), and the measurement uncertainty (e.g., crack length measurements from different NDT techniques). Consider a generic mechanism model to describe the time-dependent behavior of a system,

$$x' = M(N, \theta) + \epsilon_1 \tag{2-7}$$

where x' is system response, ϵ_1 is model prediction error, and $M(N, \theta)$ is the physics model prediction, in which N is the index variable (i.e., non-random variable, such as time and spatial coordinates), and θ is a vector of model parameters.

In some engineering applications, the system response cannot be directly measured and needs to be inferred from indirect measurements. For example, the crack in a component cannot be easily measured directly using optical method due to the inaccessible locations of these cracks. Features from NDT sensor signals are generally used to infer the crack length. In this case, the inference (i.e., the feature integration model in the proposed study) itself introduces additional uncertainties. The proposed feature integration model include components like data reduction schemes, feature extraction, regression analysis to establish correlation between features and system responses, etc. For a certain feature integration model $D(F)$ using signal features F to infer the system response, the relationship between $D(F)$ and x' can be expressed as

$$D(F) = x' + \epsilon_2 \tag{2-8}$$

where a random variable ϵ_2 is used to describe measurement uncertainty introduced by the feature integration model. To update the target system using the detected system response, the likelihood function $p(D(F)|\theta)$ is constructed below.

The probability distribution of ϵ_1 is represented as $p(\epsilon_1|\theta) = f_1(\epsilon_1)$ and the probability of measurement error ϵ_2 is $p(\epsilon_2|\,\theta) = f_2(\epsilon_2)$. The conditional probability of $p(D(F)|\theta)$ can be obtained by marginalizing the joint probability $p(D(F), x', \epsilon_2|\theta)$ over x' and ϵ_2, which is given as

$$p(D(F)|\theta) = \iint_{x',\epsilon_2} p(D(F), x', \epsilon_2|\theta)dx'd\epsilon_2 \; =$$

$$\iint_{x',\epsilon_2} p(\,x'|\theta)\, p(\epsilon_2|\,\theta)p(D(F)|x', \epsilon_2, \theta)dx'd\epsilon_2 \qquad (2\text{-}9)$$

Given the above relationship, the constraint shown in Eq.(2-7) and (2-8) can be incorporated into Eq.(2-9) using Dirac delta function. The likelihood function $p(D(F)|\theta)$ can be expressed as

$$p(D(F)|\theta) = \int_{x'} f_1(x' - M(N, \theta))\, f_2(D(F) - x')dx' \qquad (2\text{-}10)$$

It can be seen that the condition probability $p(D(F)|\theta)$ is the convolution between probability distribution $f_1(\epsilon_1)$ and $f_2(\epsilon_2)$. It should be noted that Eq. (2-10) is the general solution and is capable of correlated non-Gaussian random variables. The general solution for Eq.(2-10) is not apparent and numerical simulations can be used to approximate the distribution. In the proposed study, the two uncertainty terms $f_1(\epsilon_1)$ and $f_2(\epsilon_2)$ are assumed to be independent Gaussian distributions [38, 39] to demonstrate the overall methodology. In that case, the convolution of the two Gaussian probability distribution can be expressed as

$$p(D(F)|\theta) = \frac{1}{\sqrt{2\pi(\sigma_{\epsilon_1}^2+\sigma_{\epsilon_2}^2)}} exp(-\frac{1}{2}\frac{(D(F)-M(N,\theta))^2}{\sigma_{\epsilon_1}^2+\sigma_{\epsilon_2}^2}) \quad (2\text{-}11)$$

where σ_{ϵ_1} and σ_{ϵ_2} are standard deviation of these two variables. Substituting Eq.(2-11) into Eq.(2-6) and omitting the constant term, the posterior distribution of model parameters can be expressed as

$$q\big(\theta\big|D(F)\big) \propto p(\theta) \cdot exp(-\frac{1}{2}\frac{(D(F)-M(N,\theta))^2}{\sigma_{\epsilon_1}^2+\sigma_{\epsilon_2}^2}) \quad (2\text{-}12)$$

In Eq. (2-12), it is shown that the modeling error and measurement noise are "lumped" to a single uncertainty term using the independent Gaussian assumptions. Future experimental and theoretical work is required to separately investigate their effect on the prognosis results. In the Bayesian updating, direct estimate of the posterior distribution with complex mechanism models is different and numerical method, such as the Markov-Chain Monte-Carlo (MCMC) method, is used to draw samples for the posterior distribution estimation. The MCMC method is well documented in open literatures [20, 40-42] and details are not given in this paper. Interested readers can find more details in the cited references.

2.4.2 Fatigue Crack Growth Model

To use the mechanism-based approach, a fatigue crack growth model is introduced here to calculate the crack length for given loading cycles, which utilizes the transformation between random loading and its equivalent constant loading. The used equivalent stress model is very efficient for the random variable loadings without the cycle-by-cycle calculation and has been validated with different sets of experimental data [43]. A brief discussion for the model is given below. In the equivalent stress level fatigue crack growth model, a generalized crack growth rate curve is assumed as

$$\frac{da}{dN} = f(\Delta\sigma, R, a) \tag{2-13}$$

where $\frac{da}{dN}$ is the crack growth rate, $\Delta\sigma$ is the applied stress amplitude, R is the stress ratio, and a is the crack length. The total fatigue life N_{total} under arbitrary random loading history can be written as

$$N_{total} = \sum_0^n N_i = \sum_0^n \int_{a_i}^{a_{i+1}} \frac{da}{f(\Delta\sigma_i, R_i, a)} da \tag{2-14}$$

where a_0 is the initial crack size and N_i is the loading cycles when crack size increases from a_i to a_{i+1}. For random variable loading, the proposed model tries to find an equivalent constant amplitude loading crack growth process under which the fatigue life obtained would be same with that of the true random loading case. The fatigue life of this equivalent crack growth process can then be expressed as

$$N_{total} = \int_{a_0}^{a_{n+1}} \frac{da}{f(\Delta\sigma_{eq}, R_{eq}, a)} da \tag{2-15}$$

Theoretically, the proposed model can be applied to any type of crack growth model and variable loading case. Here a modified Paris model under two constant loading spectrum within one block is derived.

First, to incorporate the stress ratio effect, the Paris' law is modified as

$$\frac{da}{dN} = C(\Delta K)^m = g(R)(\Delta K)^m \tag{2-16}$$

where *C* and m are the fitting parameters in the Paris' law. Parameter *C* can be expressed as $g(R) = kb^R$, where k and b are fitted by experimental data under different stress ratios *R*. Based on Eq.(2-14) and (2-15) , the equivalent stress level $\Delta\sigma_{eq}$ in above equation can be described as

$$\Delta\sigma_{eq} = \left(\frac{N_1}{N_1+N_2}\frac{g(R_1)(\Delta\sigma_1)^m}{g(0)} + \frac{N_2}{N_1+N_2}\frac{g(R_2)(\Delta\sigma_2)^m}{g(0)}\right)^{\frac{1}{m}} \quad (2\text{-}17)$$

where N_1 and N_2 are the two constant loading cycles in one block. For the equivalent loading condition, the parameters k and m should be calibrated for specific specimens and are treated as random variables to express uncertainty.

To correctly predict the fatigue life, an initial crack length estimate is needed as input to the crack growth model. An equivalent initial flaw size (*EIFS*) concept [44] is applied to calculate the crack length for a given number of load cycles. In the probabilistic crack growth analysis, the *EIFS*, the parameter *k*, and *m* are three random variables that need to be updated. The initial estimation of EIFS can be calculated as

$$a = \frac{1}{\pi}\left(\frac{\Delta K_{th}}{\Delta\sigma_f Y}\right)^2 \quad (2\text{-}18)$$

where Y is a geometry correction factor depending on specimen geometry and crack configuration, $\Delta\sigma_f$ is fatigue limit, and ΔK_{th} is the threshold stress intensity factor. For lap joints, the corresponding detailed solution for Y is given in [45].

To clarify the whole process, a schematic of the probabilistic fatigue damage prognosis framework is shown in Fig. 2.11 and a step-by-step summary with reference to each equation is given below,

- Determine the prior distribution of parameters (i.e. EIFS, k, and m) $p(\theta)$
- Train the feature integration model $M(N, \theta)$, such as Eq.(2-1), (2-2) or (2-3) to build the likelihood function Eq. (2-12), which should also incorporate the fatigue crack growth model expressed in Eq.(2-13)-(2-17). Estimate the posterior distribution (i.e. Eq.(2-12)) of parameters using MCMC simulation

- Remaining useful life (RUL) is recalculated by plugging the posterior distribution of parameters into the fatigue crack growth model (Eq.(2-13)-(2-17))

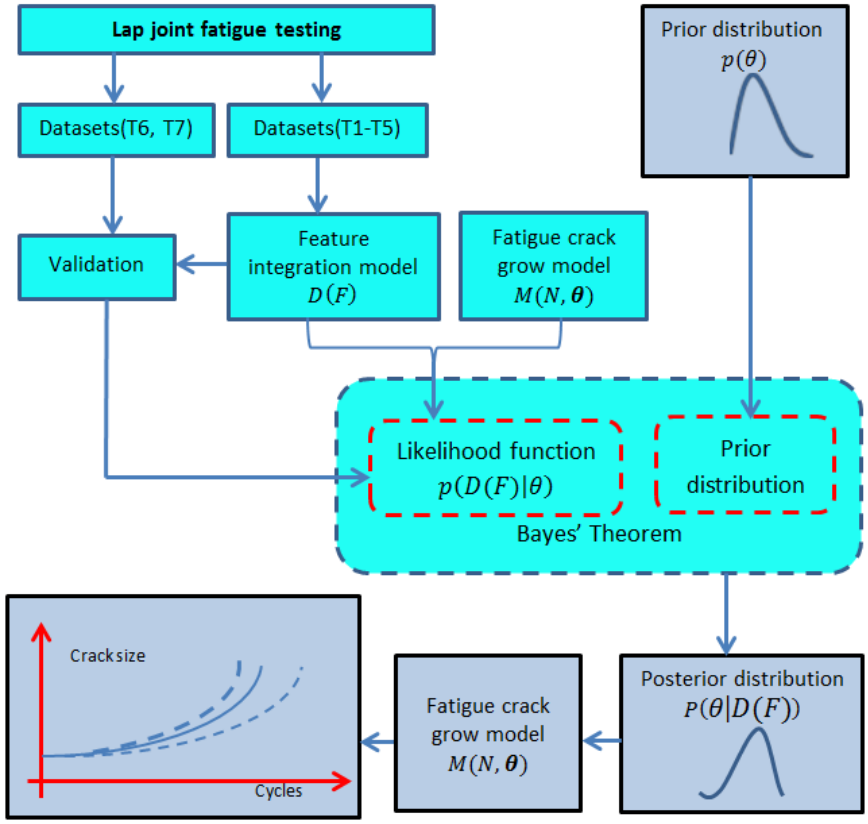

Fig. 2.11 Overall Prognosis Framework Based on Bayesian Updating

2.4.3 Lap Joint Fatigue Life Prediction Using Bayesian Inference

2.4.3.1 Constant Loading Case

Based on the prognostic method discussed before, the detected crack length from the above Quadratic model is used to update the model parameters, and then predict the remaining useful fatigue life (RUL). Since the experimentally measured crack length is used as validation, the measurement error of the crack length is omitted in the demonstration examples. Fig. 2.12 shows the prior belief and Fig. 2.13 shows the updated results from the proposed prognosis method. Blue solid line is the median prediction using

the prior distribution. Hollow rectangular points are the optically measured crack length and are considered as the true crack length. Black solid points are the crack estimation from the Lamb wave-based damage detection method.

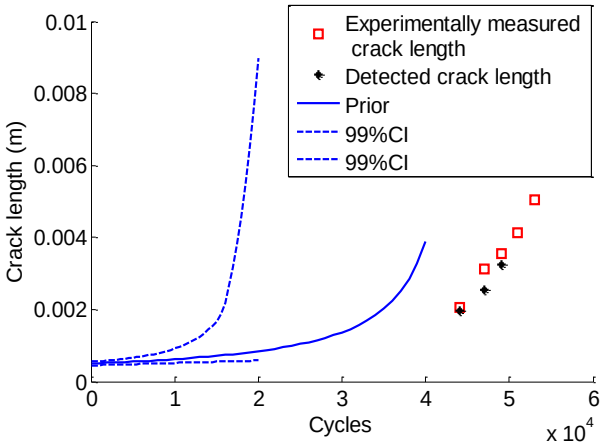

Fig. 2.12 Prior Belief and Dataset for T6

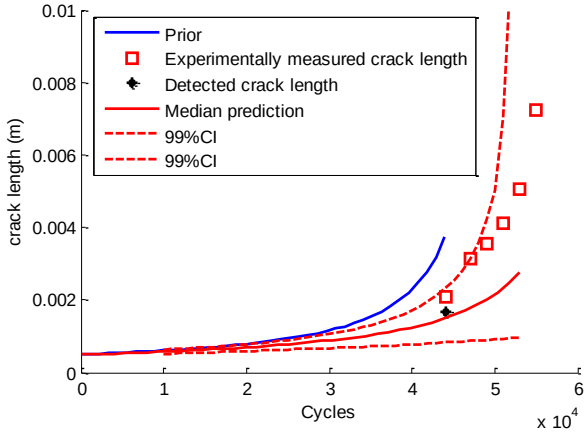

a.

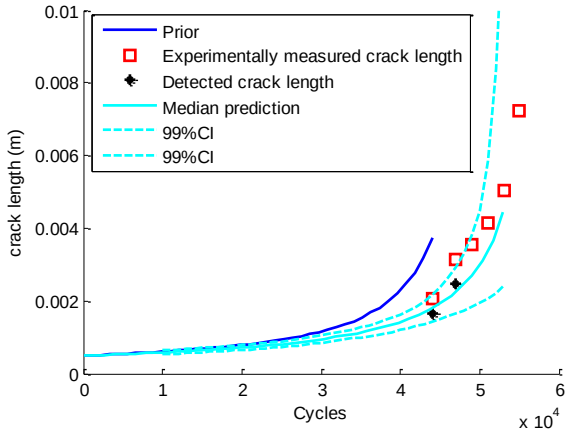

b.

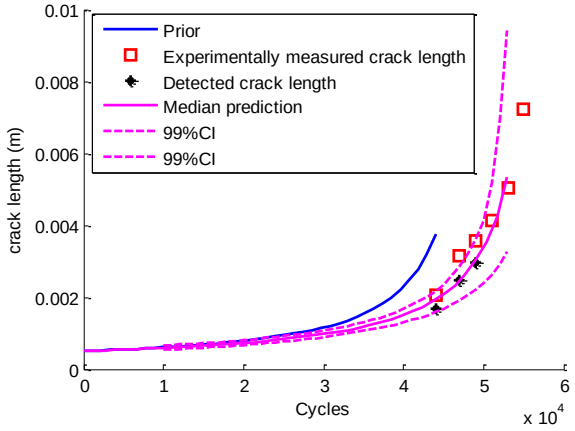

c.

Fig. 2.13 Bayesian Updating Results.
a) Updating One, b) Updating Two, c) Updating Three.

From Fig. 2.13, it can also be seen that the median prediction trend gets closer to the testing dataset with additional updating using detection data. The uncertainty bounds become narrower with additional updating, which indicates the effectiveness of the Bayesian updating method in reducing prognostic uncertainties. This trend can also be observed in the updated parameter distribution, shown in Fig. 2.14.

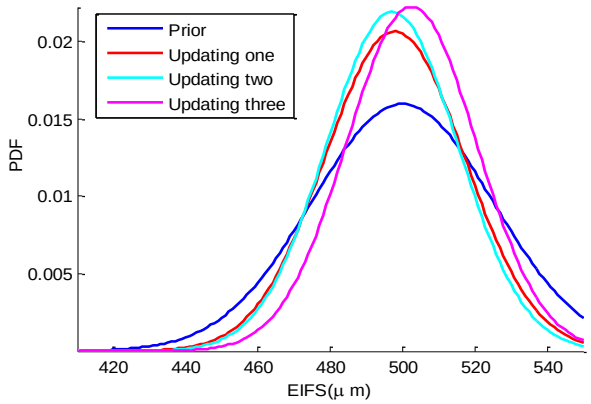
Prior
Updating one
Updating two
Updating three
PDF
0.02
0.015
0.01
0.005
420
440
460
480
500
520
540
EIFS(μ m)

a.

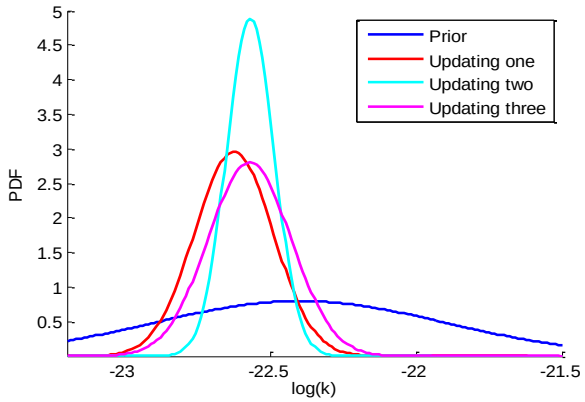
Prior
Updating one
Updating two
Updating three
PDF
5
4.5
4
3.5
3
2.5
2
1.5
1
0.5
-23
-22.5
-22
-21.5
log(k)

b.

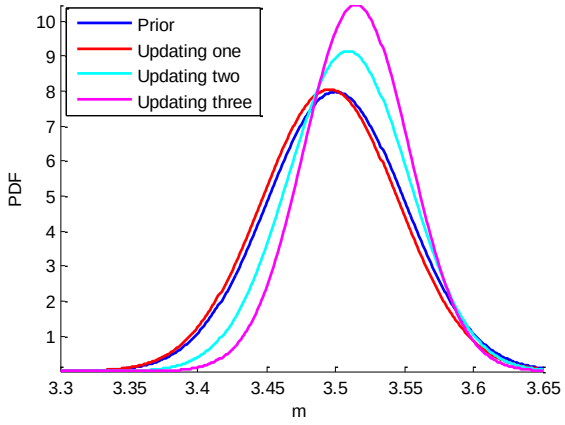
Prior
Updating one
Updating two
Updating three
PDF
10
9
8
7
6
5
4
3
2
1
3.3
3.35
3.4
3.45
3.5
3.55
3.6
3.65
m

c.

Fig. 2.14 Parameter Updating Results.
a) Updated EIFS, b) Updated log(k), c) Updated m.

2.4.3.2 Variable Loading Case

Following the same procedure as described in Section 2.4.3.1, the prognosis is carried out for the variable amplitude loading case. The detected crack length from the Quadratic regression model is used as the updating dataset. Fig. 2.15 shows the prior belief and two sets of data (i.e., crack length measurements from optical microscope and those from Lamb wave detection). Fig. 2.16 shows the updated results using the proposed prognosis method.

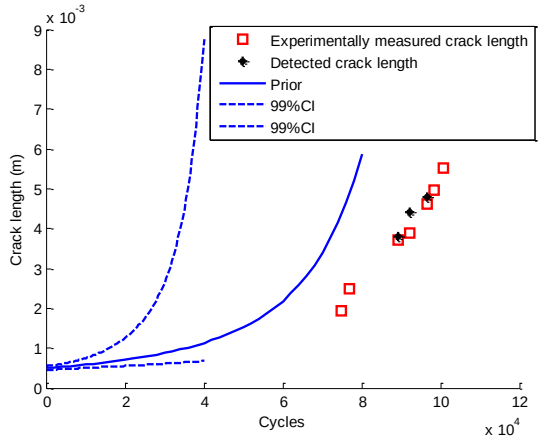

Fig. 2.15 Prior Belief and Dataset for T7

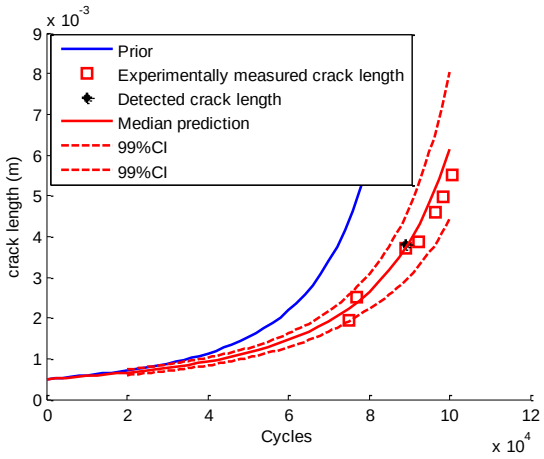

a.

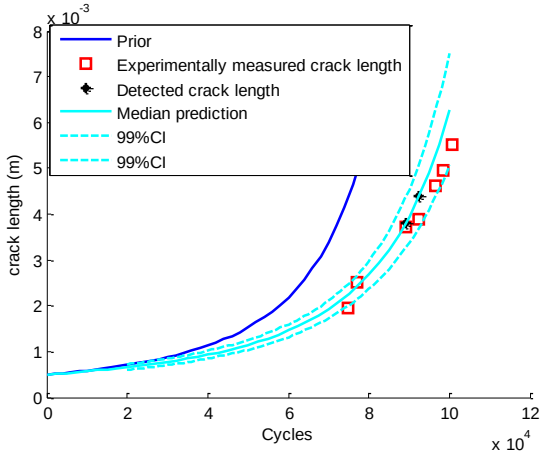

b.

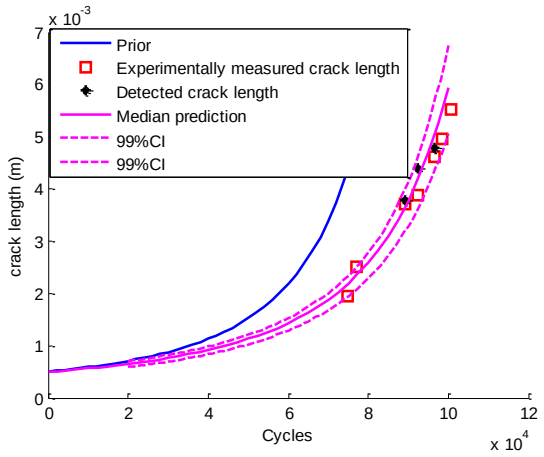

c.

Fig. 2.16 Bayesian Updating Results.
a) Updating One, b) Updating Two, c) Updating Three.

From the above figures, a similar trend can be observed for the updated crack growth trajectory as well as for the constant amplitude loading case. The 99% confidence bound is reduced when additional updating is performed. Fig. 2.17 shows the updated parameter distribution. The distribution of the updated parameters converges as more detected data is used in the Bayesian updating.

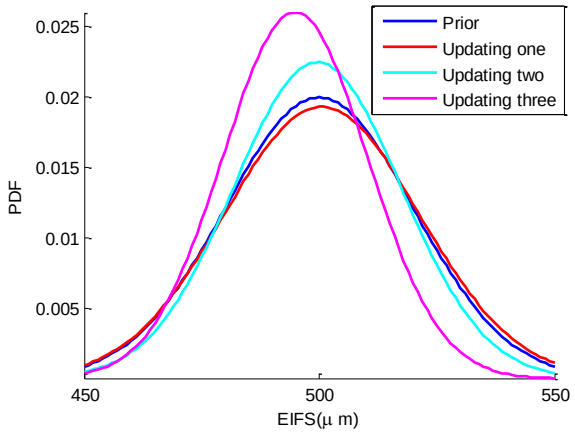
Prior
Updating one
Updating two
Updating three
PDF
0.025
0.02
0.015
0.01
0.005
450
500
550
EIFS(μ m)

a.

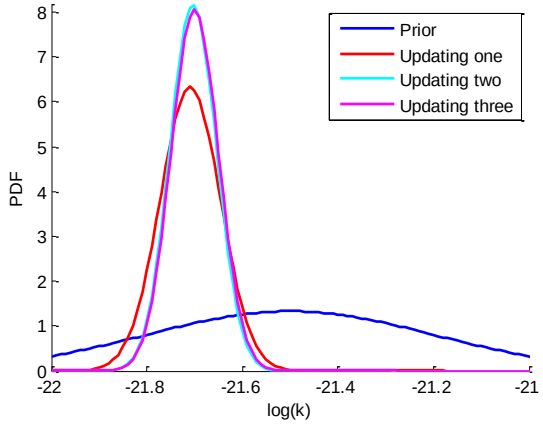
Prior
Updating one
Updating two
Updating three
PDF
8
7
6
5
4
3
2
1
0
-22
-21.8
-21.6
-21.4
-21.2
-21
log(k)

b.

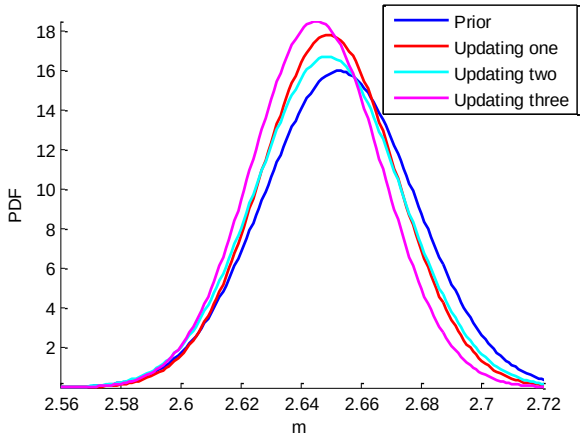
Prior
Updating one
Updating two
Updating three
PDF
18
16
14
12
10
8
6
4
2
2.56
2.58
2.6
2.62
2.64
2.66
2.68
2.7
2.72
m

c.

Fig. 2.17 Parameter Updating Results.
a) Updated EIFS, b) Updated log(k), c) Updated m.

2.4.4 Prognostic Performance Evaluation Using Prognostic Metrics

To evaluate the performance of the prognostic model, prognostic metrics are employed. A detailed discussion of metrics-based model validation can be found in [46-49]. Several relevant metrics, such as Prognostic Horizon (PH), $\alpha - \lambda$ Accuracy, Relative Accuracy (RA), Cumulative Relative Accuracy (CRA), and Convergence are discussed in that publication. In this paper, Prognostic Horizon is used to assess prognostic algorithms performance. The Prognostic Horizon describes the length of time before end–of–life (EoL) when a prognostic algorithm starts predicting with desired accuracy limits. The limit is expressed using an α-bound given by $\pm\alpha \cdot t_{EoF}$. In contrast, $\alpha - \lambda$ Accuracy determines whether prediction accuracy is within desired accuracy levels (specified by α) around RUL at any given time specified by λ. The smaller α means the higher desired accuracy. The performance is visually depicted on an RUL vs. Time plot, where accurate predictions would lie on the ground truth RUL line (black solid line) for all times. The red dots in the plots represent predicted performance at times when the Bayesian updating was applied. Error bars represent the spread of predicted PDF for corresponding prediction. The prognosis performance validation for the constant loading case and the variable loading case is shown below.

- Constant loading prediction performance assessment

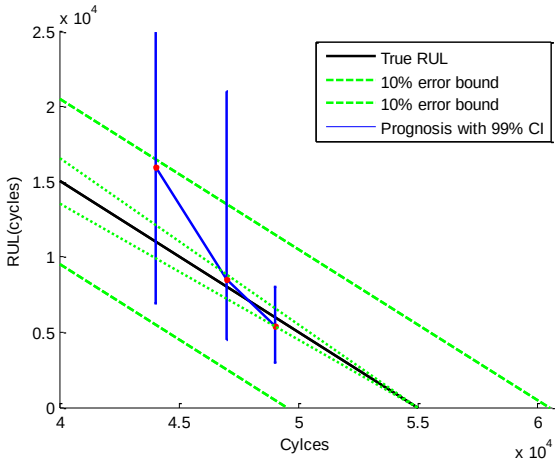

Fig. 2.18 Parameter Updating Results.
a) Updated EIFS, b) Updated log(k), c) Updated m.

Fig. 2.18 shows that the excellent median prediction is obtained after each updating. The 99% RUL prediction interval enters the 10% error bound at the third updating, so the proposed prognostic method can provide a satisfactory prediction of RUL.

- Variable loading prediction performance assessment

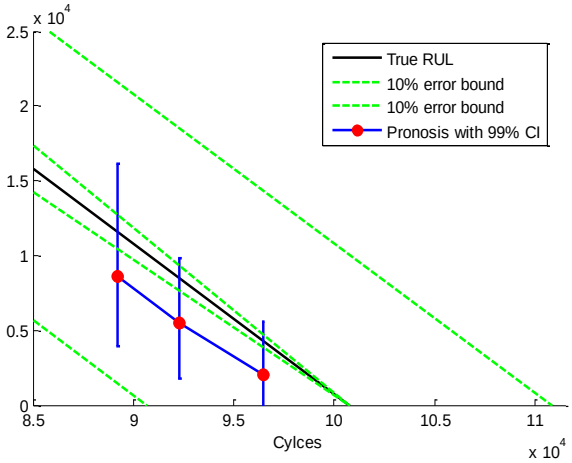

Fig. 2.19 Prognostic Performance Validation for Variable Loading

From Fig. 2.19, the same trend can be observed. The 99% RUL interval prediction enters the 10% error bound after each updating. In addition, the confidence bound is reduced to a certain level when sequential updating is applied. Given the latest system response, the

Bayesian updating can provide a more accurate RUL prediction considering all the uncertainties. Therefore, the updating result can provide an informative knowledge for health and risk management at the early stage of the whole lifecycle.

2.5 Numerical Simulation of Lamb Wave Propagation within Aluminum Plates

Many studies have been proposed to use the Lamb wave technique for defects detection in composite and metallic components. Numerical modeling of Lab waves were proposed to handle the local interaction between PZT sensor and host material [50]. Models of surface-bounded PZT disks are modeled based on effective force, moment and displacement [51]. The piezoelectric element is also coupled in FE model to simulate the Lamb wave propagation in composite structures [52]. In the proposed study, the direct coupled analysis of piezoelectric and mechanical finite element analysis is used to obtain the received signal at multiple sensor locations. This approach can include the possible coupling effect of electric potential variation and mechanical vibrations.

2.5.1 FE Modeling and Sensor Layout

The specimen in this simulation is made of Al 2024-T3 with dimension 150 × 150×1.6mm. In the center of the plate, a crack is introduced to represent the damage (Fig. 2.20).This plate is meshed using 8-node 3-D brick element and the left and right boundaries of the plate are fixed in all degree of freedoms. One actuator and six sensors are attached on the plate and perfect bonding is assumed between the sensors and the aluminum plate. The PZT disks are meshed using C3D8E elements. The electric potential for the top and bottom surface of the piezoelectric disk is coupled to the master nodes assigned to each surface. The actuating signal is applied at the master node of the actuator's top surface and reaction electrical charge can be monitored at the master nodes of the sensors' top surfaces.

In the simulation, the master nodes on the bottom surfaces are set to be zero electrical boundary condition. The detailed specimen dimension and sensors layout are shown in Fig. 2.20.

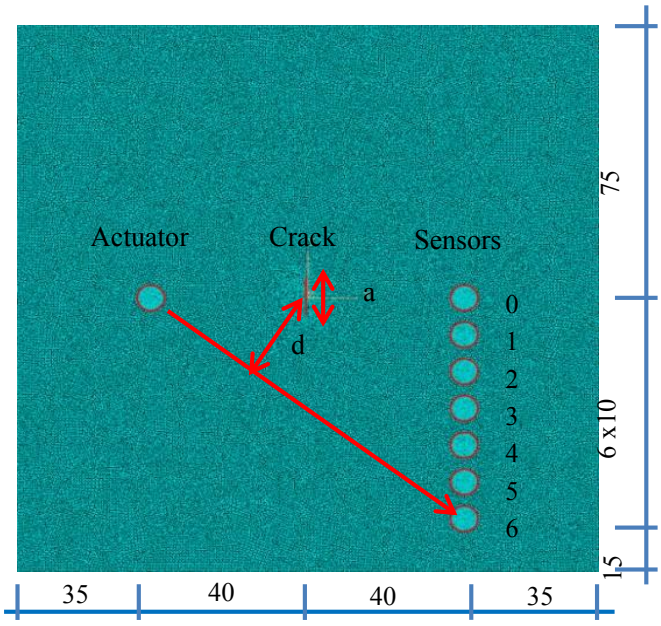

Fig. 2.20 Specimen Dimension and Sensors Layout (mm)

The mechanical and piezoelectric constants for PZT sensors are shown in Table 2.6 and Table 2.7.

Table 2.6 The Mechanical Constant of PZT Sensors

Elastic Consta	E_{11}	E_{22}	E_{33}	ν_{12}	ν_{13}	ν_{23}	G_{12}	G_{13}	G_{23}
	7	7	56	0.	0.	0.	18	23	23

Table 2.7 The Piezoelectric Constant of PZT Sensors

Dielectri c	E_{11}	E_{22}	E_{33}	Piezoelectr ic	d_{11}	d_{22}	d_{33}
	0	0	1.6		-	-	-

In the simulation, sensor signals are collected under the pristine and damaged conditions. For the damaged condition, multiple crack length is manipulated and the corresponding signal response is received for each sensor. Based on the above sensor

network layout, different crack length information is captured by a particular sensor pair and crack position information is captured by different sensor pairs. Using advanced signal processing techniques, the crack length and location are expected to be correlated with the signal features. Details are shown below.

2.5.2 Simulation Results and Data Processing

In this study, a Hamming-windowed sinusoidal tone burst with 3.5 cycles was used as the actuating signal. The central frequency of this signal was set to be 200kHz, as shown in Fig. 2.21. For any sensor pair, sensor signals under pristine and different crack length conditions are collected. Fig. 2.22 illustrates signal received by different sensors.

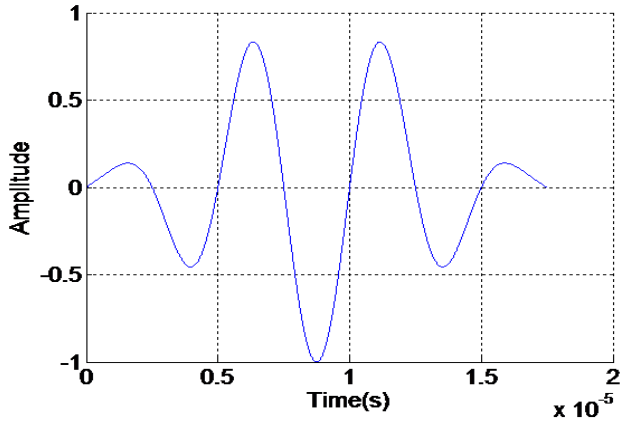

Fig. 2.21 A Tone Burst Signal of 3.5 Cycles with 200kHz Central Frequency

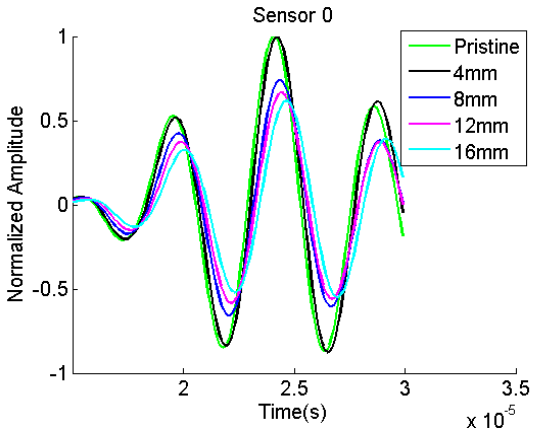

a) Signal received by sensor

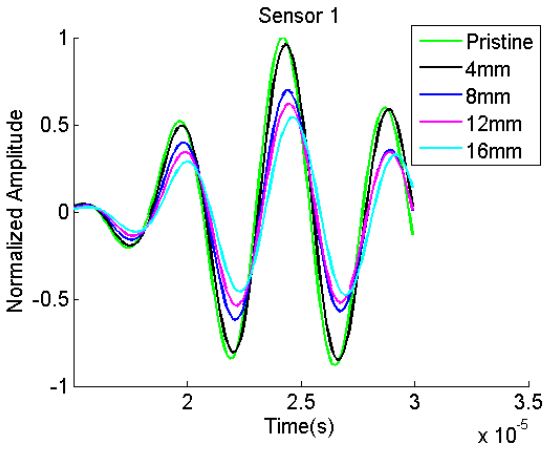

b) Signal received by sensor

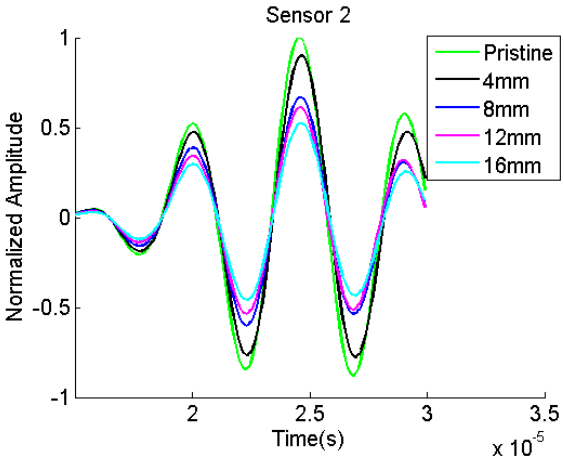

c) Signal received by Sensor 2

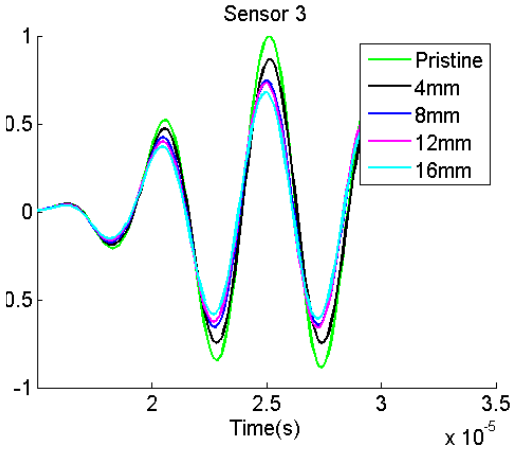

d) Signal received by Sensor 3

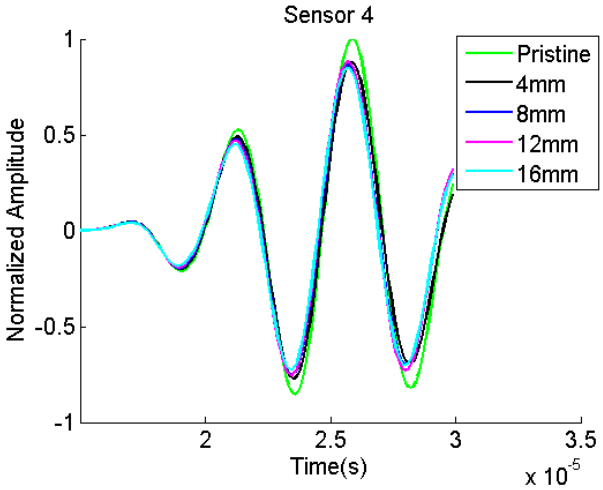

e) Signal received by Sensor 4

Fig. 2.22 Received Signal of Sensor 0 to Sensor 4 for Different Crack Length

As illustrated in above figures, the signal changes as the crack size changes. The signal change magnitude decreases as the sensor pair path is away from the crack location. With further signal processing, changes in selected features (correlation coefficient and normalized amplitude) are calculated. The amplitude change reflects the energy dissipation due to the crack. The correlation coefficient change reflects the signal perturbation due to the new waves generated at the crack surfaces [7]. All of these feature changes can be obtained by comparing the received signal under pristine and damaged conditions. Detailed description is given in literatures [32-34]. The signal features for different crack length, crack location are shown in Fig. 2.23.

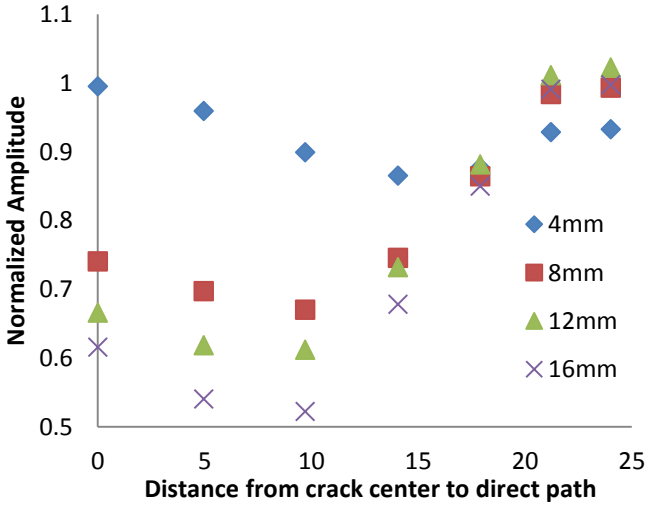

a) Normalized Amplitude

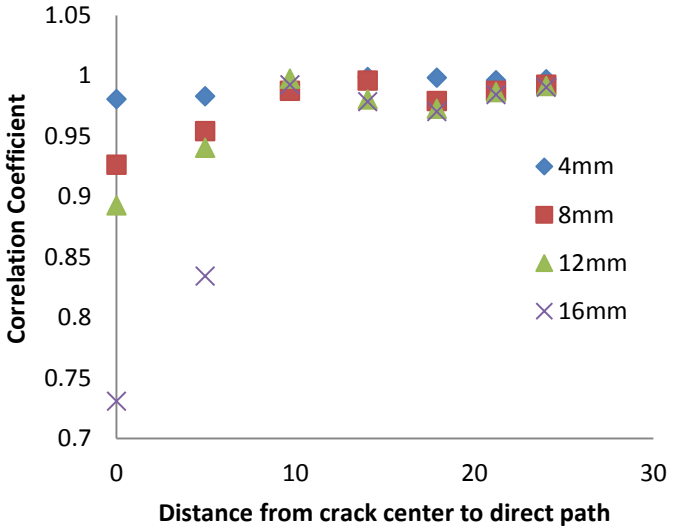

b) Correlation Coefficient

Fig. 2.23 Features for Different Crack Size and Locations

As shown in Fig. 2.23, the normalized amplitude feature is more sensitive to the damage even the crack is 20 mm away from the direct path. The correlation coefficient is not able to reliably detect the crack when the crack is 10 mm away from the sensor path. From this analysis, the normalized amplitude feature is used for the damage detection. In order to use the normalized amplitude in the Bayesian updating algorithm discussed later, a model is proposed to expressed the relationship between this feature and the crack size, position, which can be expressed as

$$feature = f(a, d) \tag{2-19}$$

where a is the crack length, d is the distance from crack center to the direct path. It should be noted that Eq.(2-19) is a generic expression and does not limit to a specific function type. In the proposed study, a polynomial regression model is used. From the trend of the curves in Fig. 2.23 and analysis of the dataset, the model for the normalized amplitude (NA) is given as

$$NA = (\alpha_1 + \alpha_2\, ln(a)) \times d^3 +$$
$$(\alpha_3 + \alpha_4\, ln(a)) \times d^2 +$$
$$(\alpha_5 + \alpha_6\, ln(a)) \times d +$$
$$(\alpha_7 + \alpha_8\, ln(a)) \qquad (2\text{-}20)$$

where $\alpha_1 - \alpha_8$ are regression coefficients, which can be obtained by the training datasets. After tuning these coefficients, the simulated and fitted features can be obtained. Fig. 2.24 shows the comparison between simulation and model fitting for the training dataset and validation dataset. It is shown that the employed simple regression model gives satisfactory results except for the region where the crack is very far away from the sensor pair path.

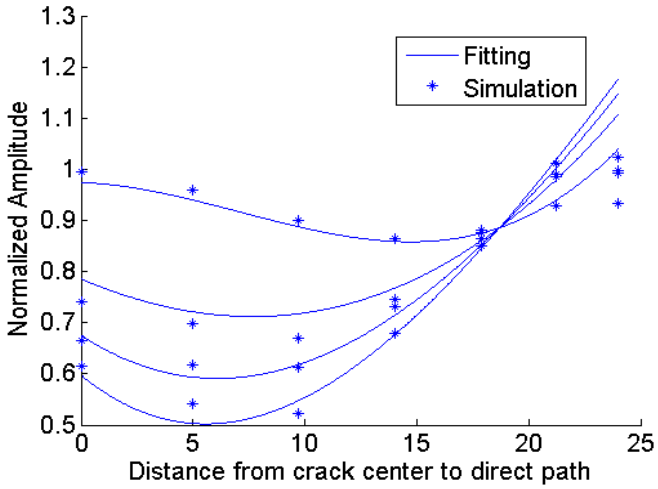

a) Training datasets (crack length: 4, 8, 12, 16 mm)

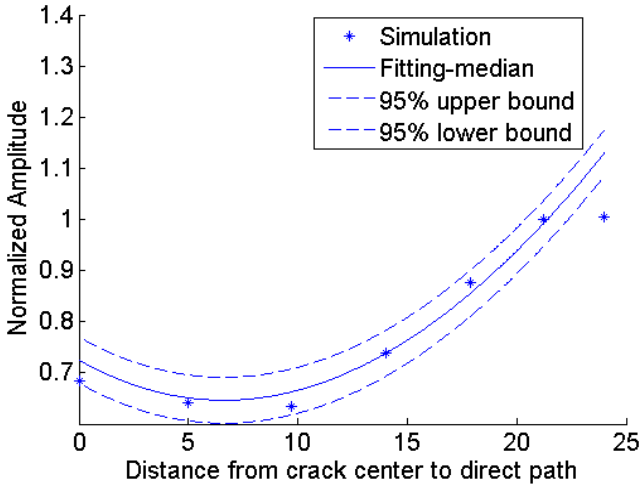

b) Validation dataset (crack length: 10 mm)

Fig. 2.24 Simulation and Fitting results for Normalized Amplitude

2.6 Damage Size and Location Diagnosis Using Bayesian Inference

Based on the discussion in section 2.4.1, Bayes' theorem can be used to manage the uncertainties embedded in the fatigue life prediction. The uncertainties in the damage diagnosis should also be considered. Unlike the deterministic damage diagnosis method mentioned in section 2.3, a probabilistic damage size and location detection method is proposed here using the finite element simulation results from section 2.5. The size and location are considered as two parameters in the Bayes' theorem, which will be updated when additional measurements (i.e. signal features) are available.

2.6.1 Damage Diagnosis Procedure

In the damage detection problem, the sensor signal can be collected during the daily service of structures and signal features can also be extracted using some signal processing techniques. To predict the damage size and location, a physics model $M(\theta)$ describing the relationship between signal features and damage information should be built, which can be substituted by the regression model shown in Eq. (2-20). By tuning this model using training datasets, the difference between this model prediction and true simulated system

measurements are determined, which can be used to build the likelihood of the Bayesian updating algorithm. Following this, the posterior belief about damage can be estimated by the posterior distribution of the updated parameters. Parameter θ represents the crack center coordinate (x_0,y_0) and crack size a. Since no prior belief is available for those three parameters, the prior distributions of them are assumed to be $x_0 \sim \mathrm{U}(-40,40)$, $y_0 \sim \mathrm{U}(-60,60)$, $a \sim \mathrm{U}(0.001,16)$. U indicates the uniform distribution (i.e., non-informative distribution). It should be noted that the crack distribution should be uniformly distributed from zero to a large length (e.g, the physical length of the specimen as the largest possible crack length). A very small quantity (i.e., 0.001 mm) for the crack distribution lower bound is used to avoid numerical difficulties. The overall diagnosis framework is shown in Fig. 2.25.

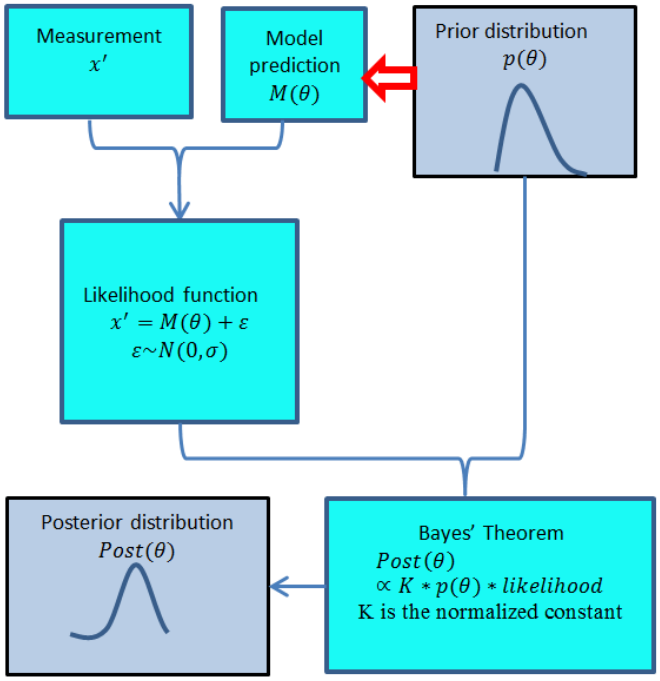

Fig. 2.25 The Overall Detection Framework Using Bayesian Updating

2.6.2 Demonstration Examples

2.6.2.1 Center Crack Location with Unknown Crack Size

To check the feasibility of this framework, a centered crack with different crack length is introduced in the aluminum plate. The sensor layout is shown in Fig. 2.26. Since the relative position of the crack and actuator is the same with that of the tuning datasets, only one actuator is used to actuate the signal. After the simulation, the corresponding received signal for each sensor is given in Table 2.8, which is used as the manipulated measurements to update the crack location and crack length. The data will be ignored if the normalized amplitude is greater than 1. The samples drawn by MCMC are plotted on the X-Y plane to show to evolution of the crack position after each updating and sample number remains the same through all the updating interactions. At the same time, the median and confidence bound prediction of crack length are extracted to show the accuracy of the crack size updating. The crack position and crack length updating are shown in Fig. 2.27 and Fig. 2.28.

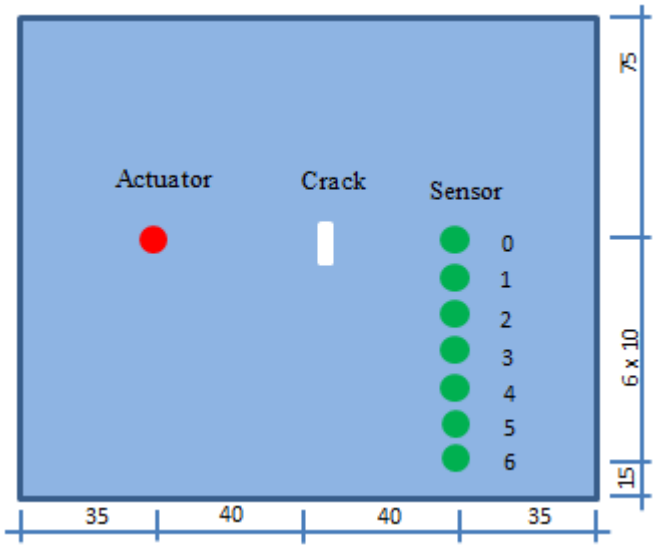

Fig. 2.26 Centered Crack Location with Unknown Size

Table 2.8 The Received Signal for Each Sensor Pair

Sensor pair	Normalized Amplitude
Actuator-Sensor0	0.6843
Actuator -Sensor1	0.6422
Actuator -Sensor2	0.6341
Actuator -Sensor3	0.7392
Actuator -Sensor4	0.8767
Actuator -Sensor5	1.001
Actuator -Sensor6	1.0038

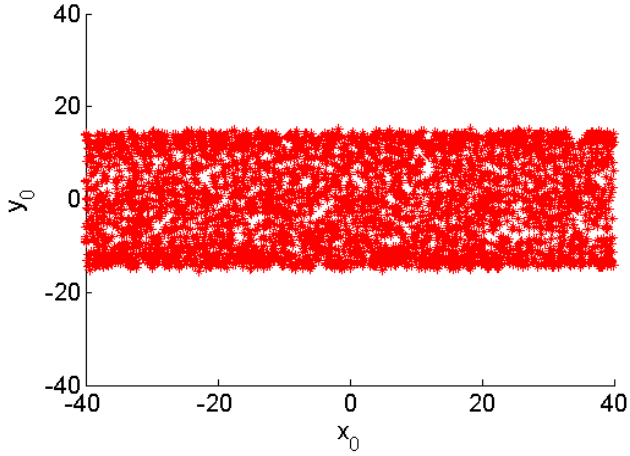

a) Updating one

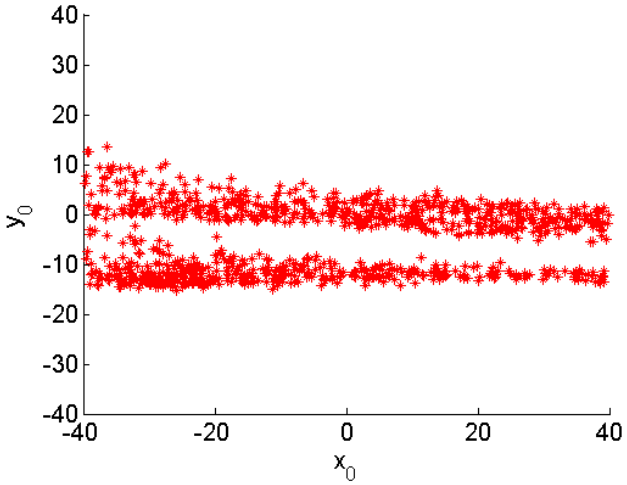

b) Updating two

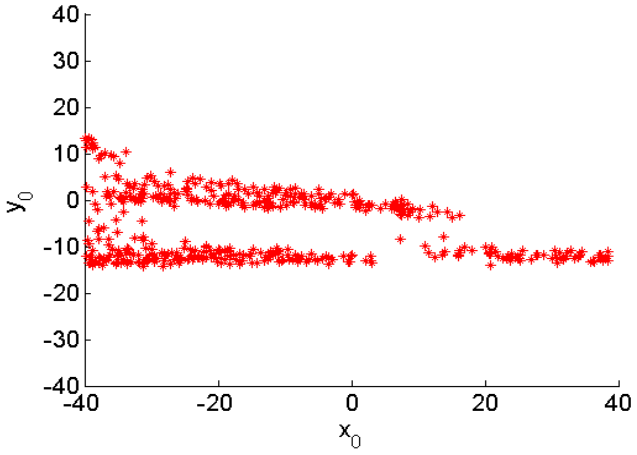

c) Updating three

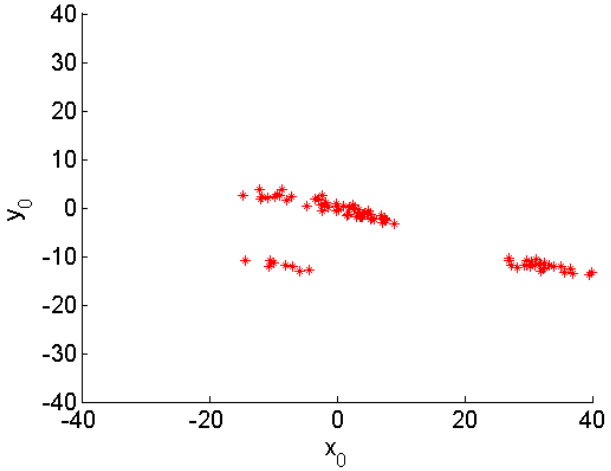

d) Updating four

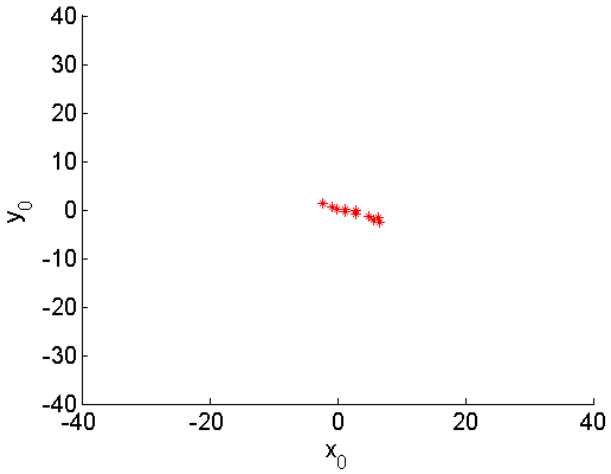

e) Updating five

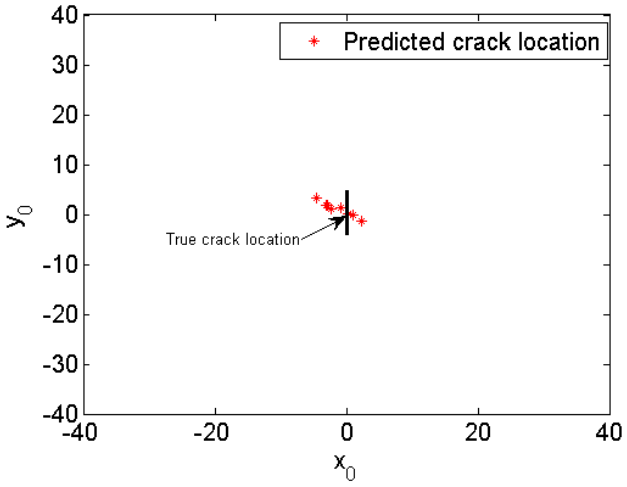

f) Updating six

Fig. 2.27 Crack Location Prediction

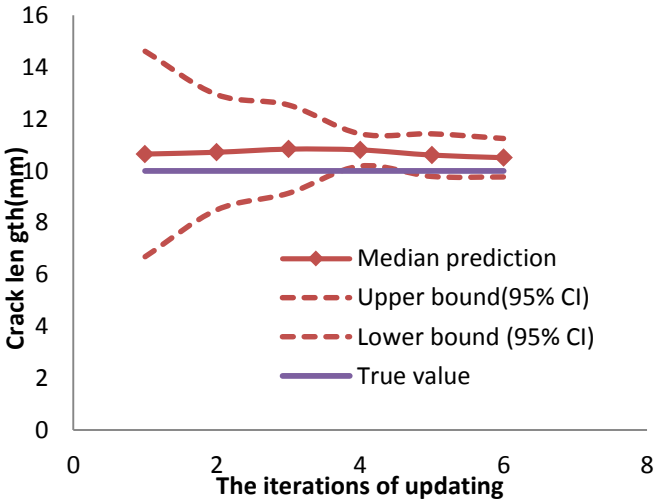

Fig. 2.28 Crack Length and its Confidence Bound Prediction

As shown in Fig. 2.28, the crack coordinate estimated is approaching closer and closer to the true crack location when applied more and more updating iterations. In Fig. 2.28, the confidence bound is narrowed as updating continues, but there is always a system error for the updated crack size, which is mainly due to the fitting error involved in the Eq. (2-20).

In that case, the performance of Bayesian updating can be improved by better physics model with reduced system error.

2.6.2.2 Random Crack Location with Unknown Crack Size

If the crack is located at a random location of the aluminum plate, multiple sensors should be used to provide enough updating information. To cover the entire plate, three actuators are attached on the left of the plate and thirteen sensors are put on the right of the plate. The sensor layout is shown in Fig. 2.29. During each run of simulation, only one of three actuators actuates signal and all the sensors act as the receivers. Similarly, the normalized amplitude feature is extracted from the received sensor signal. Following the above procedure, the median and confidence bound prediction of the crack location and crack size can be estimated from the posterior distribution of the parameters after each updating. The crack center coordinate (x_0, y_0) and crack length a median and confidence bound prediction are given in Fig. 2.30. To show the updating performance, the predicted and true crack location is shown in Fig. 2.31.

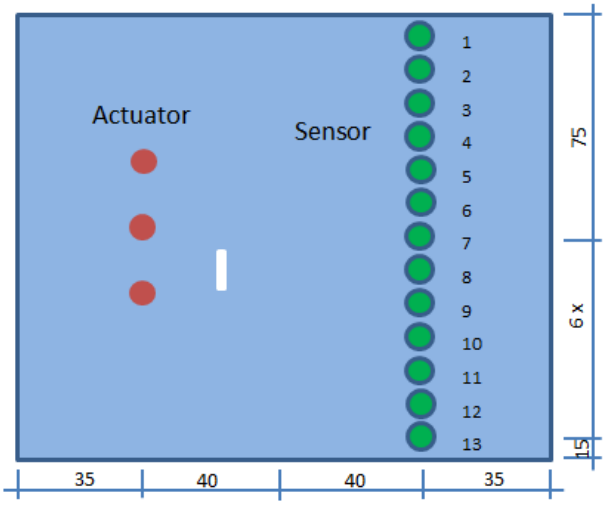

Fig. 2.29 General Crack Location with Unknown Size

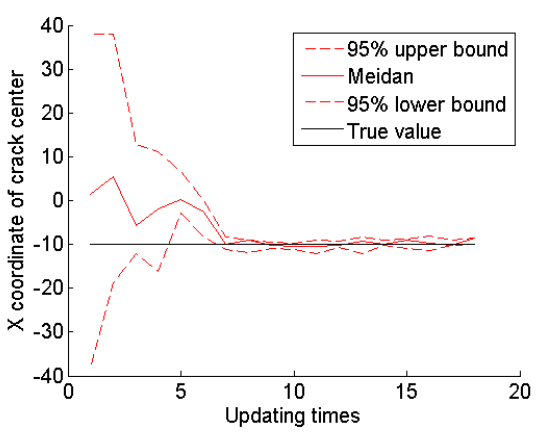

a) X coordinate prediction

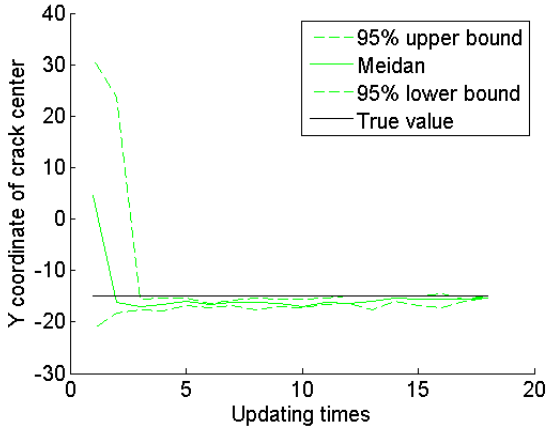

b) Y coordinate prediction

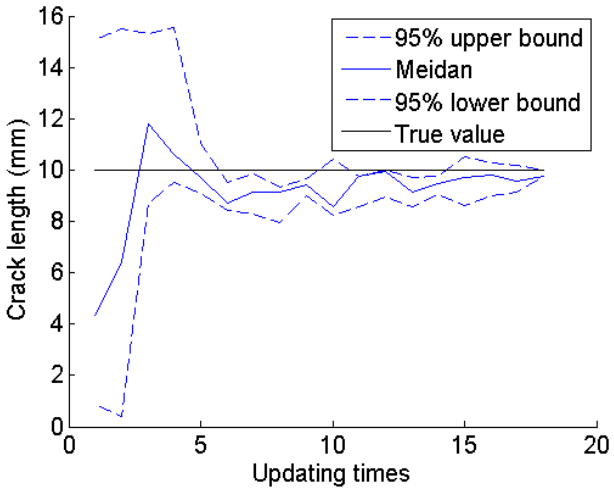

c) Crack length prediction

Fig. 2.30 Crack Location and Size Prediction for Random Damage Configuration

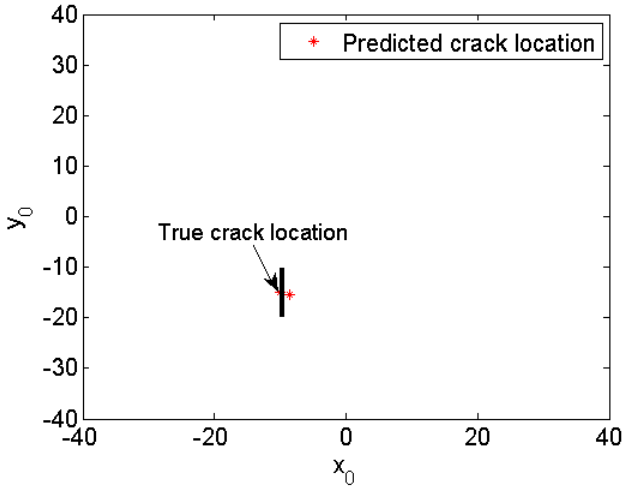

Fig. 2.31 Comparison between Predicted and True Crack Location

From Fig. 2.30, the crack size and location updated are approaching the true value after around ten updating iterations. This result can also be observed from the comparison shown in Fig. 2.31.

2.7 Conclusions

In this chapter, Lamb wave-based damage diagnosis and remaining useful life (RUL) prognosis is proposed. The proposed method is demonstrated and validated using fuselage lap joint test datasets. Finally, the model prediction is evaluated using prognostic metrics quantitatively.

It can be concluded that, by properly interpreting the changes in features of the received signal, the proposed diagnostic model provides a reasonable estimate of the crack length in lap joints. Among various crack length prediction models, the Quadratic regression model shows better results in the current investigation. Based on the demonstration example, Bayesian updating can successfully represent and manage the uncertainties introduced by model parameters and detection model. Additional measurements can greatly reduce uncertainties of prognostic estimates.

In order to consider the uncertainties from modeling and measurements for damage diagnosis, a probabilistic damage size and location updating algorithm is proposed, which incorporates the Lamb wave simulation results into Bayesian updating. It can be seen that the normalized amplitude change and correlation coefficient in the received signal are correlated with the damage size and location. The normalized amplitude change shows larger change compared to the correlation coefficient when the crack is far away from the

sensor path. Bayesian updating can represent and manage the uncertainties introduced during the damage detection, including both modeling uncertainty and measurement uncertainty. Probabilistic estimation of crack size and location can be obtained. The proposed detection algorithm can provide satisfactory median and confidence bound prediction for both centered crack and random crack location in the current investigation.

3 FATIGUE DAMAGE DIAGNOSIS AND PROGNOSIS FOR COMPOSITE MATERIALS

3.1 Introduction

Composite materials are widely used in many applications, such as rotorcrafts, aerospace, automobiles, and civil engineering structures because of their low weight and high strength properties [53-56]. However, due to lack of complete understanding of composite fatigue and corresponding failure models, it is difficult to express similar amount of trust as in metallic structures, which limits the usage and application of composite structures. Delamination and matrix cracking are the most common failure patterns for composite materials. Visual inspection is very difficult to identify this type of damage and therefore expensive and time consuming nondestructive evaluation (NDE) techniques have been extensively investigated and relied upon for composite materials. Development of structural health monitoring alternatives through continuous monitoring for the assessment of structural integrity has gained a lot of attention in recent years.

With the development of the Lamb wave-based damage detection methods, piezoelectric (PZT) sensors have been widely used for structural health monitoring because of their low cost and high efficiency. In certain modes, Lamb waves can propagate in thin plates without excessive dispersion [57] . Therefore, a typical practice in the Lamb wave-based damage detection is to use the signal features extracted from those special modes of the received signal by certain signal-processing algorithms. Several features from the received signal, such as the attenuation and phase shift, can effectively indicate the damage characteristics quantitatively [31]. A detailed review of the Lamb wave-based structure health monitoring techniques for composite materials is given in [58]. It has been shown that holes or cutting damage on composite plates can be identified using the A_0 mode of

the Lamb waves [59, 60] and its interaction with delamination in composites has been studied both experimentally and numerically [61, 62]. A method proposed in [63, 64] uses the reflected wave from the damage to detect the through-width delamination, in which the delamination location and size are determined by embedded piezoelectric material. Many simulation methods have also been developed to simulate the Lamb wave propagation within composite plates [51, 64-69]. Local defects are captured by modeling the interaction of wave and local discontinuities [51, 70, 71]. Although considerable amount of work has been done for both numerical and experimental investigation of Lamb wave-based damage detection, very few studies focused on a quantitative comparison and validation of numerical simulations.

In numerical simulation, the received signal is always clean and deterministic without considering uncertainties from measurements, modeling, and parameters. However, multiple sources of uncertainties should be incorporated in order to detect the damage in real practical scenarios. Therefore, a probabilistic damage detection method for in-situ applications is proposed in this study. The novel method is presented here to estimate damage location and the size, as along with corresponding confidence bounds. The proposed method combines the Lamb wave-based damage detection technique with Bayesian Imaging Method (BIM) to achieve these goals.

Many existing studies have been done on explicitly incorporating the different types of detected damages (e.g. cracks, delamination) in the damage evolution model for the fatigue life prediction [72-77]. Majority of these methods are based on finite element method (FEM), which focuses on the mechanisms investigation and modeling. In-situ fatigue life prognosis that directly uses these models will be very difficult due to the computational

complexity. In addition, the diagnosis and quantification of various types of damages in-situ is a challenging problem, which makes the prediction based on the high fidelity FEM model very difficult. Some researchers use an alternative approach for life prediction at the macro level, which is based on the strength or stiffness degradation induced by fatigue loading [78-83]. Whitworth [82] proposed a statistical model that describes the residual stiffness using a two-parameter Weibull distribution. In [83], a normal distribution was proposed to predict the residual stiffness of composite laminates. In both approaches, the residual stiffness model ignores the effect of applied stress which is generally not true for fatigue problems. Shirazi and Varvani-Farahani [84] proposed to use the stiffness degradation to develop a fatigue damage model for a unidirectional fiber-reinforce polymer (FRP) laminates system. A relationship between the stiffness reduction and the remaining fatigue life ratio was developed. This model is relatively difficult for the in-situ fatigue prediction because the field measurements for stiffness are very difficult and the knowledge of ultimate fatigue life is not available beforehand. Unlike the stiffness measurement in the laboratory conditions, it is difficult to obtain stiffness reduction measurements directly under service conditions. Thus, it would be desirable if the stiffness degradation can be inferred using a feasible structural health monitoring system. Based on the fact that Lamb wave propagation is highly dependent on material stiffness, it is expected that stiffness degradation will be captured by the received Lamb wave signal propagating through the specimen. Since piezoelectric sensors are embedded in the structure, system health can be measured in-situ on a continuous basis, which lays foundation for more accurate RUL prognosis.

The objective of this chapter is to first develop a new co-simulation framework to include the delamination and matrix cracking effect simultaneously to explain the observed changes in wave signal due to different damage types and intensities. Parametric studies are used to investigate the sensitivity of model parameters on the simulation results. Following this, a probabilistic delamination size and location detection framework is proposed using Bayesian imaging method (BIM). Damage diagnosis uncertainty bounds are generated simultaneously by considering measurement and model uncertainties. After that, an in-situ fatigue life prognosis framework is proposed based macro level stiffness degradation. Lamb wave signals are used for specimen stiffness degradation detection, which is incorporated in the Bayesian inference for real time reaming useful life (RUL) prediction. Finally, some conclusions and future work are generated based on the current investigation.

3.2 Fatigue Testing for Composite Coupons

Fatigue experiments were conducted using composite coupons with 12 plies. Torayca T700G uni-directional carbon-prepreg material was used for this $15.24\ \text{cm} \times 35.56\ \text{cm}$ dog bone geometry coupons and an edge notch (5.08 mm × 19.3mm) was introduced to induce stress concentration, as shown in Fig. 3.1.

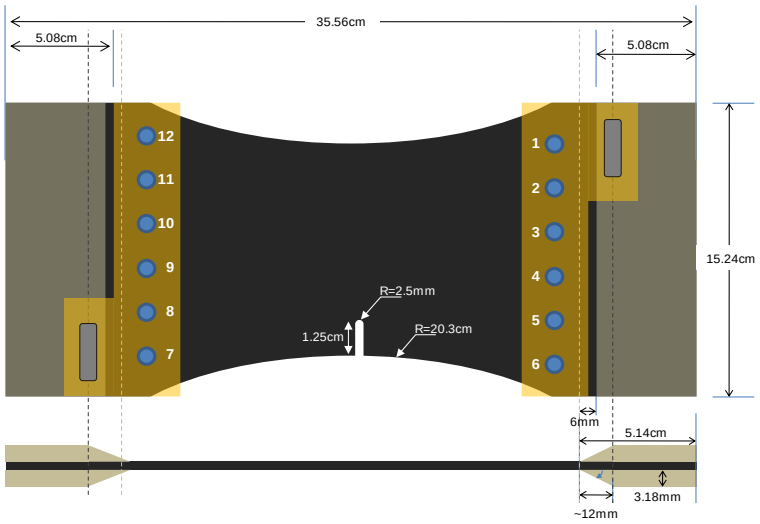

Fig. 3.1 The Geometry of the Dog Bone Coupon

These experiments served for several objectives - (i) collection of run-to-failure data with periodic system health data using PZT sensors, (ii) collection of ground-truth data (X-ray imaging) for the delamination to validate the sensor measurement analysis, (iii) accounting for variations between samples of same internal structure (layup), and (iv) characterizing variations between samples of different internal structures. Three symmetric layup configurations were chosen to account for the effect of the ply orientation: Layup 1: $[0_2/90_4]_2$, Layup 2: $[0\ /90_2\ /45\ /{-45}\ /90]_2$, and Layup 3: $[90_2\ /45\ /{-45}\ ]_2$. Two six-PZT sensor SMART Layers from Acellent Technologies, Inc (Fig. 3.2(a)) were attached to the surface of each sample. In Fig. 3.2(a), actuator 1 to 6 were used to actuate the PZT signal and sensors 7-12 were used collect the corresponding signal propagation through the plate. Each actuator and sensor acted as a diagnosis path to interrogate the damage information. A more detailed description about these experiments is given in [85]. Fig. 3.2(a) shows such a path form actuator 5 to sensor 8, which is represented as path 5⟶8. The other paths follow the same rule as above in the following sections.

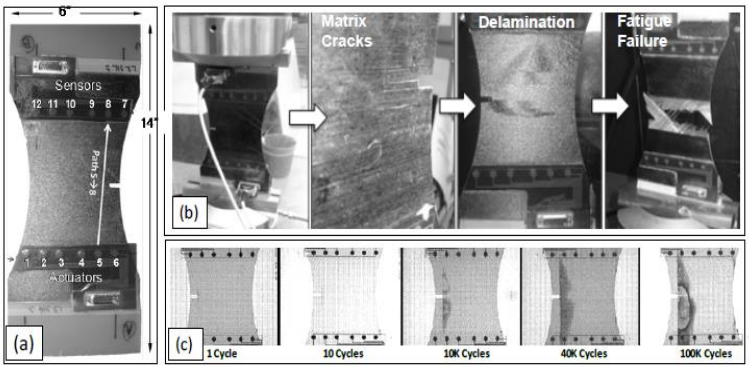

Fig. 3.2 (a) Coupon Specimen, Smart Layers Location, and Diagnostic Path From Actuator 5 to Sensor 8, (b) Development of Matrix Cracks and Delamination Leading to Fatigue Failure,(c) Growth in Delamination Area During the Increased Loading Cycles.

Using this configuration of sensor network, all PZTs are used one by one as actuator to actuate the Lamb wave, which is received by other acting as sensors. It is expected that the growth in delamination size will be captured in the received signal from a particular diagnosis paths that cover the delamination area (e.g. path 5⟶8), which was validated by the comparison between features and delamination size in literature[85]. For diagnosis path 5⟶8, the signal received by sensor 8 at different loading cycles is plotted in Fig. 3.3. As illustrated in Fig. 3.3, an increase in delamination size can be captured by monotonic trends in features (amplitude, correlation coefficient, and phase change). Conceptually, a change (decrease) in normalized amplitude reflects the energy dissipation due to the damage. The phase angle change is attributed to the increased wave traveling distance induced by the damage. The correlation coefficient change reflects the signal perturbation due to the new waves generated at the damage surfaces due to reflections [7]. All of these features are computed by comparing the received signal from a pristine coupon, called baseline and the signal from damaged coupons.

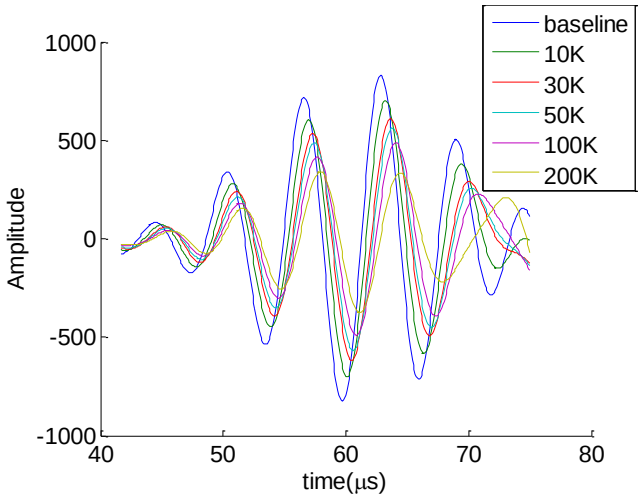

Fig. 3.3 Changes in Signal Received at Sensor 8 with Increased Fatigue Cycles

3.3 Numerical Simulation for Lamb Wave Propagation within Composite Coupons

Many numerical methods have been developed to simulate the propagation of Lamb wave within a thin plate. In this part, a finite element model (FEM) is developed by coupling the piezoelectric and mechanical elements using the commercially available code ABAQUS.

3.3.1 Finite Element Modeling

The FE model geometry is chosen identical to that discussed in section 3.2. The FE model and the orientation of each ply are schematically shown in Fig. 3.4. The composite plate is finely meshed using 8-node 3-D brick element and the right and left end of the specimen are fixed for all degree of freedoms (DOFs). Six actuators and six sensors are attached on the composite plate and perfect bonding is assumed between them. The PZT disks are meshed using piezoelectric C3D8E elements. The electric potential for the top and bottom surfaces of the piezoelectric disk is coupled to the master nodes assigned to each surface. The actuating signal is applied at the master node of the actuator's top surface and the reaction electrical chaFgiurge can be monitored at the master nodes of the sensors'

top surfaces. During simulation, the master nodes on the bottom surfaces are set to be zero electrical boundary condition. The PZT sensor property is characterized by its polarization direction, which is illustrated as the axis-3 in Fig. 3.5. This polarization direction is identical with the normal direction of composite plate the FE model. The mechanical constants of the composite material and the piezoelectric constants of the sensors are given in Table 3.1 and

Table **3.2**, in which 1 mean horizontal direction (i.e. x-axis), 2 means vertical direction (i.e. y-axis), and 3 means normal direction (i.e. z-axis).

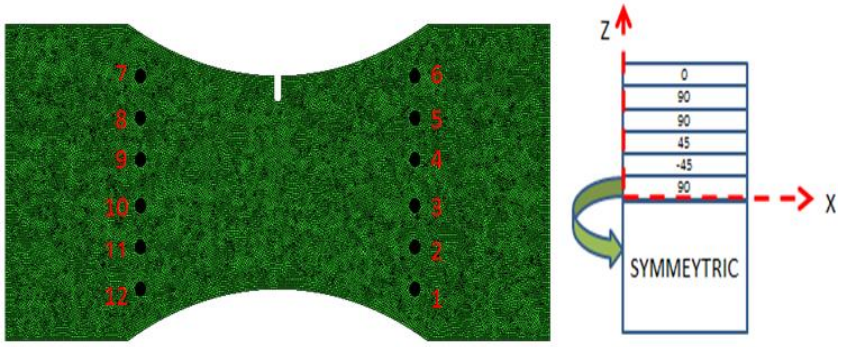

Fig. 3.4 Sensor Layout and Orientation for Each Ply

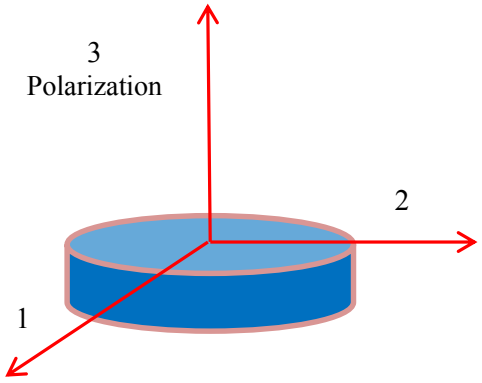

Fig. 3.5 The Local Coordinate of the PZT Sensor

Table 3.1 The Mechanical Constant of the Composite Material

Elastic	E_{11}	E_{22}	E_{33}	υ_{12}	υ_{13}	υ_{23}	G_{12}	G_{13}	G_{23}

constant(Gpa)	127.5	8.4	8.4	0.31	0.31	0.36	6.2	6.2	3.4

Table 3.2 The Piezoelectric Constant of PZT Sensors

Dielectric $(10^{-8}F/m)$	E_{11}	E_{22}	E_{33}	Piezoelectric $(10^{-10}V/m)$	d_{11}	d_{22}	d_{33}
	0	0	1.68		-1.9	-1.9	-4.5

It is suggested in the literature that a hamming windowed sinusoidal tone burst with 5.5 cycles can be used for the damage detection [60]. The central frequency of this signal is set at 150 kHz, as shown in Fig. 3.6. Since the actuator is attached on only one side of the composite plate, both symmetric mode and anti-symmetric modes will be actuated. For current frequency thickness product (i.e. 270 Hzm), the dominant Lamb wave mode should be S_0 mode based on the wave speed dispersion curve. The PZT sensors can actuate and receive Lamb waves by coupling with in-plane stain motion [86]. Therefore, the Lamb wave mode can be justified by extracting the in-plane displacement on the symmetric side of the composite plate. Fig. 3.7 shows the schematic representation of the Lamb wave mode and the x, y displacement of these two nodes.

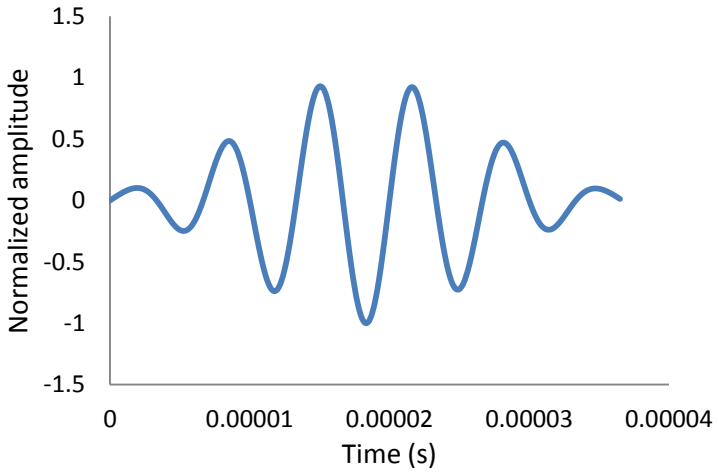

Fig. 3.6 A Tone Burst Signal of 5.5 Cycles with 150 kHz Central Frequency

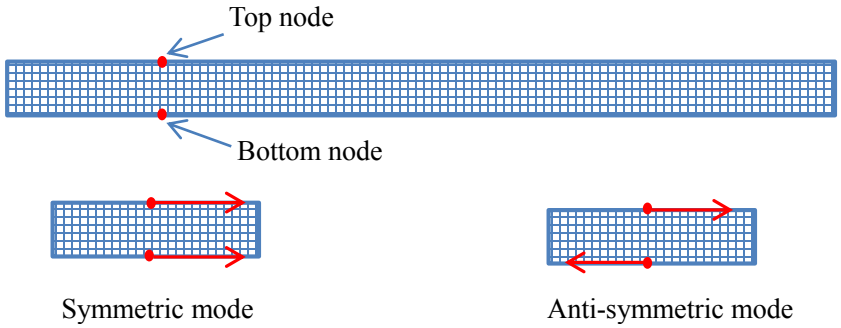

(a)

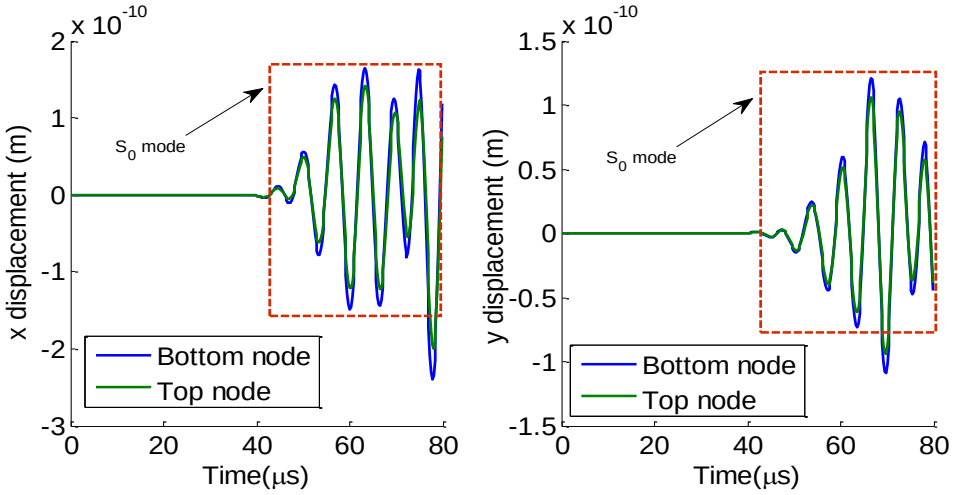

(b)

Fig. 3.7 Extracted X, Y Displacement of the FE Model.
(a) Schematic Representation of the Lamb Wave Mode, (b) The Extracted X, Y Displacement.

3.3.2 Convergence Analysis and Parameter Tuning

In order to evaluate the convergence of the finite element solution, a convergence analysis was conducted with respect to the element size and time increment. In general, the accuracy of the FE model should increase as element size is further refined and smaller

time increments are used, which of course in turn results in longer computational times. Therefore, a balance needs to be maintained between these factors.

For Lamb wave propagation, certain criteria should be satisfied when choosing the critical element size and a time step. It is required that there are at least ten elements within the smallest wavelength and there are at least twenty time steps within a cycle of wave at the highest frequency [87]. The time of arrival (ToA) is an important factor for damage detection and is used as a metric to evaluate the convergence of calculation. The time of arrival (ToA) for different time increments is shown in Fig. 3.8. The mesh size convergence study is conducted under defect condition, in which both delamination and matrix cracking exist. The ToA and amplitude against different mesh size are given in Fig. 3.9. It is observed that when the time increment and the element size are small enough, the relative variation of the solution is small (i.e., an asymptotic behavior). For a balance between computational efficiency and accuracy, the time step is set to be $0.25\mu s$ and element size is set to be 0.45 mm. In that case, there are four elements through the thickness, which can ensure convergence of the received signal for both ToA and amplitude features.

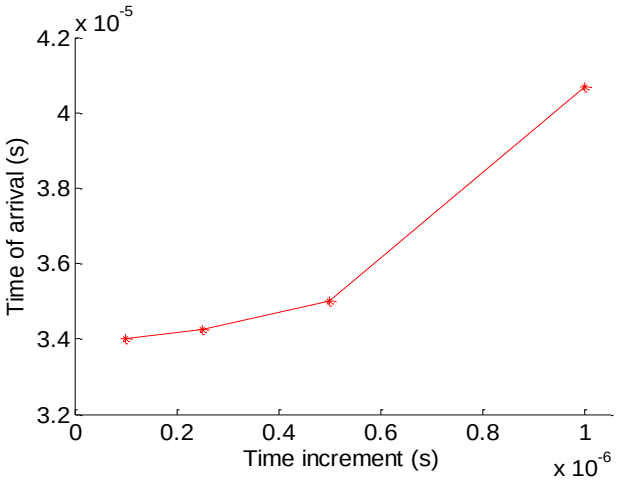

Fig. 3.8 The ToA for Different Time Increments

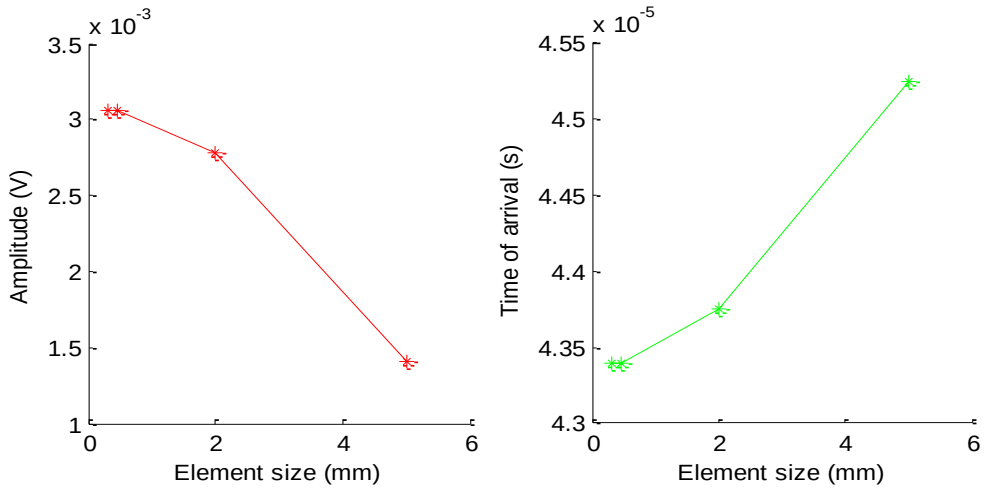

Fig. 3.9 The ToA and Amplitude for Different Mesh Sizes under Defect Conditions

The first time window of the simulation is compared with that of experiment under the pristine condition. Due to various uncertainties associated with materials (e.g., initial void count, size, and locations, inhomogeneity and anisotropy of materials, and manufacturing variations), the basic material properties, such as Young's modulus and density, need to be calibrated. Because of the anisotropy of the composite laminates, the wave speed is a complex function of elastic properties (i.e., unlike the isotropic solids). Eq.(3-1) is used for the model calibration and is a simplified approximation based on the solution for isotropic solids. The results show that this simplification can greatly reduce the model calibration work and give satisfactory agreement between FE simulation and experimental measurements.

$$v \propto \sqrt{\frac{E}{\rho}} \tag{3-1}$$

where E is the Young's modulus and ρ is the density. Since material density usually varies during the manufacturing process, it is chosen as one of the parameters to be tuned in the

FE model. Based on the online database [88], the material density is assumed to be $1780kg/m^3$ initially. By tuning the parameter ρ, the received signals for the experiment and simulation are given in Fig. 3.10.

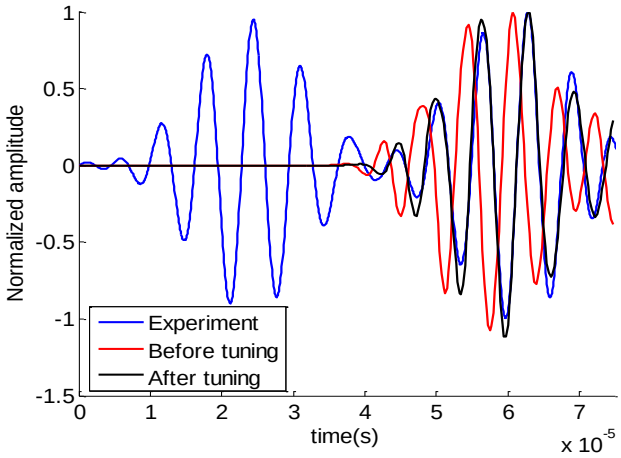

Fig. 3.10 Model Parameter Tuning for FE Simulation

As shown in above figure, the numerical simulation can match the experiment for the wave propagation velocity when the material density is tuned to be 2220kg/m^3. This value is used in the rest of the analysis.

3.3.3 Delamination Modeling

Due to the high stress concentration around the notch tip, delamination initiates at this location as expected. Based on the X-ray images from the experiment, the delamination initiates between the middle layer and grows gradually as applied higher loading cycles. In the FE model, the nodes for the two semi-elliptical areas between the 6th and the 7th ply of the composite plate are released, with other parts of these two plies connected using tie constraint. Fig. 3.10 shows an example of X-ray image and FE model of the delamination for different loading cycles.

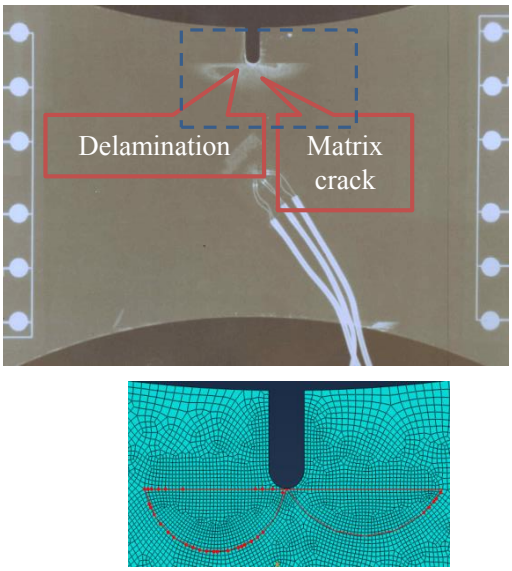

Fig. 3.11 X-ray Image and FE Model for Delamination

First a numerical simulation is carried out to observe the simulated wave propagation signal with delamination damage alone (Fig. 3.12).To compare with the experiment, the signal on diagnosis path 5⟶8 is collected correspondingly. The received signal package shows slight changes between the pristine conditions and the damaged conditions. This trend observed is different from the observations from the experimental testing, which indicates that the delamination along does not fully explain the changes in the Lamb wave signal and other types of damages must be included for a comprehensive investigation.

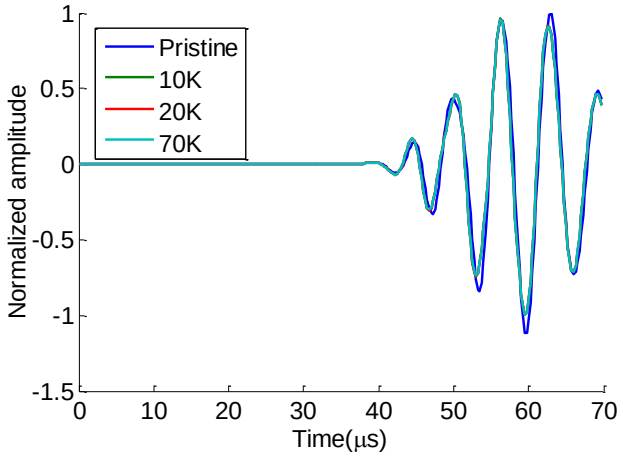

Fig. 3.12 The Simulation Signal Received by Sensor 8 for Delamination Damage Modeling

3.3.4 Co-simulation of Delamination and Matrix Cracking

Experimental data (Fig. 3.2(a)) suggest that matrix crack are always present before delamination is initiated. Therefore, changes in the features during fatigue cycles may be induced by a combination of delamination damage and matrix cracking. In that case, matrix cracks should be modeled simultaneously in order to represent the true material condition. It is very time consuming, if not infeasible, to model every single matrix crack in the finite element simulation. Therefore, in this research a simplified algorithm was used to include the matrix crack for the co-simulation. The key hypotheses are: 1) the matrix cracks mostly exist close to the delamination region; 2) the matrix cracks are uniformly distributed in the targeted high stress region. The matrix crack is modeled by taking a very thin slit in the FEM model. In the current study, the width of the crack is 0.1 mm, which is determined by the convergence study. The number of cracks is from experimental record and the crack length is assumed be the same with the delamination size from the X-ray images. A schematic representation of the matrix crack distribution is given in Fig. 3.13(b).

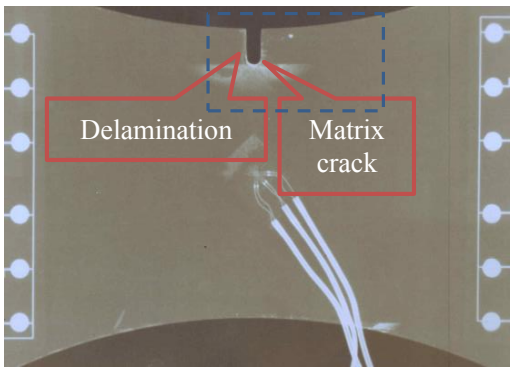

(a)

(b)

Fig. 3.13 Experimental and Numerical Representation of Damage.
(a) X-ray Image from Experiment, (b) Schematic Representation of the Matrix Crack.

Following the procedure discussed above, the FE model with the combination of delamination and matrix crack can be developed and the corresponding signal for the delaminated/cracked condition is recorded. Fig. 3.14 illustrates the simulation signal received by sensor 8 under different loading cycles. Comparing the simulation results in Fig. 3.14 and experimental observations in Fig. 3.2, the simulated signal trend qualitatively agrees with that from the experimental testing.

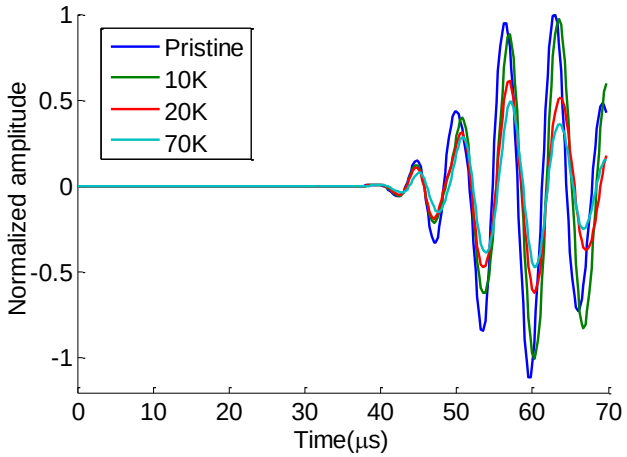

Fig. 3.14 The Simulation Signal Received by Sensor 8 for Co-simulation of Delamination and Matrix Cracking

In addition to the qualitative comparison as shown above, signal features are extracted from received signals for data reduction, damage diagnosis and prognosis. It has been shown that the normalized amplitude change, correlation coefficient, and phase change are

good feature candidates for the fatigue damage detection and quantification for metallic structures [10] . In the following analysis, these three features are used for comparisons as quantitative validation, which are presented in Fig. 3.15. The x-axis is the delamination size and the y-axis represents the feature values. As can be seen a good agreement is observed between the simulation results and experimental data for most part, but there is still difference between simulation and experiment. Further analysis of experimental data were required to identify the reason for the difference. One possible reason is that the true matrix crack configuration cannot be simulated accurately. However, the proposed co-simulation framework is shown to be able to model the change in wave signals, which are of critical importance from the prognosis point of view. It must also be observed that that the three features that were identified have unique monotonic trends with the damage progression. This supports the hypothesis that they can serve as the potential damage indicators in SHM applications, at least for the components similar to those used in this study. Further experimental and numerical research is required for other types of composite components and material properties.

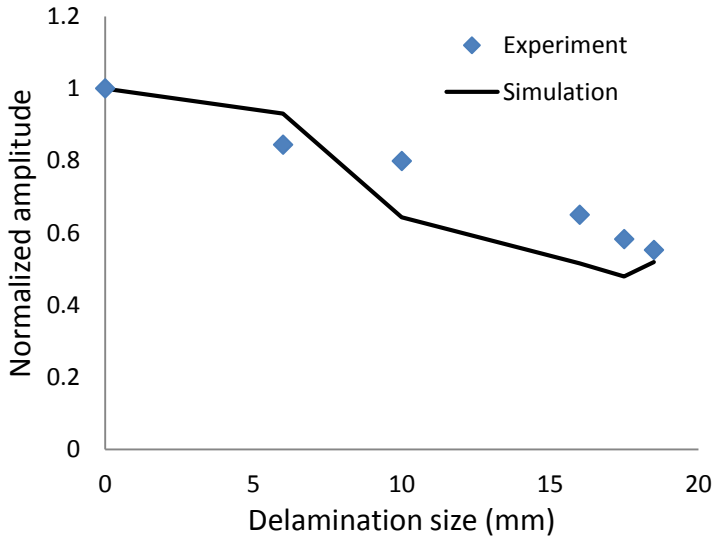

(a)

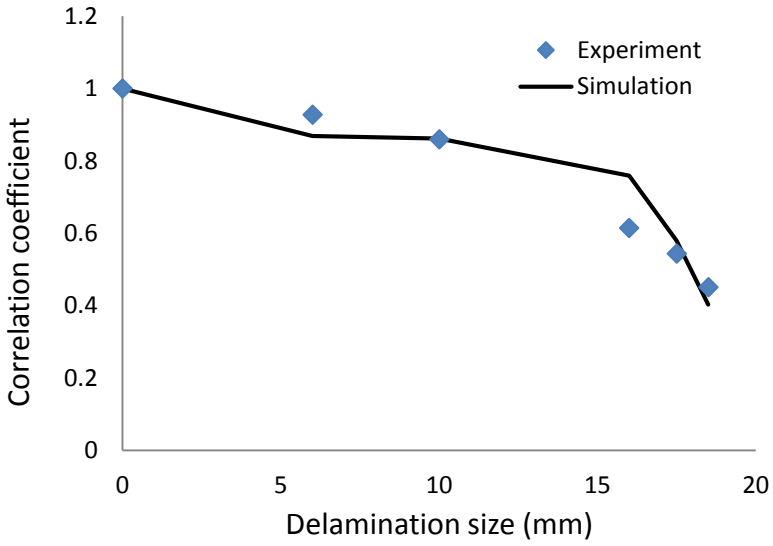

(b)

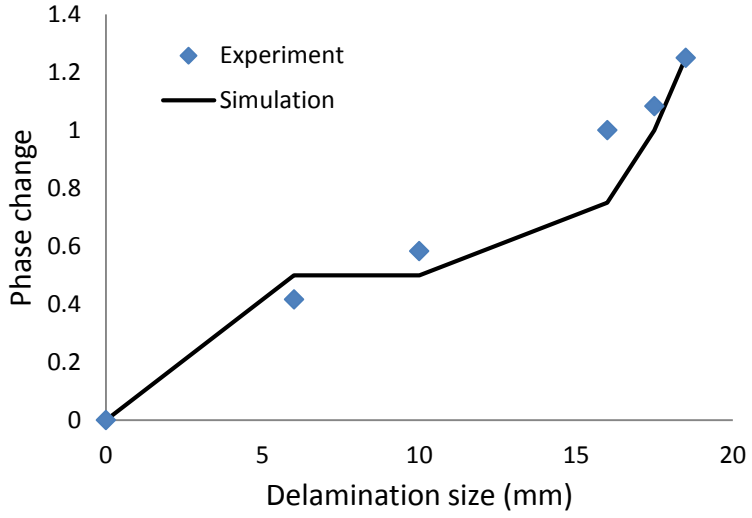

(c)

Fig. 3.15 Features Comparison between Experiment and Simulation

3.3.5 Sensitivity Analysis

Another important aspect for a comprehensive numerical simulation study of the wave propagation is the parametric sensitivity analysis of model parameters. This is important to show the impact of model hypotheses on the final simulation results. For instance, in the experimental measurements there is no information available for matrix crack extension in the thickness direction. This is partially due to the limitation of NDE techniques available

for use in the experiments. The modeling approach, however, needs this information and hence has to make an assumption about this information for the simulation. The impact of this assumption must be investigated. In the proposed parametric study, the matrix crack depth, gaps, and lengths are investigated (as shown in Fig. 3.16). The corresponding sensitivity analysis of these three parameters is given in Fig. 3.17, in which three features for each modeling parameter are illustrated. The x-axis represents the investigated parameters and the y-axis is the corresponding features.

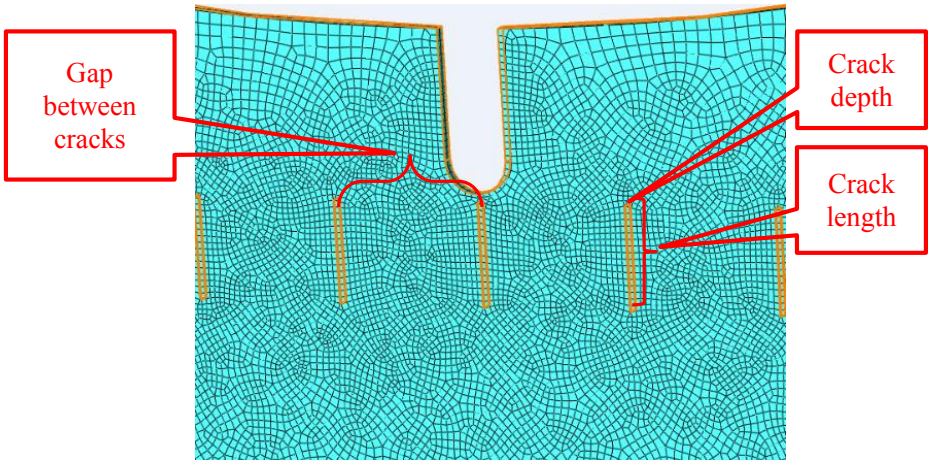

Fig. 3.16 The Three Parameters That Determine the Matrix Crack Configuration

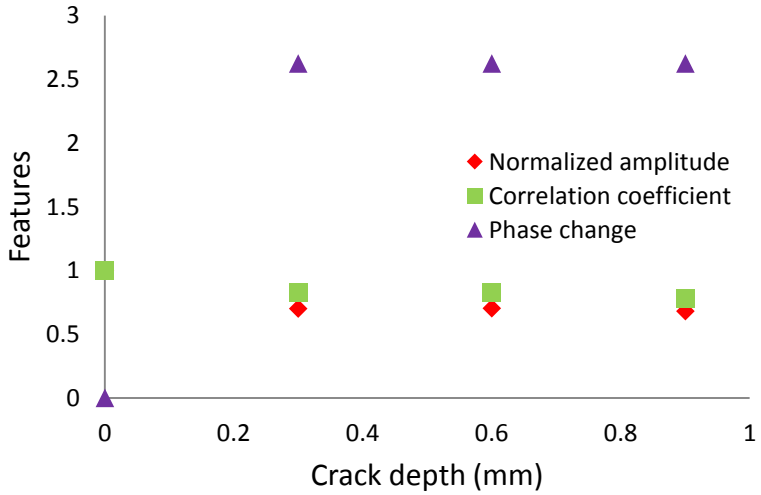

(a)

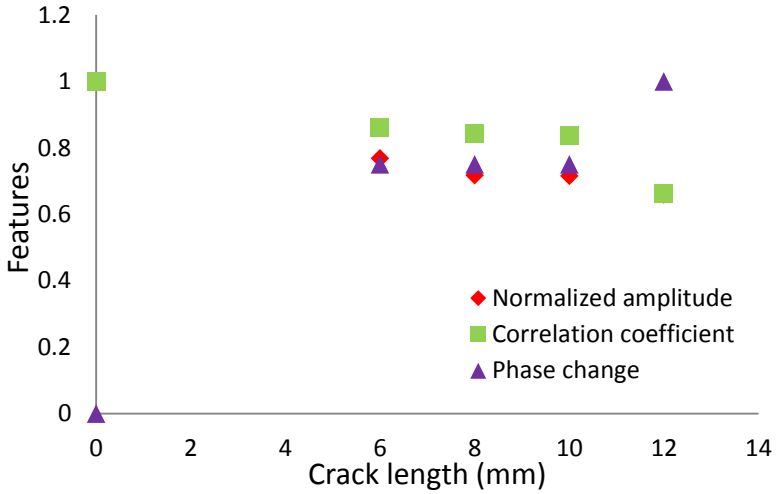

(b)

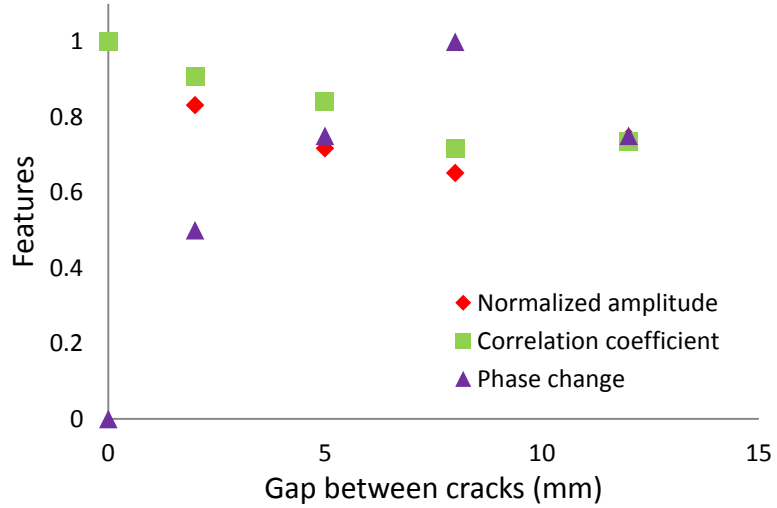

(c)

Fig. 3.17 The Sensitivity Analysis for Three Parameters

From Fig. 3.17, it can be seen that these three features show similar trend for each model parameter. They are not sensitive to the matrix depth change, if the depth is beyond a certain value. The matrix crack gap and length have significant effect on the received signal features, which must be carefully included in a FEM framework for Lamb wave propagation analysis. For the current analysis, they are not quantitative incorporated because of the limitation of current NDE technique.

3.4 Delamination Size and Location Diagnosis Using Bayesian Imaging Method

In section 2.6, a crack size and location detection framework is proposed for aluminum using the numerical results from the finite element method (FEM), in which the uncertainty can be strictly controlled. There will be more sources of uncertainties if we want to build the detection framework from experiment point of view. To apply this method for the composite delamination, two critical problems should be solved, (1), how to predict delamination area with only one dimensional signal features; (2), how to incorporate various uncertainties in the real composite experiment. In this section, a probabilistic delamination localization and size detection framework using Bayesian imaging method (BIM) is developed. This proposed method is also demonstrated and validated using the experimental datasets.

3.4.1 Damage Diagnosis and Bayesian Imaging Development

The introduction for Bayes' theorem and uncertainties management are given in section 2.4.1. In order to utilize Bayesian theorem for delamination size and location detection, it is essential to build a model $M(\theta)$ describing the relationship between the signal features and damage information, which is developed using information extracted from available testing datasets. Next, a likelihood function for the updated parameters, i.e., delamination size and location is built considering the measurement and model uncertainties. The posterior belief about damage can be estimated from the posterior distribution of the updated parameters. In this case the parameter vector θ comprises of delamination geometric center coordinate (x_0, y_0) and delamination size a. Since no prior belief is available for any of these three parameters, the prior distributions of x_0, y_0 are assumed to be uniform distribution over the entire possible region where the delamination may appear.

The delamination size distribution is uniformly distributed from zero to a large size (e.g, the physical length of the specimen as the largest possible delamination size). A very small quantity (i.e., 0.001 mm) for the delamination distribution lower bound is used to avoid numerical difficulties. The overall diagnosis framework in the proposed study is shown in Fig. 3.18.

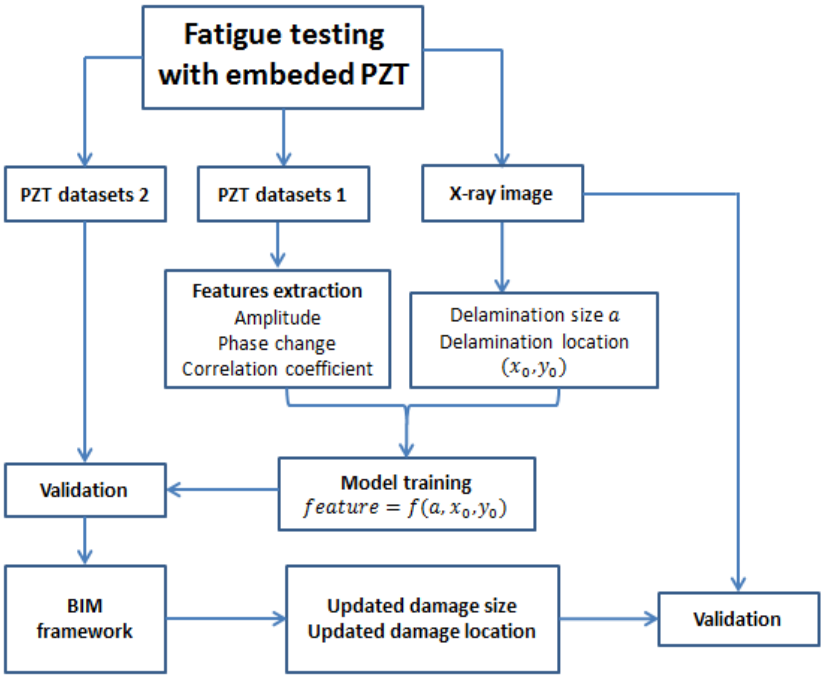

Fig. 3.18 Flowchart for the Damage Diagnosis Method

In Bayesian updating, it is nontrivial to derive an analytical solution if the posterior distribution is non-parametric or very complex, which is the case in this problem. Therefore, the Markov-Chain Monte-Carlo (MCMC) method is used to draw samples.

The key idea behind the proposed BIM is that the entire specimen is discretized into many small cells (e.g., with size $1\text{mm} \times 1\text{mm}$ in the current study) and each cell is assigned an associated probability of damage. The probability of damage is updated based on measured signal features using the Bayesian technique. The updated posterior distribution at each cell can be used to construct an image that directly represents the

damage location and size.

3.4.2 Data Processing of the Composite Coupon Fatigue Testing

The experiment data for the composite coupon testing discussed in section 3.3 is processed in this section. A model $M(\theta)$ describing the relationship between the signal features and damage information is developed based on the extracted damage identification features.

Observation from X-ray images of the damaged coupons reveal that damage grows from the tip of the slit to semi- elliptical shapes, approximately. Therefore, damage shapes are modeled as half elliptical lobes. Using the sensor network and the analysis method described above, there are two parameters describing these half elliptical shapes that would possibly affect the received signal, which is shown in Fig. 3.19. The green ellipse is the delamination area observed from the X-ray and the red envelop is introduced to cover the entire area, whose radius is used as a damage parameter for delamination size a. The distance from the delamination center to the diagnosis path is denoted by d. For a given layup specimen (e.g., L2S11_F in this case), features can be extracted from the collected PZT datasets and the corresponding features for actuator 5 is given in Fig. 3.20.

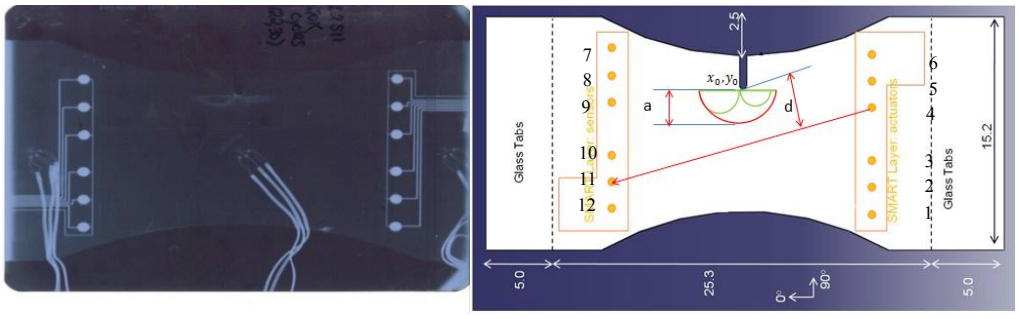

Fig. 3.19 X-Ray Image and Schematic Representation of Delamination

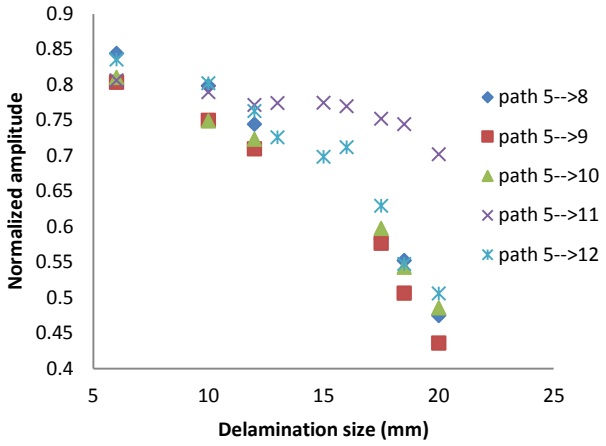
Normalized amplitude
0.9
0.85
0.8
0.75
0.7
0.65
0.6
0.55
0.5
0.45
0.4
5
10
15
20
25
Delamination size (mm)
path 5-->8
path 5-->9
path 5-->10
path 5-->11
path 5-->12

(a)

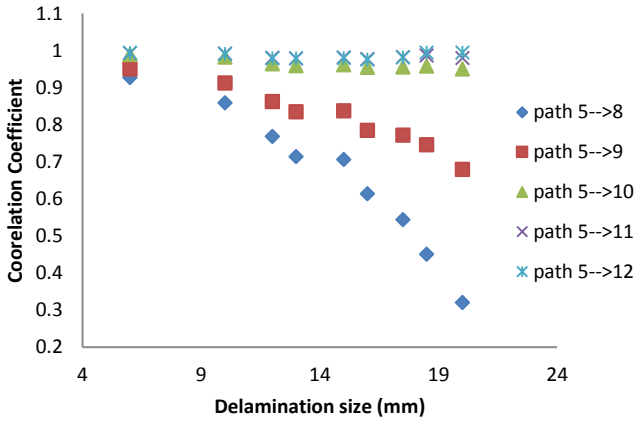
Coorelation Coefficient
1.1
1
0.9
0.8
0.7
0.6
0.5
0.4
0.3
0.2
4
9
14
19
24
Delamination size (mm)
path 5-->8
path 5-->9
path 5-->10
path 5-->11
path 5-->12

(b)

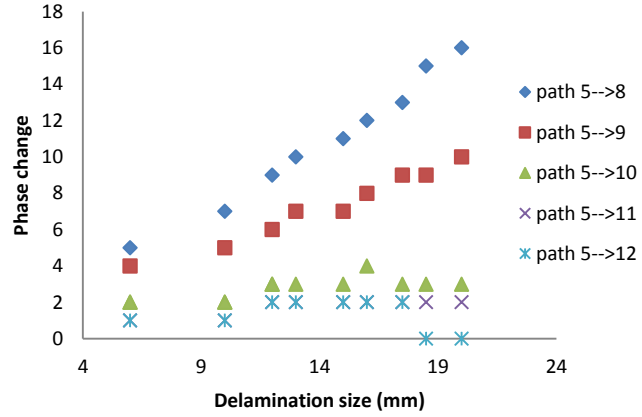
Phase change
18
16
14
12
10
8
6
4
2
0
4
9
14
19
24
Delamination size (mm)
path 5-->8
path 5-->9
path 5-->10
path 5-->11
path 5-->12

(c)

Fig. 3.20 Features Related to Actuator 5 for Different Delamination Size and Distance. (a) Normalized Amplitude, (b) Correlation Coefficient, (c) Phase Change.

As shown in Fig. 3.20, the correlation coefficient and phase change features are more sensitive to the distance compared to the normalized amplitude. For example, for a fixed distance, these two features have monotonic relationship with the delamination size, which is consistent with the trend in Fig. 3.3. In order to use these two features in the proposed BIM, a model is introduced to express the relationship between the features with the delamination size and position. A generic expression can be written as

$$feature = f(a, d) \tag{3-2}$$

where a is the delamination size, d is the distance from the delamination center to the direct diagnosis path. It should be noted that Eq.(3-2) is a generic expression and does not limit to a specific function type. In this study, a polynomial regression model is used. Using the trend in the datasets, the model used for these two features is given as

$$feature = f_1(d) \times a^2 + f_2(d) \times a + f_3(d) \tag{3-3}$$

where $f_i(d) = \beta_{i1} \times ln(d) + \beta_{i2}$ for correlation coefficient. β_{ij} is the regression coefficient, which can be obtained by learning from the training datasets. After tuning these coefficients, the testing and fitted results for features are shown in Fig. 3.21. The yellow circular dots are the validation data and the rest are used for the training. It is can be seen that the simple regression model above gives satisfactory results except for the regions where the delamination is far away from the diagnostic path.

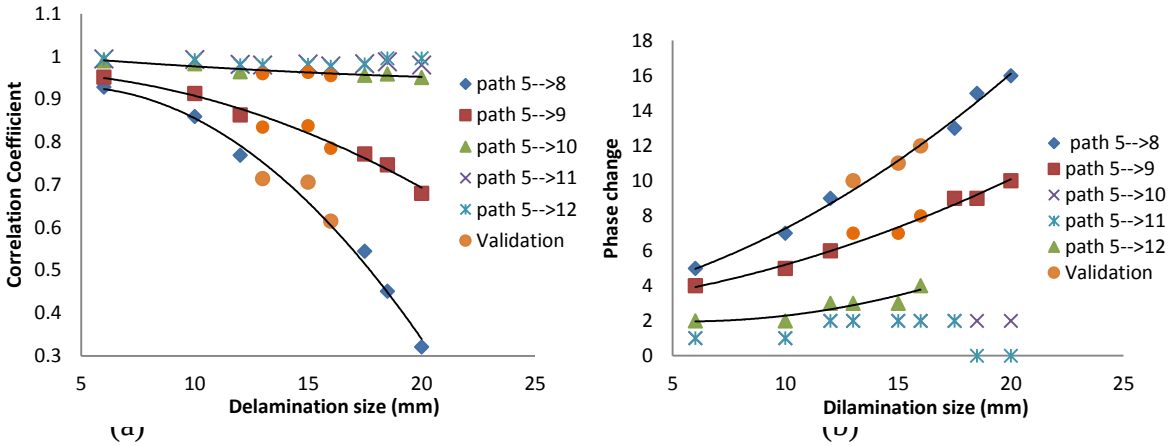

Fig. 3.21 The Testing Data and Curve Fitting

The data analysis presented above is from a single actuator (actuator 5). Similar trends are observed for data from other actuators. For a given delamination defect, damage information from different actuators and wave paths can be combined to provide a better estimation of the delamination size and location. The following section presents an example of the BIM demonstration and validation.

3.4.3 Demonstration Examples

As described in section 3.4.1, the model $M(\theta)$ is needed to show the relationship between damage information and signal features, which can be substituted by the fitting model shown in Eq.(3-3). The posterior belief about the damage is estimated by the posterior distribution of the updated parameters. Parameter θ represents the delamination center coordinate (x_0,y_0) and delamination size a. Since no prior belief is available for these three parameters, the prior distribution of location is assumed as $x_0 \sim \mathrm{U}(93.5,259.5)$, $y_0 \sim \mathrm{U}(25,125)$, which covers all the possible location where delamination may appear. The coordinate definition of this specimen is given in Fig. 3.22. The delamination size distribution is assumed as $a \sim \mathrm{U}(0.001,18)$, where U means uniform distribution. The

likelihood function is developed based on the difference between fitting model and real experimental data. The measurements from actuator 5 and 6 are utilized in Bayesian updating, as given in Table 3.3. It should be noted that each updating iteration incorporates one measurement in the BIM framework. The aspect ratio for the delamination area is assumed to be 2.5 based on the experimental X-ray image.

Table 3.3 The Sensor Measurements for Given Delamination

Actuator / Sensor	5		6	
	Correlation Coefficient	Phase change	Correlation Coefficient	Phase change
8	0.7142	10	0.6858	10
9	0.8351	7	0.8279	7
10	0.9595	3	0.9476	4

The posterior distribution of (x_0, y_0, a) can be estimated by the samples drawn using the MCMC, which updates the belief about the delamination location and delamination size at each updating iteration. At the same time, corresponding median and uncertainty bound predictions are computed to describe the accuracy of each updating result. The delamination location estimates after each updating iteration are shown in Fig. 3.23.

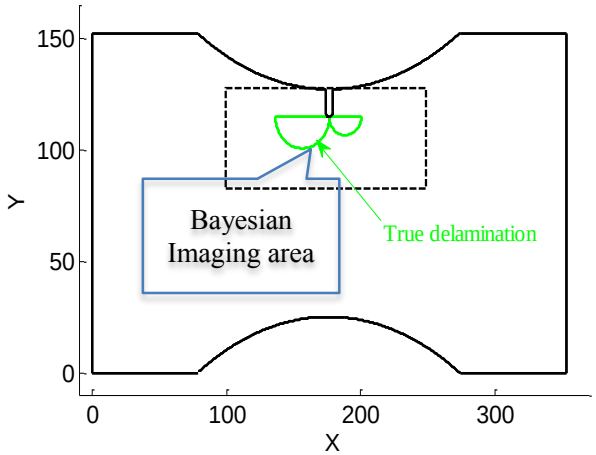

Fig. 3.22 The Definition of the Sample Coordination and Specific Area to Show the Bayesian Image

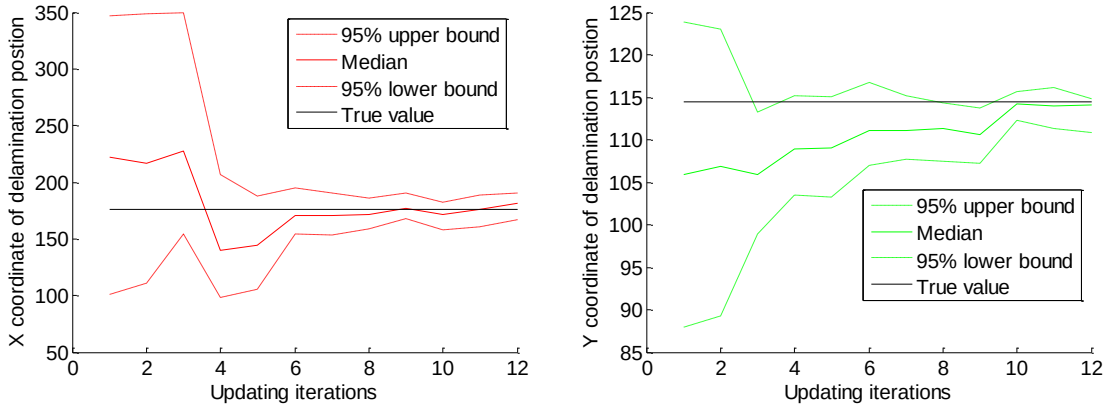

Fig. 3.23 The Delamination Location Updating

As shown in Fig. 3.23, the estimated delamination location is approaching the true location as more data are used for the updating. Additionally, the uncertainty bounds narrow down as more measurements become available. Fig. 3.24 illustrates the Bayesian imaging of the damage probability at each cell of the specimen. It is obvious that the possible delamination area is narrowed down and the probability is increasing as more updating observations are available. At the final updating, the location with the highest probability is considered as the most probable delamination centers, which is almost the same with the true value as show in Fig. 3.24(d).

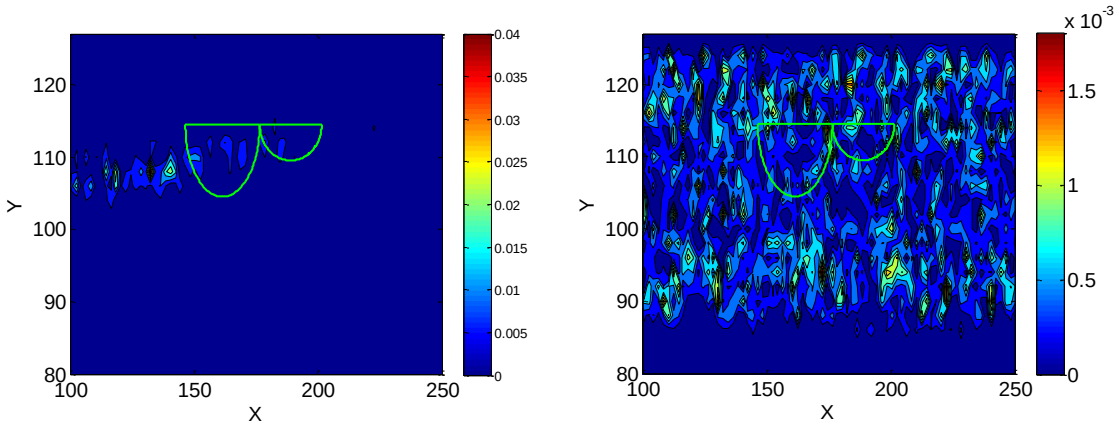

(a) One updating iteration (b) Four updating iterations

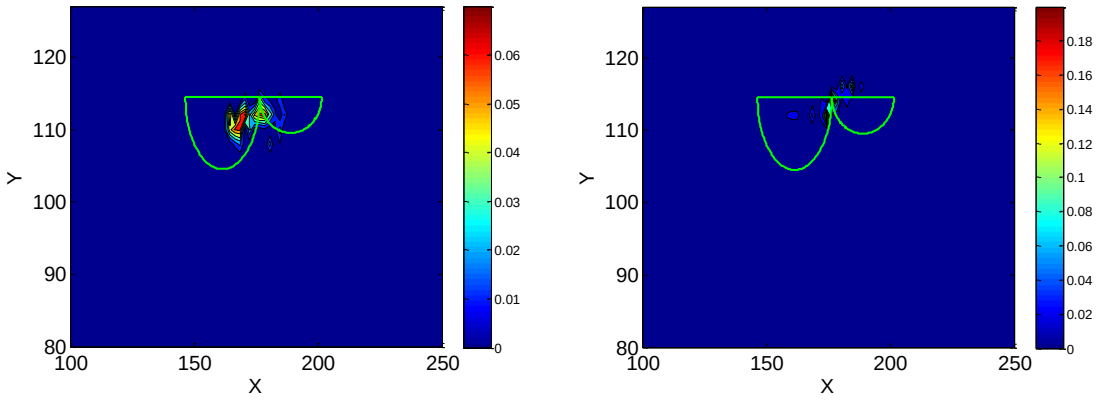

(c) Eight updating iterations (d) Twelve updating iterations

Fig. 3.24 Bayesian Images of the Damage Probability at Each Cell of the Specimen

Simultaneously, delamination size is updated gradually, as shown in Fig. 3.25. By incorporating the location and size information, the estimated delamination area can be calculated. Fig. 3.26 gives the comparison between the true delamination from the X-ray images and the updated results using the proposed BIM. Satisfactory agreement is observed.

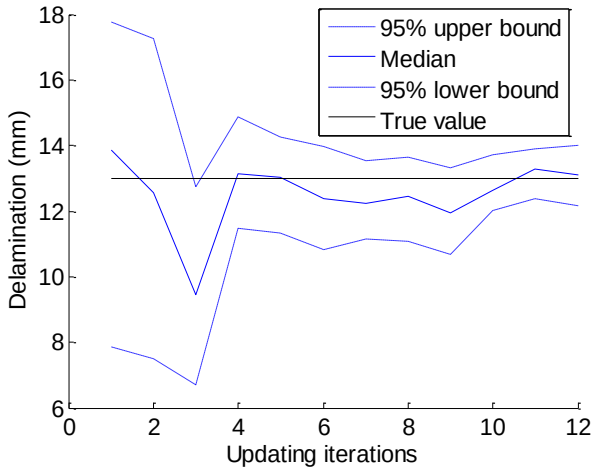

Fig. 3.25 The Delamination Size Updating

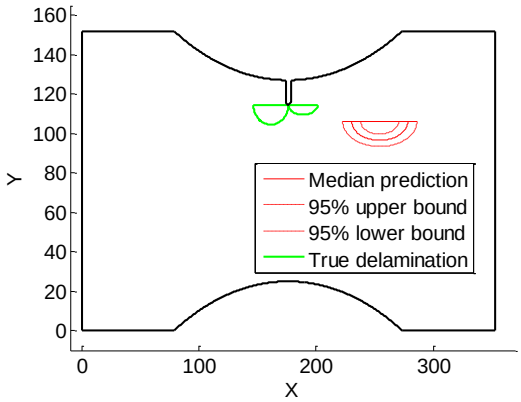

(a) One updating iteration

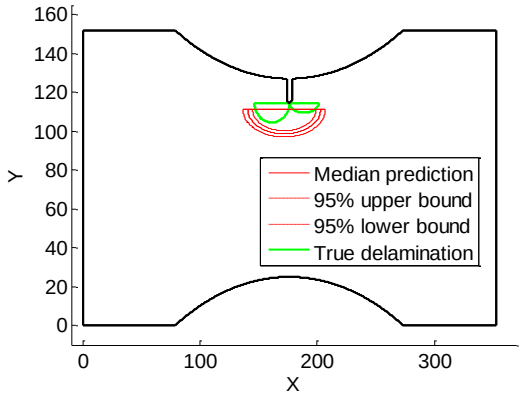

(b) Four updating iterations

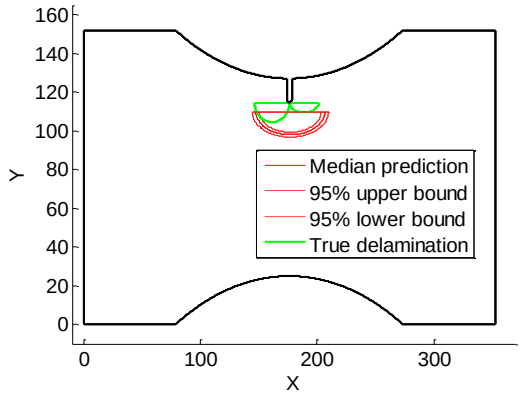

(c) Eight updating iterations

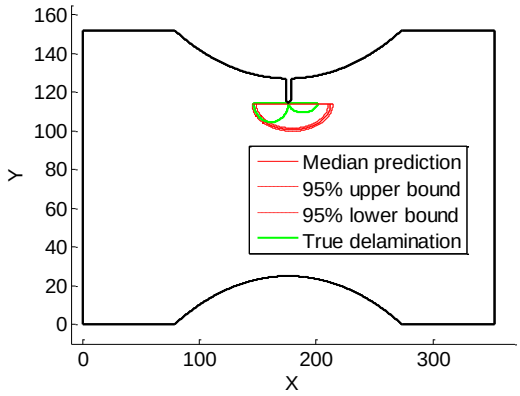

(d) Twelve updating iterations

Fig. 3.26 The Comparison between the True Value and Updated Results

As given in Fig. 3.26, the predicted delamination is reconstructed based on the location and size prediction after each updating iteration. More updating iterations mean more information is incorporated in the Bayesian updating. At the same time, the uncertainty bound is decreased as more observations are available, which is consistent with the result given in Fig. 3.23 and Fig. 3.25.

To validate the generality of this framework, the fatigue testing data for another two specimens are processed and two sensitive features are extracted. Fig. 3.27 and Fig. 3.28 show the extracted features for sample L2S20_F and L2S17_F .

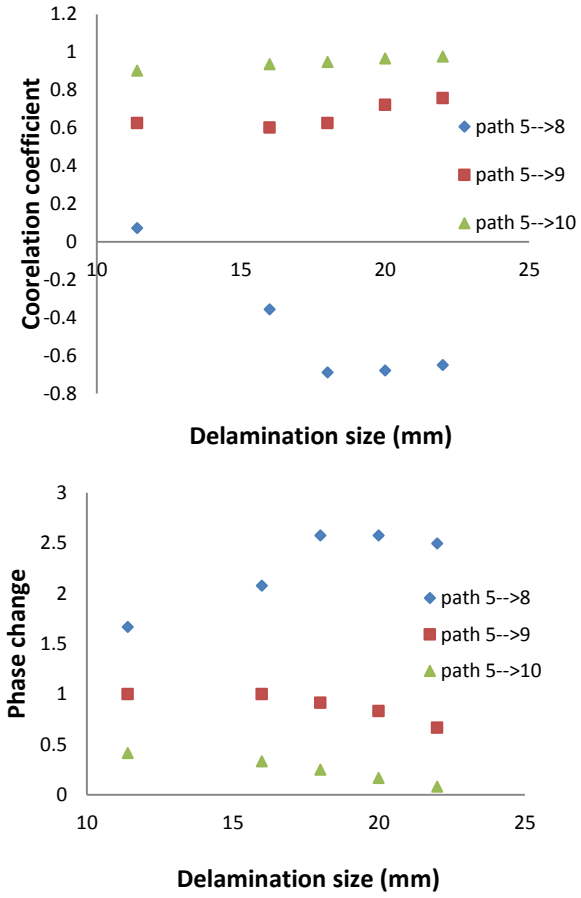

Fig. 3.27 Feature Extraction of Specimen L2S20_F

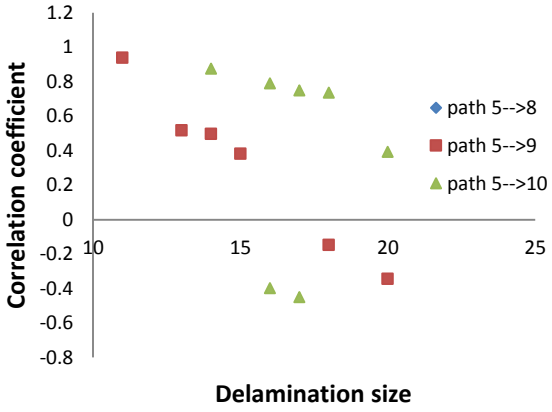

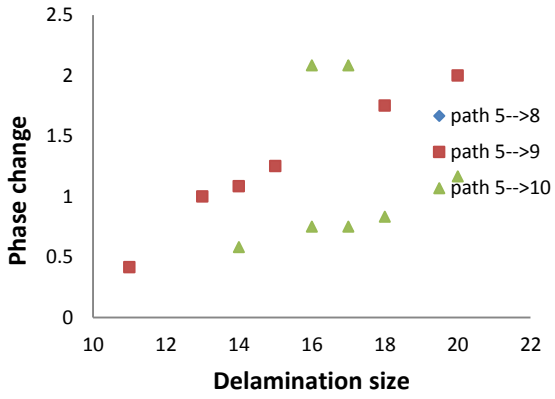

Fig. 3.28 Feature Extraction of Specimen L2S17_F

As shown in Fig. 3.27 and Fig. 3.28, the correlation coefficient and phase change features have different patterns, which represent the uncertainties associated with each specimen. Following the same procedure discussed in section 3.4.1, the fitting models can be assumed as the same form given in Eq.(3-3). It should be noted that this model shows good performance for different specimens, but the corresponding model regression coefficients β_{ij} may vary. The final location and delamination size updating results are given in Fig. 3.29 and Fig. 3.30 for L2S20_F specimen. Similarly, Fig. 3.31shows the final delamination prediction for specimen L2S17_F.

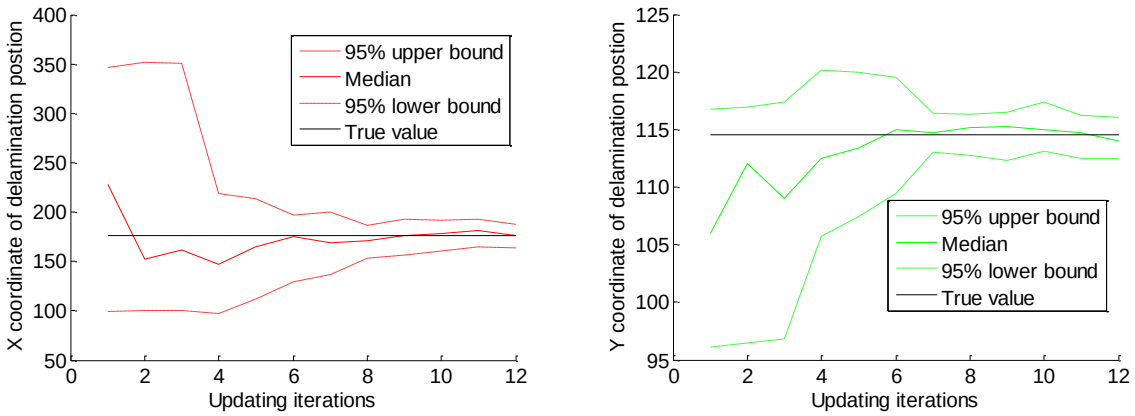

Fig. 3.29 The Delamination Location Updating for L2S20_F

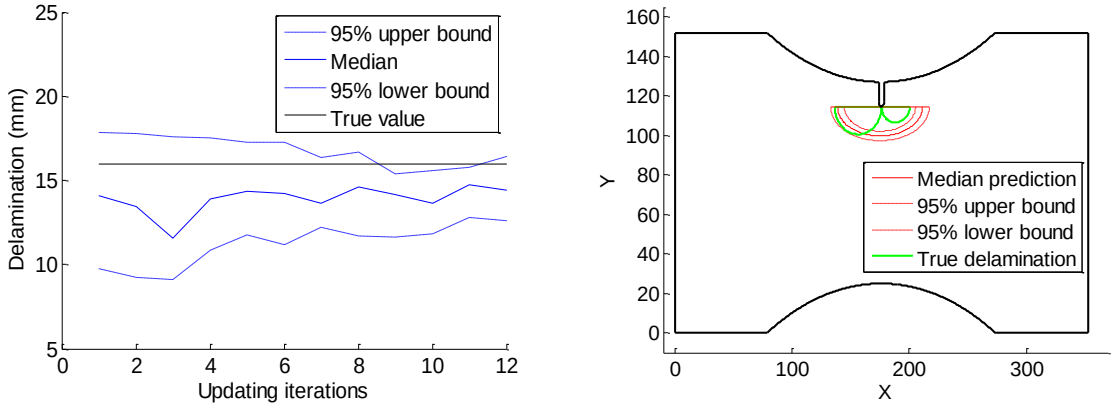

Fig. 3.30 The Delamination Size and Final Delamination Prediction for L2S20_F

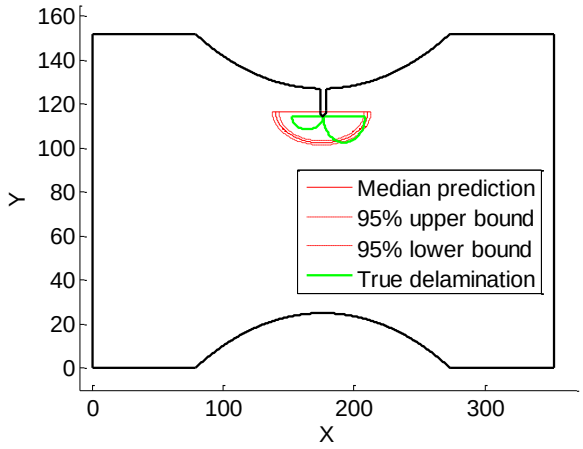

Fig. 3.31 The Final Delamination Prediction for Specimen L2S17_F

3.5 Remaining Useful Life (RUL) Prognosis of Composite Materials

In this section, a general framework for composites RUL prediction using stiffness degradation is discussed. The main focus is on stiffness degradation model development and Lamb wave-based overall material stiffness diagnosis.

3.5.1 Stiffness Degradation Model Development

In this section, a general model for composites stiffness degradation is proposed. The key idea is to express the overall composite stiffness reduction at certain loading cycles using a growth rate kinetics. The stiffness degradation rate is assumed to be a function of the applied stress amplitude and the current stiffness. Detailed the discussion is given below.

Under fatigue loadings, different forms of damage such as matrix cracking, delamination and fiber breaking will occur simultaneously or sequentially, which will eventually lead to the final failure of the entire composite component. The concept of the stiffness degradation-based life prediction is to implicitly incorporate different forms of damage mechanism into different stages of stiffness degradation curve. A schematic representation of a general stiffness degradation curve for composites is shown in Fig. 3.32.

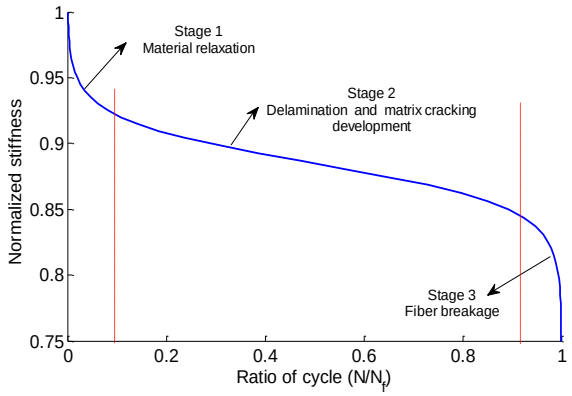

Fig. 3.32 The General Trend for Composite Stiffness Degradation

As shown in Fig. 3.32, the x-axis is the normalized fatigue life (i.e., normalized with respect to the final failure life) and the y-axis is the normalized stiffness (i.e., normalized with the stiffness before the fatigue loading). The stiffness degradation process can be divided into three distinct stages. Initially, the stiffness decreases quickly during the initial loading stage. In this stage, some initial defect in the material will quickly approaches to the stable stage. After that, the stiffness decreases gradually due to the development of delamination and matrix cracking. Close to the final failure state, the stiffness drops dramatically because of the fatigue loading induced fiber breakage. The last stage is usually unstable and the specimen will fail in a very short amount of cycles.

In the experimental testing shown later, the initial relaxation state will stabilize within several hundreds to a few thousands cycles which is very small portion of the entire fatigue life span of composites under high cycle fatigue conditions. Ignoring the initial relaxation stage will not produce large error for the final fatigue life prediction. Thus, the proposed study will focus on the second and third stages, which can simplify the stiffness degradation model without sacrificing life prediction accuracy. In the proposed stiffness degradation model, two major hypotheses are made. First, the stiffness degradation rate is increasing

monotonically and reaches its maximum at final failure stage. Second, for the same material, the stiffness degradation rate is assumed to be a function of the applied stress and the current stiffness. Based on the above assumptions, the generalized stiffness degradation model can be proposed as

$$\frac{ds}{dN} = -f(\Delta\sigma, s) \tag{3-4}$$

where $\Delta\sigma$ is the applied stress amplitude. s is the current normalized stiffness, which is obtained by dividing the current stiffness by value under the health condition. N is the fatigue cycles and $\frac{ds}{dN}$ is the stiffness degradation rate during one cycle. f is a generic function which describes the relationship between the stiffness degradation rate, the stress amplitude, and stiffness. In the proposed study, a power law function is used to represent the general trend for the second and third stage of the stiffness degradation curve. Thus, the proposed stiffness degradation model is expressed as

$$\frac{ds}{dN} = -C(\Delta\sigma s^{-r})^m \tag{3-5}$$

where C, r and m are model parameters which are assumed to be positive and can be calibrated using experimental datasets. Using Eq.(3-5), the predicted stiffness for given fatigue cycles can be calculated by integrating both sides as

$$\int_{s_0}^{s} s^{rm}\, ds = \int_0^N -c(\Delta\sigma)^m\ dN \tag{3-6}$$

In the fatigue life prognosis, the model proposed above is used to determine the system degradation under fatigue loading. Once the system response (e.g. stiffness) is available, the model parameter and uncertainties can be updated to achieve more accurate prediction. One method to incorporate the stiffness measurement for the life prediction updating is the Bayesian inference method, which is discussed below.

3.5.2 Fatigue Life Prognosis Using Bayesian Inference

Remaining useful life prognosis for a structural component should be continuously updated using the latest measurement information. New information should be incorporated to improve prognostics algorithm by updating model parameters, their distributions, correcting for model errors, and updating future loading conditions. Widely used Bayes' theorem [14, 89, 90] allows updating of the parameter distributions based on the condition monitoring data from the system. The detailed derivation for uncertainties integration using Bayesian inference has been provided in section 2.4.1. The difference is to replace the physics model using the stiffness degradation model proposed before. The feature integration model will be similar with the stiffness diagnosis model discussed below.

Based on above discussions, the general framework for the in-situ fatigue life prognosis framework is given below,

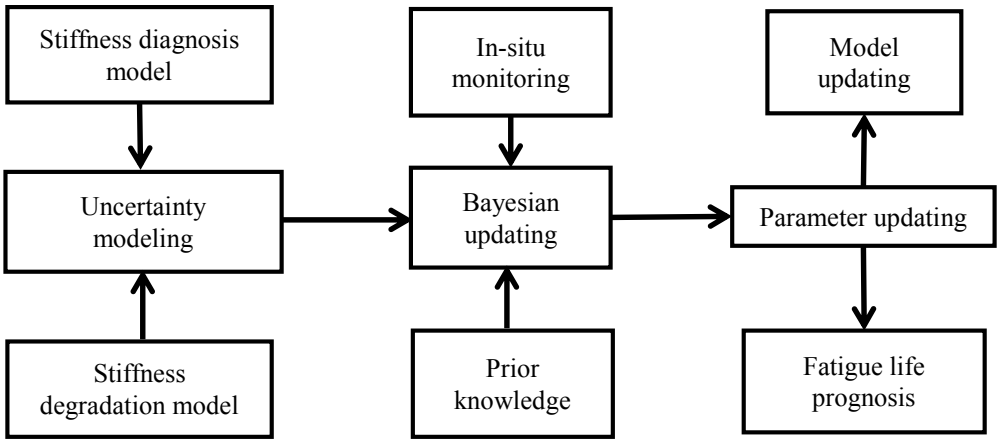

Fig. 3.33 The General Framework for In-situ Fatigue Life Prognosis

3.5.3 In-situ Stiffness Diagnosis Using Lamb Waves

In this section, the stiffness degradation model proposed in section 3.5.1 will be calibrated using laboratory composites fatigue experiment data. With embedded PZT

sensor network system, the stiffness is estimated using the extracted damage features from digital signal processing.

3.5.3.1 Experiment Setup

The test setup for stiffness diagnosis of open-hole composites includes two major systems: data acquisition system and fatigue testing system (Fig. 3.34). Data acquisition system is used to generate exciting signal to the PZT sensor network and to collect the signal received by sensors. The specimen is subject to tensile-tensile constant loading spectrum using fatigue testing system. Loads with different stress amplitude are applied for different specimens. For all fatigue tests in the current study, stress ratio is fixed to be 0.1.

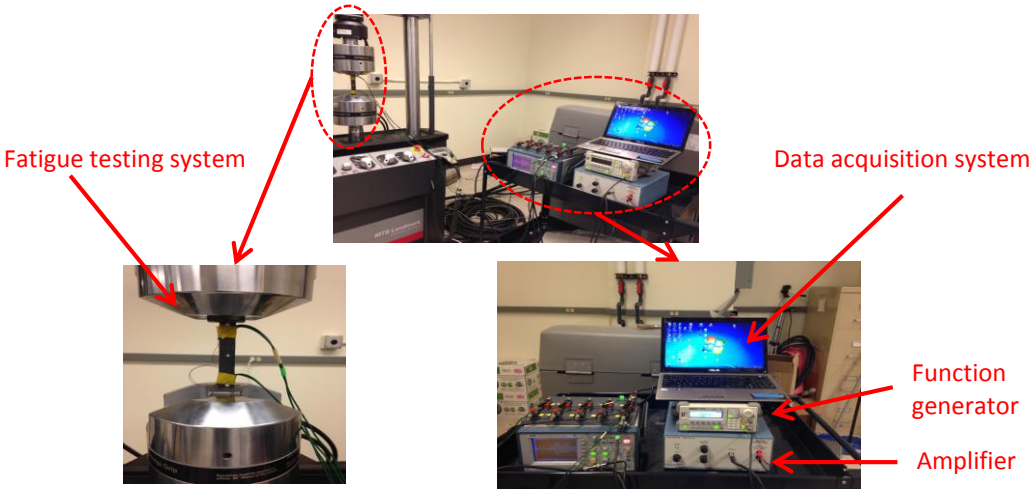

Fig. 3.34 Open-Hole Fatigue Testing Setup

The composite open-hole specimen is made of 12 plies of composite lamina with layup $[90_3/0_3]_s$. The raw material for manufacturing the composites is carbon fiber cloth, resin, hardener and other consuming materials, such as nylon membrane and cloth. The fiber is unidirectional carbon fiber, the resin is resin epoxy system FS-A23, Part(A) and the hardener is epoxy system FS-B412, Part(B). All of them are produced by Fiberglast.com.

The composite layup is conducted manually, and then applied with 160Mpa pressure under 100 Celsius. The schematic layup before the hot pressing is shown in Fig. 3.35. The specimen thickness and width varies slightly due to manufacturing variability. The nominal specimen dimension 200x20x2 mm with a center hole diameter of 5 mm. The nominal specimen geometry is schematically shown in Fig. 3.36. Actuators and sensors are mounted on both sides of the open-hole specimen to add redundancy to the measurement system. Actuator 1 and sensor 1 are mounted on the front side; actuator 2 and sensor 2 are mounted on the back side of the specimen. Each actuator and sensor pair forms a diagnosis path.

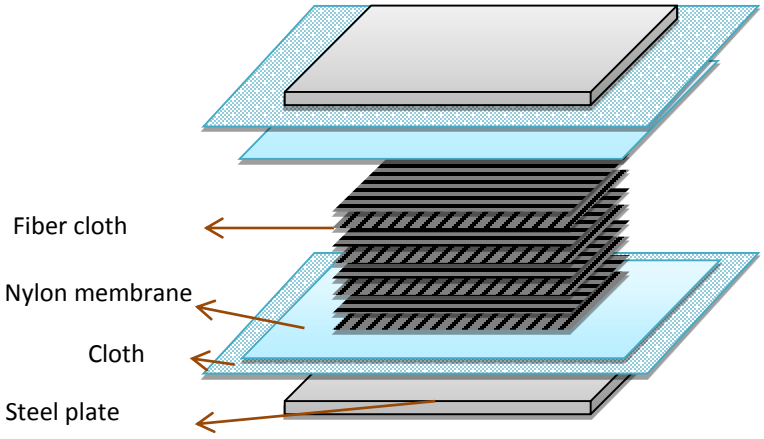

Fig. 3.35 Schematic Representation of Composite Layup

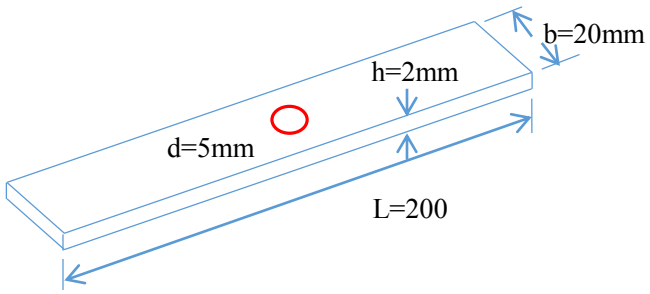

Fig. 3.36 The Nominal Geometry for the Open-Hole Specimen

3.5.3.2 Experimental Results and Diagnosis Model Development

In this study, a hamming-windowed sinusoidal tone burst with 3.5 cycles is used as the actuating signal. Central frequency of this signal is set to be 200 kHz, as shown in Fig.

3.37. Under fatigue loading, initially matrix cracking starts to appear in 90° plies, and then delamination follows and grows between 0° and 90° plies with fiber breaking at the same time. Most specimens fail near the center hole location. Some specimens fail at the other locations due to the splitting of the laminates. The final failure for the open-hole specimens is shown in Fig. 3.38.

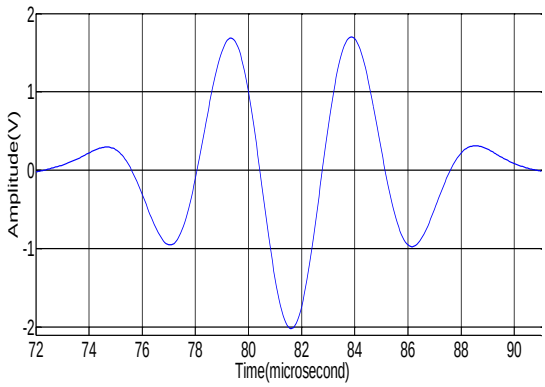

Fig. 3.37 A Tone Burst Signal of 3.5 Cycles with 200kHz Central Frequency

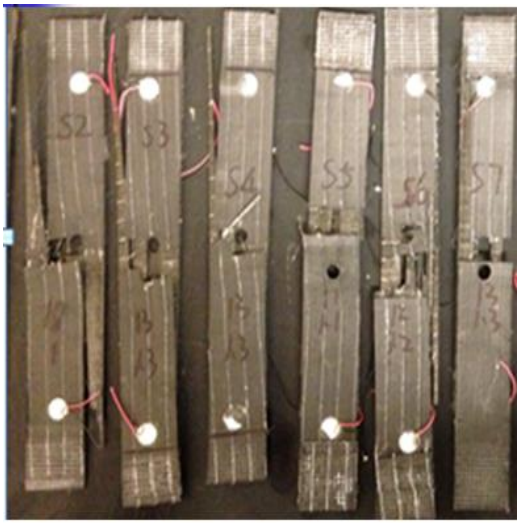

Fig. 3.38 The Final Failure Pattern for Open-Hole Specimens

After installing the specimen on the hydraulic machine, a baseline PZT signal under pristine condition is collected first. Subsequent data are collected periodically during fatigue loading cycles. Fig. 3.39 illustrates a typical signal obtained for specimen S2 with

a 13kN maximum force. Fig. 3.39 (a) is the overall raw signals collected during the testing. Fig. 3.39(b) shows the first time-window of interest between the dashed lines in Fig. 3.39(a). With further signal processing, changes in selected features, such as normalized amplitude, correlation coefficient, and cross correlation are calculated. All of these feature changes can be obtained by comparing the received signals under pristine and damaged conditions. Normalized amplitude change reflects the energy dissipation due to the damage and correlation coefficient change reflects the first time window signal perturbation due to the new waves generated at the delamination or matrix cracking [10]. Cross correlation measures the similarity between these two time series. For the cross correlation at different time lags, the maximum value is extracted and normalized w.r.t. the maximum value under pristine condition. Specimen stiffness is measured using the force-displacement curve from the hydraulic machine output. Multiple specimens are tested here to assess reproducibility of the diagnosis method and investigate the effect of variability among different specimens. A detailed experiment summary for these specimens is provided in Table 3.4. To compare with different specimens under different stress amplitude, the extracted features and specimen stiffness are normalized with respect to their maximum value under pristine conditions. Normalized stiffness vs. different sensor signal features for different specimens is shown in Fig. 3.40.

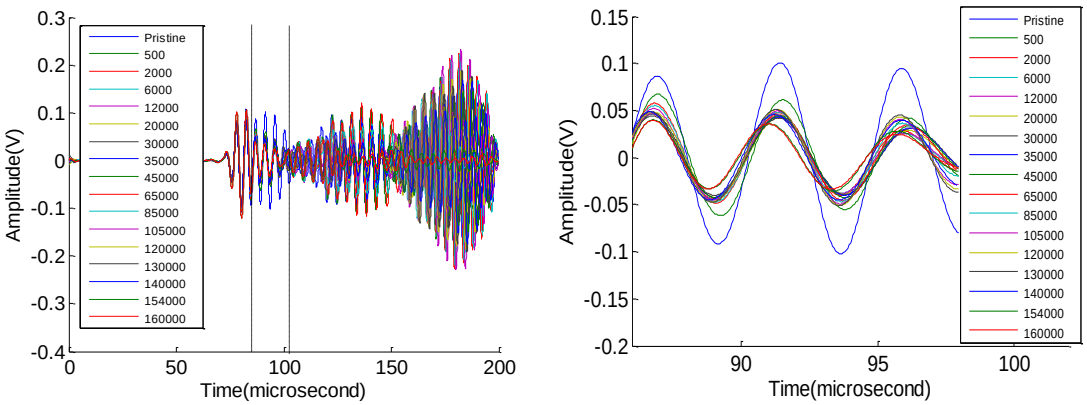

Fig. 3.39 The Received Signal for Specimen S2 at Different Cycles

Table 3.4. Testing Information Summary for Different Specimens

Specimen #	Max stress (Mpa)	Stress ratio	Fatigue life (cycles)
S1	296	0.1	423500
S2	325	0.1	163400
S3	326	0.1	85600
S4	428	0.1	10680
S5	410	0.1	45000
S6	379	0.1	41257

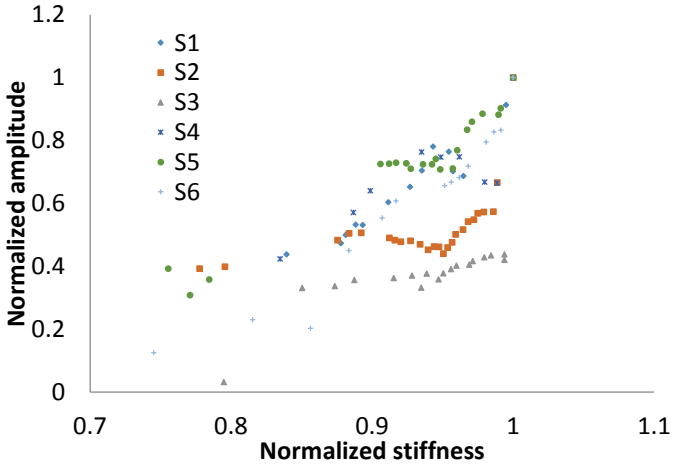

(a)

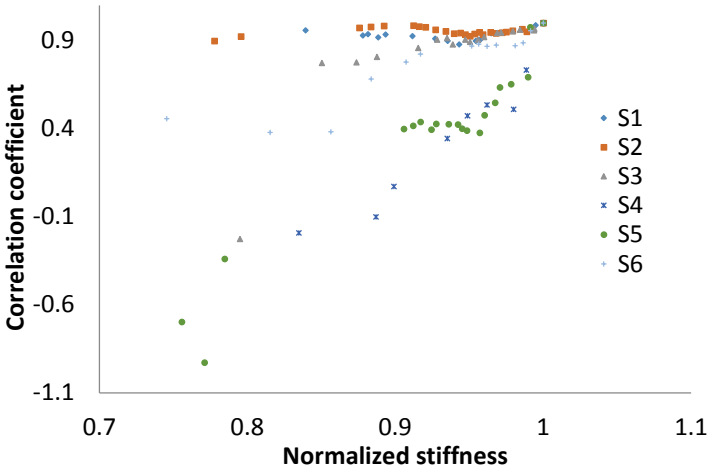

(b)

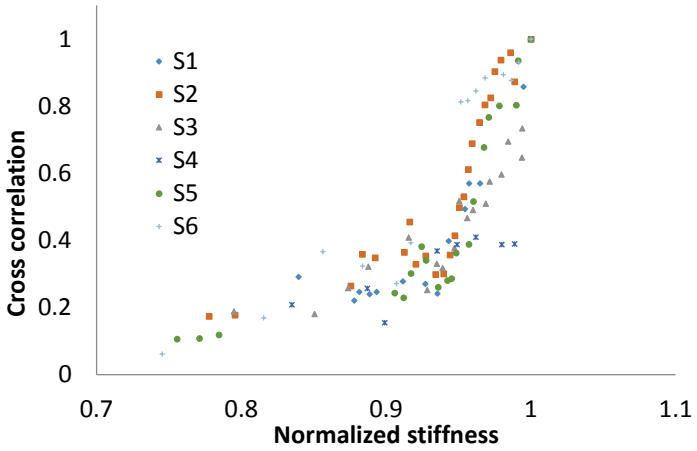

(c)

Fig. 3.40 These Three Features vs. Normalized Stiffness for Six Specimens

As seen in the above figures, large uncertainties are observed across different specimens. It is observed that these three features have generally monotonic relationship with the normalized stiffness. However, it is difficult to predict the normalized stiffness using a single feature due to large uncertainties in different specimens. Thus, all features are combined into a second order multiple variable regression model to estimate the normalized stiffness. Collected sensor data from specimens (S1, S2, S3, S4, and S5) are used as calibration to get the regression coefficients in Eq. (3-7). Values for those coefficients in Eq. (3-7) are listed in Table 3.5. Sensor data from specimen S6 is used as

validation. Fig. 3.41 shows the predicted normalized stiffness using the proposed second order regression model.

$$s = \alpha_0 + \alpha_1 x + \alpha_2 y + \alpha_3 z + \alpha_4 x^2 + \alpha_5 y^2 + \alpha_6 \sqrt{z} + \alpha_7 xy + \alpha_8 x\sqrt{z} + \alpha_9 y\sqrt{z} \quad (3\text{-}7)$$

s: normalized stiffness
x: normalized amplitude
y: correlation coefficient
z: cross correlation

Table 3.5. Coefficients for the Second Order Multivariate Regression Model

Coefficient	Value
$\boldsymbol{\alpha_0}$	0.5108
$\boldsymbol{\alpha_1}$	0.0919
$\boldsymbol{\alpha_2}$	-0.0440
$\boldsymbol{\alpha_3}$	-0.5370
$\boldsymbol{\alpha_4}$	0.2938
$\boldsymbol{\alpha_5}$	-0.0250
$\boldsymbol{\alpha_6}$	0.9516
$\boldsymbol{\alpha_7}$	-0.1060
$\boldsymbol{\alpha_8}$	-0.4040
$\boldsymbol{\alpha_9}$	0. 2675

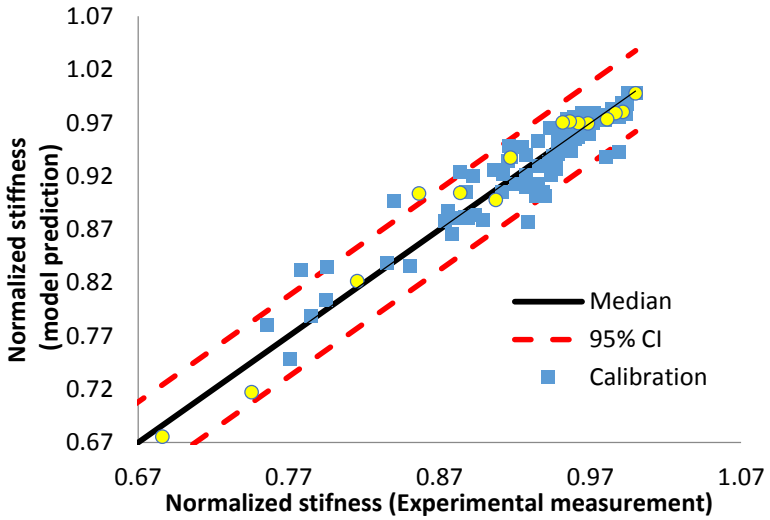

Fig. 3.41 The Predicted Normalized Stiffness vs. Experimental Measurements (R^2=0.8819)

From Fig. 3.41 above, it can be seen that the proposed model can provide reasonable prediction for the normalized stiffness. The predicted normalized stiffness for specimen S6 will be used in the following section as a demonstration example for RUL prediction.

3.5.3.3 Probability of Detection

The probability of detection (PoD) measures the detection capability of Non-destructive technique (NDT) under certain inspection conditions [91]. As discussed above, the system response (i.e. the stiffness degradation) is estimated using ultrasonic signal features. The PoD of the diagnosis model is derived and presented in detailed below. Assume ŝ is the detected normalized stiffness and s is the true system response of interest, then the PoD curve for these data can be approximated using linear relationship between $\ln(\hat{s})$ and $\ln(s)$ [91], which is expressed as,

$$ln(\hat{s}) = \beta_0 + \beta_1 ln(s) + \delta \tag{3-8}$$

where δ is an error term, which is normally distributed with zero mean and standard deviation σ_δ, β_0 and β_1 are model coefficients. In this problem, the normalized stiffness will be considered as detected if ŝ is less than the pre-specified threshold s_{th}. Therefore, the function PoD(s) can be given as,

$$PoD(s) = P(ln(\hat{s}) < ln(s_{th})) = 1 - \Phi((ln(s) - \mu)/\sigma) \tag{3-9}$$

$$\mu = (ln(s_{th}) - \beta_0)/\beta_1 \tag{3-10}$$

$$\sigma = \sigma_\delta/\beta_1 \tag{3-11}$$

where Φ is the cumulative distribution function of the standard normal distribution. Given the detected $\hat{s}$ and available true system response s, the coefficients in Eq. (3-8) can be estimated using linear regression, which is expressed as,

$$ln(\hat{s}) = -0.0096 + 0.8465\, ln(s) + \delta \tag{3-12}$$

where δ is the error term. In order to validate the distribution of δ, its histogram and normal probability paper are shown in Fig. 3.42.

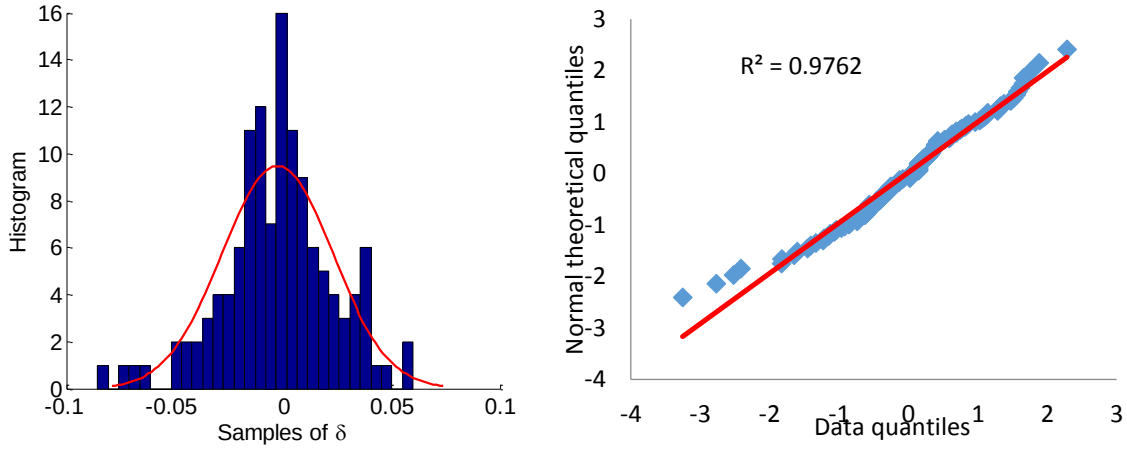

Fig. 3.42 The Histogram and Probability Plot of Term δ

From Fig. 3.42, it can be observed that the probability plot shows highly linear trend based on the linear regression statistics, which also substantiates that the error term is normally distributed. Observation from the data suggests that the normalized stiffness can be detected once it is less than 1, thus the pre-specified threshold s_{th} is set to be 1. With above information, the parameter μ and σ can be calculated as,

$$\mu = \frac{ln(s_{th}) - \beta_0}{\beta_1} = \frac{ln(1) - (-0.0096)}{0.8465} = 0.0113 \tag{3-13}$$

$$\sigma = \frac{\sigma_\delta}{\beta_1} = \frac{0.0255}{0.8465} = 0.0301 \tag{3-14}$$

Using Eq. (3-9), the PoD for different normalized stiffness is illustrated below in Fig. 3.43. It can be seen that over 90% PoD can be achieved when normalized stiffness is less than 0.97. It demonstrates the accuracy and sensitivity of the proposed detection method for stiffness degradation.

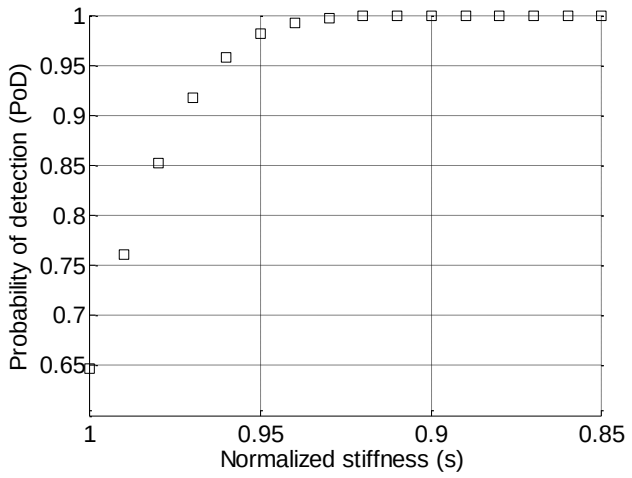

Fig. 3.43 The PoD for Different Normalized Stiffness

3.5.3.4 Stiffness Degradation Model Validation

To validate the general stiffness degradation trend shown in Fig. 3.32, measured stiffness degradation curves for all the specimens are shown in Fig. 3.44. In order to get the kinetics equation for the stiffness degradation, local time derivatives (i.e., rate) are required. To get a smooth estimation for local derivatives, 5 point local polynomial regression is used [92]. The stiffness changing rate per cycle is shown in Fig. 3.45.

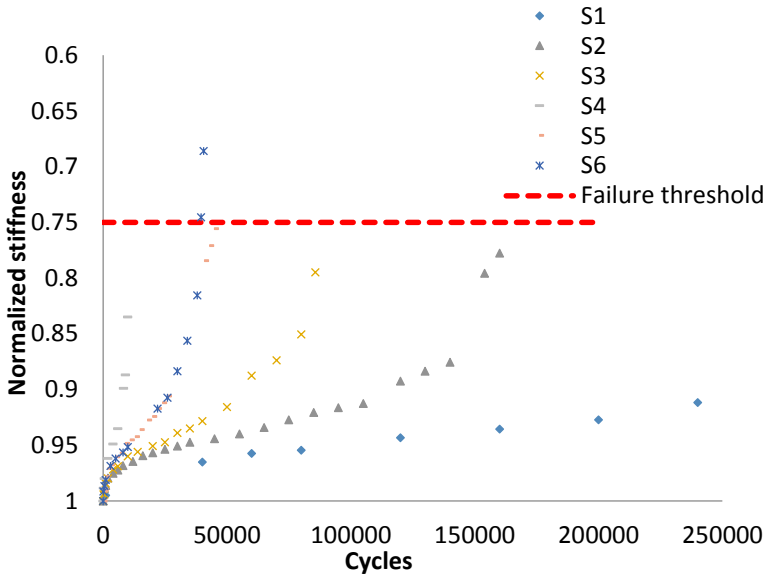

Fig. 3.44 The Stiffness Degradation Curves for All Specimens

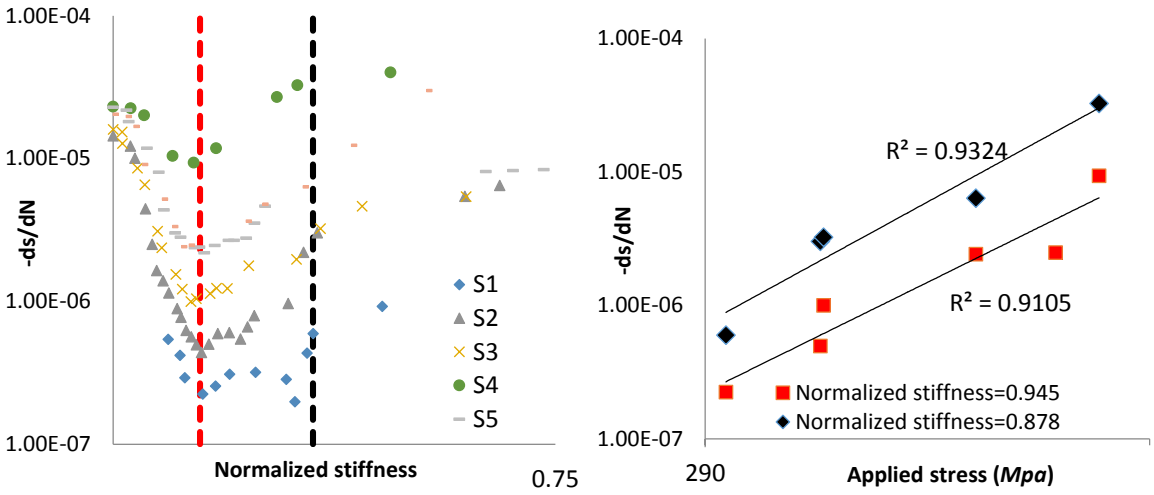

(a) (b)

Fig. 3.45 The Stiffness Degradation Rate for Different Specimens (Log-log scale). (a) w.r.t. Normalized Stiffness, (b) w.r.t. Applied Stress.

From Fig. 3.44, it can be observed that normalized stiffness decreases very fast at the initial stage and so does the stiffness degradation rate. The degradation rate reaches its minimum at the transition point from stage 1 to stage 2 shown as red dashed line in Fig. 3.45(a). During stage 2, the degradation rate is increasing gradually and reaching to its maximum at its final failure stage. Fig. 3.45 indicates that the stiffness degradation rate is log-linear with respect to the current normalized stiffness value and applied stress. The stiffness degradation rate is plotted with respect to a mixed stiffness and stress term in Fig. 3.46.

.

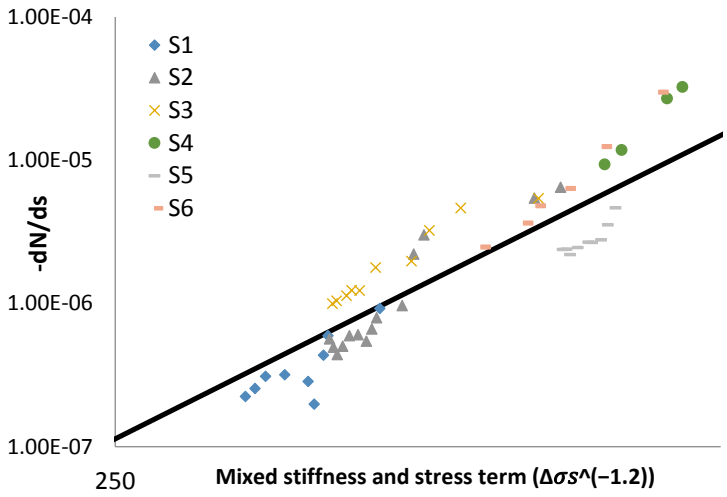

Fig. 3.46 The Stiffness Degradation Rate Considering the Applied Stress (Log-log scale)

From Fig. 3.46, all the curves coalesce and form a general linear relationship can be obtained between the stiffness degradation rate and the term of $\Delta\sigma s^{-1.2}$ in log-scale. Based on that, the proposed stiffness degradation model is calibrated as,

$$ds/dN = -C(\Delta\sigma s^{-1.2})^m \tag{3-15}$$

where N is the fatigue cycle at time t, s is the normalized stiffness, C and m are model parameters, which may vary for different specimens. These two parameters will be considered as random variables so as to capture the uncertainties between different specimens. These distributions will be updated using the proposed Bayesian inference framework. A demonstration example will be given in the following section.

3.5.4 Demonstration Examples

Following the framework shown in Fig. 3.33, the stiffness degradation model and diagnosis model proposed above are integrated using Bayesian inference for fatigue life prognosis. In the stiffness degradation shown in Eq.(3-6), the lower integration limit s_0 should be determined initially in order to obtain the predicted stiffness at N cycles. Due to ignorance of the initial stage of stiffness degradation. The parameter s_0 is approximated

with initial stage stiffness degradation data obtained from all specimens. The value is around 0.99 for all specimens. The prior distributions of parameters C and m are determined by the linear regression statistics illustrated in Table 3.6. In this study, the normalized stiffness is inferred from piezoelectric sensor signal and is estimated using the quadratic regression model given in Eq.(3-7) . The failure threshold is set to 0.75, which is consist for all specimens.

Predictions using the proposed diagnosis and prognosis framework and the experimentally measured stiffness and life are compared together in Fig. 3.47 and Fig. 3.48. In those figures, the x-axis is the fatigue cycles and the y-axis is the normalized stiffness. The measured stiffness using hydraulic machine (ground truth), the inferred stiffness from piezoelectric sensor signal (diagnosis), and the Bayesian updating results (prognosis) are shown together. Fig. 3.47 shows the predictions with prior distributions of parameters. The prior distributions for the two parameters are listed in Table 3.6. As can be seen, the prior distributions of parameters are from other testing specimen data and is very different from the investigated specimen. Thus, a large error is observed for the prediction of stiffness degradation and life (i.e., the fatigue cycles when the unstable stiffness degradation occurs). Fig. 3.48 shows the updated results from the proposed prognosis method with different numbers of observation points. Blue solid line is the median prediction using the prior distribution. Hollow rectangular points are the experimentally measured stiffness. Black solid points are the stiffness inferred from the Lamb wave-based damage detection method.

Table 3.6 The Prior Distribution of Two Model Parameters

Parameter	C	m
PDF	Log-normal	normal
Mean	-60	8.3

Standard deviation	0.2	0.1

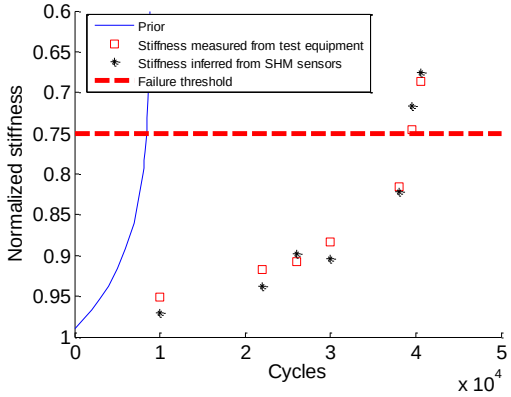

Fig. 3.47 The Prior Belief and Experimental Datasets

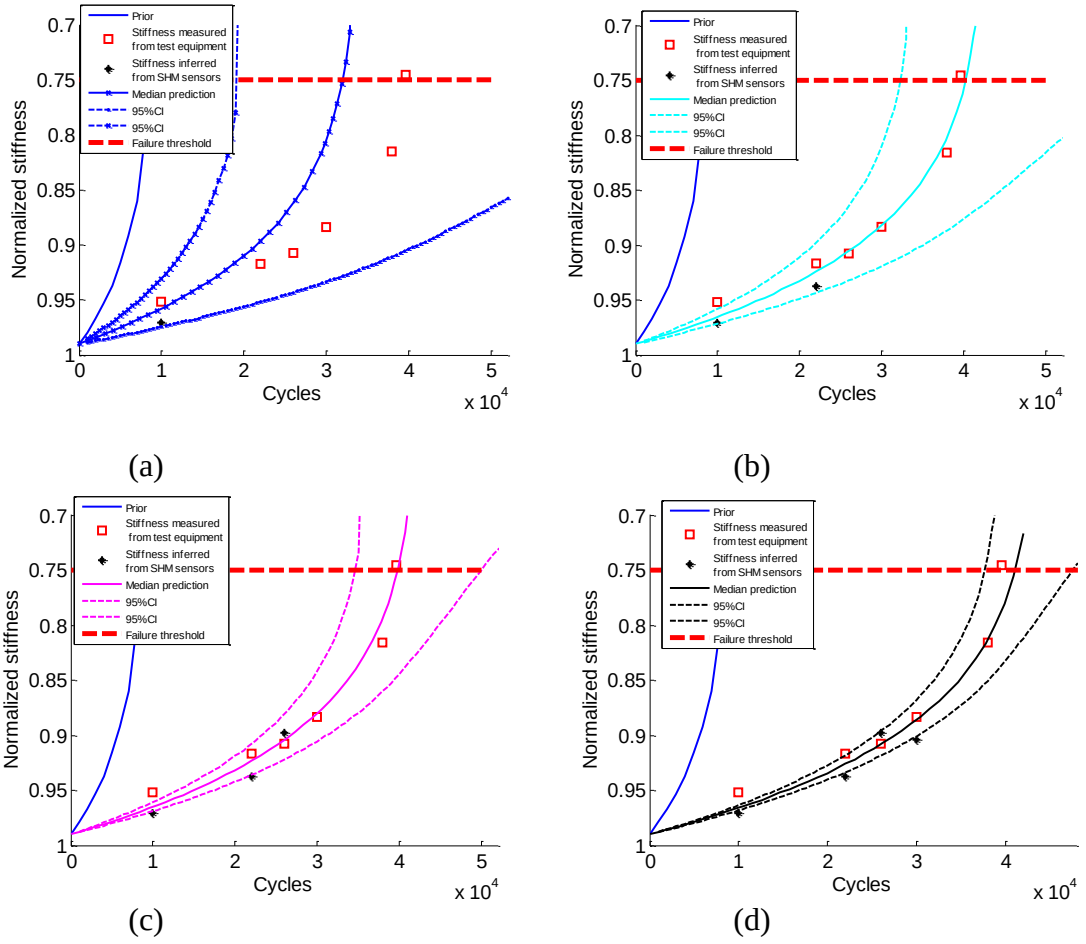

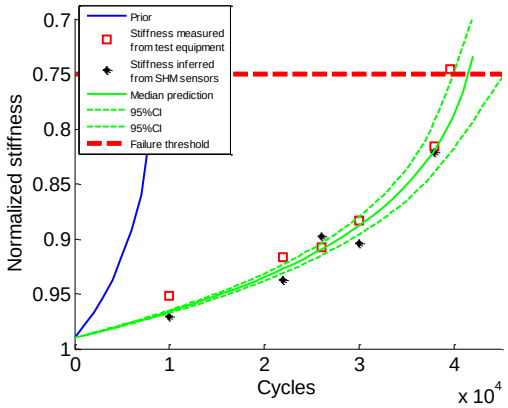

(e)

Fig. 3.48 Bayesian Updating Results. (a) Updating One, (b) Updating Two, (c) Updating Three, (d), Updating Four, and (e) Updating Five.

From Fig. 3.48, it can also be seen that the median prediction trend gets closer to the experimentally measured ground truth with additional updating using inferred stiffness data. The uncertainty bounds become narrower with additional updating, which indicates the effectiveness of the Bayesian updating method in reducing prognostic uncertainties. This trend can also be observed in the updated parameter distribution, shown in Fig. 3.49.

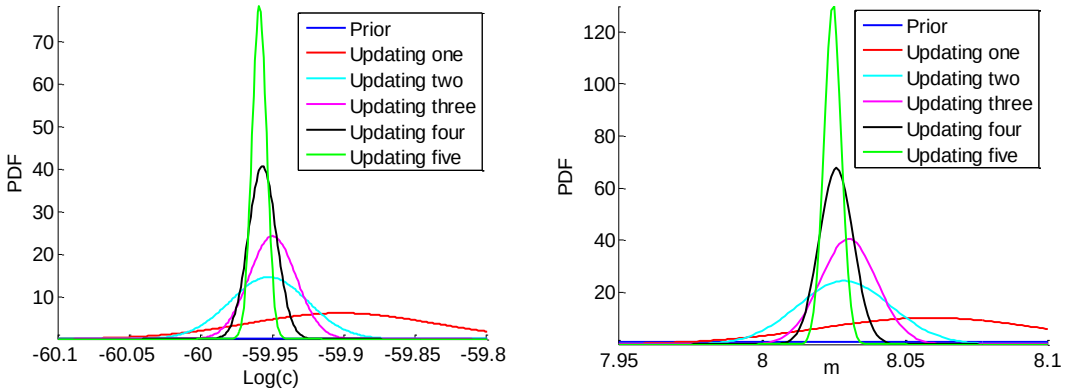

Fig. 3.49 Parameters Updating Results. (a) Updated Log(c), (b) Updated m.

To evaluate the performance of the prognostic model, prognostic metrics are employed. A detailed discussion of metrics-based model validation can be found in [46-49]. Following the similar procedure discussed in section 2.4.4. The performance is visually depicted on an RUL vs. Time plot, where accurate predictions would lie on the ground truth RUL line

(black solid line) for all times. The red dots in the plots represent predicted performance at times when the Bayesian updating was applied. Error bars represent the spread of predicted PDF for corresponding prediction. The validation of the proposed prognostic method is given in Fig. 3.50.

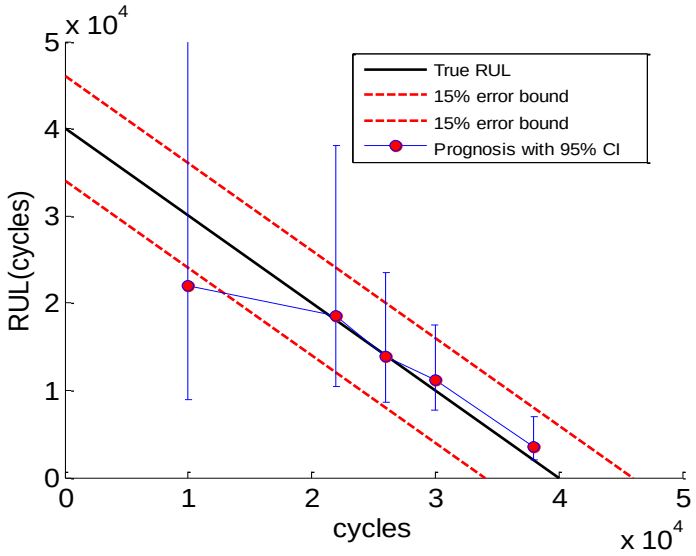

Fig. 3.50 Prognostic Performance Assessment

Fig. 3.50 shows that the excellent median prediction illustrated as pink dot is obtained after each updating. The proposed prognostic method can provide accurate median RUL prediction when prognosis horizon (PH) is about 2×10^4 cycles and the 95% RUL prediction interval enters the 15% error bound at the fourth updating.

3.6 Conclusions

In this chapter, a Lamb wave-based fatigue damage diagnosis and remaining useful life (RUL) prognosis method is proposed. Following the similar procedure discussed in section 2.5, a new probabilistic damage size and location estimation algorithm (BIM) based on in-situ measurements is proposed, which incorporates the Lamb wave-based signal features into the Bayesian updating framework. In order to improve the prognosis efficiency, the

detected overall stiffness is considered as the in-situ system response for predicting the RUL of open-hole composite specimens.

Based on numerical investigation, the delamination and matrix cracking of composite materials have significant effect on signal features. The normalized amplitude change, correlation coefficient, and phase angle change are proven to be good candidates for the damage detection in composite plates, which are compared and validated using experimental data. Additionally, the matrix cracking depth has little effect on the received wave signal, if the depth is beyond one ply thickness. On the contrary, gaps between matrix cracks (crack density), crack lengths, and delamination size have significant effect on the received signals.

From the proposed Bayesian imaging method, it can be concluded that the correlation coefficient and phase change features in the received signal varies as the damage size and location changes. The variation is very small if the sensor path is far away from the damage location. The BIM can simultaneously estimate the damage size and location information with corresponding uncertainty bounds. These uncertainty bounds tend to converge after about 6~8 updating points in the current study.

Since it is very difficult to directly incorporate the detected delamination and matrix cracking for real time fatigue life prognosis, the stiffness degradation is chosen as an alternative for system response measurement of open-hole composite specimens. From experimental testing, three stages of stiffness degradation are observed from the experimental testing results and stiffness degradation rate is shown to be dependent on the current stiffness value and applied loading. A power law stiffness degradation model is proposed to consider the stiffness degradation physics. The detected stiffness degradation

is included in the Bayesian updating for RUL prediction. Satisfactory results are achieved based on the performance assessment using prognostic metrics.

4 THE ADJOINT METHOD-BASED DAMAGE DIAGNOSIS

4.1 Introduction

From the discussion of previous chapters, the widely used Lamb wave-based damage diagnosis method is highly dependent on the baseline signal and extracted damage identification features using signal processing techniques. These properties limit its application on general detection of complex 3D damages. Therefore, in this chapter, the physics of the physical scenarios, such as heat transfer and wave propagation will be incorporated in the damage diagnosis algorithm to achieve higher accuracy and resolution.

Recently, Han et. al. proposed a sonic IR technique for delamination and fatigue crack detection in composites and metallic materials [93, 94]. In this method, a high power ultrasonic transducer is used to excite ultrasonic wave within the composites coupon, which can generate heat flux at crack-like damage areas due to friction between interfaces [95]. The sonic IR offers very unique capabilities for fast full field damage imaging and the proposed study focuses on this technique. The original development of sonic IR was for the 2D area/size estimation and the technique was extended for delamination depth profiling in [96]. The existing sonic IR method uses the surface temperature profile to estimate the damage size and cannot provide accurate delamination shape detection because the surface temperature profile blurs at the sharp delamination edges. In addition, the depth profiling in [96] is a semi-3D imaging method and use the analytical solution for isotropic homogeneous material for approximation, which might yield large errors for materials showing strong thermal anisotropy or heterogeneity.

In view of the above brief review, a new method for accurate and efficient true 3D imaging technique is developed to reconstruct the crack-like damage based on the surface measured temperature history. Inverse heat conduction (IHC) is employed to incorporate

full surface temperature history measurements and to achieve more accurate damage shape and depth detection. Inverse heat conduction was initially proposed to estimate the surface heat flux of space vehicles using the discrete temperature measurements of interior sensors[88, 97] . The objective to the IHC is to estimate the unknown initial conditions, boundary conditions or thermal properties, which minimizes the difference between the estimated and measured temperature history [98]. The majority of the existing work focus on estimating heat source waveforms [88, 99-101], which is not the case for damage detection problems because the heat source waveforms are determined by the ultrasonic transducer and is known beforehand. Thus, the damage detection excited by ultrasonic transducer should be considered as heat source location detection problem.

Additionally, damage in materials will cause thermal properties, such as density, specific heat, or thermal conductivity change, which can highly impact the physics of heat conduction. The temperature-dependent thermal conductivity estimation has been investigated using the general framework of IHC [102, 103]. However, the thermal conductivity is space-dependent for damage detection problems because its value for some elements may be reduced due to certain types of damages. After discretization, the thermal conductivity values for all elements are considered as unknown parameters, whose dimensions are much greater than that of the temperature-dependent thermal conductivity estimation problems. Space-dependent thermal conductivity estimation for general 3D objects was rarely investigated.

Similarly, mechanical properties, such as modulus and density change can affect the physics of elastic wave propagation. Therefore, the damage detection problem can be transferred to modulus detection for wave propagation problems. The shear/Young's

modulus can be estimated following the similar procedure of space-dependent thermal conductivity by just substituting the governing equations. Sensitivity of the objective function with respect to the shear modulus can be efficiently computed using the adjoint method, which has been implemented to compute the sensitivity for seismic problems [104, 105], in which a single element with perturbed density is assumed and detected with very low frequency excitation. The application of the adjoint method is extended to ultrasonic wave-based multiple damage detection with arbitrary shapes and at random locations. The effect of certain conditions, such as the number of measurement sensors, measurement duration, and level of measurement noise will be investigated.

This chapter is organized as follows. First, the IHC formulation for detecting 3D crack-like defects is derived by considering the heat source generated by the ultrasonic transducer. The adjoint method is used to enhance the computational efficiency for large scale simulation. Following this, the derivation for thermal conductivity estimation is given and two thermal conductivity detection problems (i.e. 1D and 3D) are provided to demonstrate the overall procedure. Some parametric studies are conducted in this part. After that, the shear modulus estimation for wave propagation problems is discussed. Several 2D examples are used to illustrate the efficacy of this proposed method. Parametric studies are performed to investigate the effect of the number of measurement sensors as well as the measurement noise. Finally, some conclusions and future work are generated based on the current investigation.

4.2 Crack-Like Damage Diagnosis Using Inverse Heat Conduction (IHC)

In this section, a general crack-like damage diagnosis framework is introduced. A formula is proposed to link the ultrasonic transducer with the heat source term of heat

transfer problems. Its corresponding adjoint problem is derived to compute the derivative of the objective function with respect to the unknown parameters. Examples for metallic and composite materials are used to demonstrate the feasibility of the proposed method.

4.2.1 3D Crack-Like Damage Reconstruction Based on IHC

The general formulation and derivation of inverse heat conduction problem and its solution method are provided. Our key contribution is to propose a new formulation which makes the 3D crack-like damage detection problem solvable using the inverse heat conduction.

From the sonic IR setup discussed in [96], several hypothesis are made for the proposed study: 1) heat flux is generated between crack/delaminated interfaces after ultrasonic excitation; 2) the waveform of the generated heat flux is proportional to the ultrasonic excitation waveform; 3) full-field temperature history for each node on the surface can be measured by infrared camera. A brief derivation of IHC based on above hypothesis will be provided below. The detailed discussion on IHC and corresponding solution techniques can be found in [88].

4.2.1.1 IHC Formulation

Based on the above discussion, the unknown internal heat source is parameterized as the weighted sum of the heat source at each node and the temperatures history for each node on the surface is available. Thus, the one dimensional IHC corresponding to the crack-like damage detection problem can be formulated by minimizing the objective function given as

$$F(W) = \sum_{m=1}^{M} \sum_{j=1}^{J} \left[Y_m(x_m, t_j) - T_m(x_m, t_j) \right]^2$$

$$= \iint_{x,t} \big(Y(x,t) - T(x,t)\big)^2 \delta(x - x_m) dt dx \tag{4-1}$$

where $F(W)$ is the sum of the square error for temperature measurements. $Y_m\big(x_m, t_j\big)$ is the available temperature history measurement at surface node x_m, time t_j. $T_m\big(x_m, t_j\big)$ is the estimated temperature history measurement at surface node x_m, time t_j. W is the vector for the weight at each node $W = [w_1 \quad w_2 \quad \dots w_I]^T$, where I is the total number of possible heat source locations. M is the total number of measurement points. J is the total number of time points.

The estimated temperature $T_m\big(x_m, t_j\big)$ can be obtained by solving the direct heat conduction problem given as

$$\rho c \frac{\partial T(x,t)}{\partial t} = \lambda \frac{\partial T^2(x,t)}{\partial x^2} + g(x,t;W) \tag{4-2}$$

where ρ is mass density, c is specific heat, and λ is thermal conductivity. The initial temperature is the same with the surrounding environment and the top and bottom surfaces are applied with free convection boundary condition. Without loss of generality, the environment temperature is set to be a reference temperature zero. Thus, the boundary and initial conditions are given as

$$\lambda \frac{\partial T(x,t)}{\partial x} = hT(x,t) \text{ for } x = 0 \tag{4-3}$$

$$\lambda \frac{\partial T(x,t)}{\partial x} = -hT(x,t) \text{ for } x = L \tag{4-4}$$

$$T(x,0) = 0 \tag{4-5}$$

where h is the free convection coefficient.

4.2.1.2 Gradient Calculation Using the Adjoint Problem

In order to minimize the least square problem in Eq. (4-1), the key step is to compute

the function gradient with respect to unknown parameters. Since each node in the domain is assigned with a weight, there will be a large number of unknown parameters for realistic applications. In classical IHC analysis, the derivative with respect to each unknown parameter is computed using finite difference methods, which is not feasible for high dimensional problems. The adjoint method is able to compute the derivative for all parameters using one direct heat conduction simulation, which can significantly enhance the computational efficiency. The formulation for gradient calculation using adjoint method is shown below.

The sensitivity problem is defined as the perturbation of $T_m(x_m, t_j)$ as a result of the perturbation of unknown heat source parameters, which is defined as

$$\rho c \frac{\partial \Delta T(x,t)}{\partial t} = \lambda \frac{\partial \Delta T^2(x,t)}{\partial x^2} + \Delta g(x,t;W) \tag{4-6}$$

$$\lambda \frac{\partial \Delta T(x,t)}{\partial x} = h\Delta T(x,t) \text{ for } x = 0 \tag{4-7}$$

$$\lambda \frac{\partial \Delta T(x,t)}{\partial x} = -h\Delta T(x,t) \text{ for } x = L \tag{4-8}$$

Given the perturbation of the heat source term, the sensitivity problem can be solved using the direct heat conduction solver. Following the procedures discussed in [88, 101], the adjoint problem is formulated by introducing a generalized Lagrange multiplier $\varphi(x,t)$ to incorporate the heat conduction PDE constraint, which is given as

$$F(W) = \int_{t=0}^{t_f} \int_{x=0}^{L} \big(Y(x,t) - T(x,t)\big)^2 \delta(x - x_m) dx dt + \int_{t=0}^{t_f} \int_{x=0}^{L} \varphi(x,t)(\lambda \frac{\partial T^2(x,t)}{\partial x^2} + g(x,t;W) - \rho c \frac{\partial T(x,t)}{\partial t}) dx dt \tag{4-9}$$

$$\text{for } m = 1, \dots, M$$

Thus, the variation of the objective function is derived as

$$\Delta F(W) = \nabla F(W)^T \Delta W =$$

$$\int_{t=0}^{t_f} \int_{x=0}^{L} 2\big(T(x,t) - Y(x,t)\big)\delta(x - x_m)\Delta T(x,t)dxdt +$$

$$\int_{t=0}^{t_f} \int_{x=0}^{L} \varphi(x,t)\left(\lambda \frac{\partial \Delta T^2(x,t)}{\partial x^2} + \Delta g(x,t;W) - \rho c \frac{\partial \Delta T(x,t)}{\partial t}\right) dxdt \qquad (4\text{-}10)$$

$$\text{for } m = 1, \dots, M$$

Integrating by part and applying boundary conditions from the sensitivity problem yields

$$\Delta F(W) = \nabla F(W)^T \Delta W =$$

$$\int_{t=0}^{t_f} \lambda\left(-h\varphi(L,t) - \frac{\partial \varphi(L,t)}{\partial x}\right)\Delta T(L,t) - \lambda\left(h\varphi(0,t) - \frac{\partial \varphi(0,t)}{\partial x}\right)\Delta T(0,t)\, dt \; -$$

$$\int_{x=0}^{L} \rho c \varphi\big(x, t_f\big)\Delta T\big(x, t_f\big)\, dx + \int_{t=0}^{t_f} \int_{x=0}^{L} \varphi(x,t)\Delta g(x,t;W)dxdt + \qquad (4\text{-}11)$$

$$\int_{t=0}^{t_f} \int_{x=0}^{L} \Delta T(x,t)\left(\lambda \frac{\partial \varphi^2(x,t)}{\partial x^2} + \rho c \frac{\partial \varphi(x,t)}{\partial t} + 2\big(T(x,t) - Y(x,t)\big)\delta(x - x_m)\right) dxdt$$

$$\text{for } m = 1, \dots, M$$

The adjoint problem is obtained by eliminating the term $\Delta \boldsymbol{T}(\boldsymbol{x}, \boldsymbol{t})$ and it is expressed as

$$\lambda \frac{\partial \varphi^2(x,t)}{\partial x^2} + \rho c \frac{\partial \varphi(x,t)}{\partial t} + 2\big(T(x,t) - Y(x,t)\big)\delta(x - x_m) = 0 \qquad (4\text{-}12)$$

$$\lambda \frac{\partial \varphi(x,t)}{\partial x} = h\varphi(x,t) \text{ for x} = 0 \qquad (4\text{-}13)$$

$$\lambda \frac{\partial \varphi(x,t)}{\partial x} = -h\varphi(x,t) \text{ for x} = \text{L} \qquad (4\text{-}14)$$

$$\varphi\big(x, t_f\big) = 0 \qquad (4\text{-}15)$$

The above adjoint problem is not the standard form of the heat conduction problem, as the final time condition instead of the initial condition is specified. Using the change of variable $\tau = t_f - t$, the above equations can be transformed into the standard form of direct heat conduction problem, which can be solved by any thermal analysis solver. After introducing the adjoint problem, the Eq.(4-11) is simplified as

$$\Delta F(W) = \nabla F(W)^T \Delta W = \int_{t=0}^{t_f} \int_{x=0}^{L} \varphi(x,t) \Delta g(x,t;W) dxdt \qquad (4\text{-}16)$$

In order to get the explicit expression for gradient term $\Delta F(W)$, the heat source is defined as

$$g(x,t;W) = \sum_{i=1}^{J} w_i f(t) \delta(x - x_i) \qquad (4\text{-}17)$$

where $f(t)$ is the given heat source waveform, x_i is the possible heat source location (i.e., nodes). Substituting Eq.(4-17) into Eq.(4-16), the gradient can be expressed as

$$\begin{aligned} \Delta F(W) = \nabla F(W)^T \Delta W &= \int_{t=0}^{t_f} \int_{x=0}^{L} \varphi(x,t) \Delta g(x,t;W) dxdt \\ &= \int_{t=0}^{t_f} \int_{x=0}^{L} \varphi(x,t) \sum_{i=1}^{I} \Delta w_i f(t) \delta(x - x_i)\, dxdt \\ &= \sum_{i=1}^{I} \int_{t=0}^{t_f} \int_{x=0}^{L} \Delta w_i f(t) \delta(x - x_i) \varphi(x,t) dxdt \\ &= \sum_{i=1}^{I} \int_{t=0}^{t_f} f(t) \varphi(x_i,t) dt\, \Delta w_i \end{aligned} \qquad (4\text{-}18)$$

Thus, the component of the derivative is written as

$$[\nabla F(W)]_i = \int_{t=0}^{t_f} f(t) \varphi(x_i,t) dt \qquad (4\text{-}19)$$

Using Eq.(4-19), the gradient with respect to each parameter w_i can be directly computed after solving the adjoint problem. In the next section, the method for applying nonnegative or bound constraints and the flowchart of conjugate gradient method coupling with the adjoint problem will be presented as the numerical algorithm for the IHC solution.

4.2.2 Conjugate Gradient Method with Bound Constraints

In [88], a conjugate gradient with adjoint problem has been discussed in detail for estimating heat source function with the known source location. This algorithm is different from the one investigated here since the heat source function can take both positive and negative values. In the 3D crack-like damage imaging problem, there is no heat sink induced by the ultrasonic transducer, thus the weight for each possible heat source is

nonnegative. In addition, the proposed method used a normalized weight factor for each possible heat source and the normalized weight at each node is not greater than 1. Thus, the optimization of the proposed IHC is a bounded inverse problem and a constraint should be applied on each parameter. Generally speaking, constrained least square problems are much slower than the unconstrained problems because they usually include nested loops in order to identify the active sets or free variables [106-109]. An intuitive approach which sets the parameter to be zero when it is outside the bound is applied in our problem. Although this method may cause inaccuracy or divergence issues [106], it proves to be very efficient and can converge to the true solution by some modifications. This method will be discussed in detail below.

4.2.2.1 Algorithm Description and Modification

In conjugate gradient method, two critical steps are: computing the direction of descent $d^k$and step size β^k. As illustrated in [88], the equations for computing these two quantities are expressed as

$$d^k = \nabla F(W^k) + \gamma^k d^{k-1} \tag{4-20}$$

where $\gamma^k = \frac{\nabla F(W^k)^T (\nabla F(W^k) - \nabla F(W^{k-1}))}{\nabla F(W^{k-1})^T \nabla F(W^{k-1})}$

$$\beta^k = \frac{\sum_{m=1}^{M} \int_{t=0}^{t_f} (T(x_m,t) - Y(x_m,t)) \Delta T(x_m,t) dt}{\sum_{m=1}^{M} \int_{t=0}^{t_f} [\Delta T(x_m,t)]^2 dt} \tag{4-21}$$

To show the procedures, let's define $S^k = \{s: w_s^k < 0 \text{ or } w_s^k > 1\}$ and set $W^k(S^k) = 0$. In order to ensure convergence of the method, the equations for updating γ^k, d^k and W^k are revised as

$$\gamma^k = \frac{\nabla \check{F}(W^k)^T (\nabla \check{F}(W^k) - \nabla \check{F}(W^{k-1}))}{\nabla \check{F}(W^{k-1})^T \nabla \check{F}(W^{k-1})} \tag{4-22}$$

where $\nabla\check{F}(W^k)$ is the partition of $\nabla F(W^k)$with index $\check{s} \notin S^k$.

$$d^k(s) = 0 \; for \; s \in S^k \text{ and } d^k(\check{s}) = \nabla F(W^k)(\check{s}) + \gamma^k d^{k-1}(\check{s}) \text{ for } \check{s} \notin S^k \quad (4\text{-}23)$$

$$W^{k+1} = W^k - \beta^k d^k \text{and } W^{k+1}(S^{k+1}) = 0 \quad (4\text{-}24)$$

Clearly, the above modification will increase the speed for algorithm convergence, because more and more parameters are set to be inactive (i.e., 0) during the optimization. Another important issue is to choose the stopping criteria, which is determined such that the temperature difference at each time point is less than1×10^{-4} ˚C. Similar with that shown in [88], the flowchart for the revised conjugate gradient method is shown in Fig. 4.1.

4.2.2.2 A numerical Exampe for Illustration

In order to illustrate the proposed methodology, a simple 1D problem is used to demonstrate the entire heat source location detection procedures. A rod with material properties and dimension listed in Table 4.1 is selected as an example. The material properties are chosen to represent a composite coupon along thickness direction. There is an internal heat source at the middle of the rod (i.e., $x = 0.9mm$) with waveform given in Fig. 4.2(a). Two free ends and lateral surface of the rod are applied with free convection and insulation boundary conditions, respectively. The direct heat conduction is formulated and solved using the finite element method documented in [110]. As mentioned in section 4.2.1.1 , the environment temperature is set to be $T_\infty = 0$ ˚C to facilitate the computation. The schematic representation of the rod is shown in Fig. 4.3.The temperature history at the right end is collected for about 14 seconds, which is used for the heat source location estimation (shown in Fig. 4.2(b)).

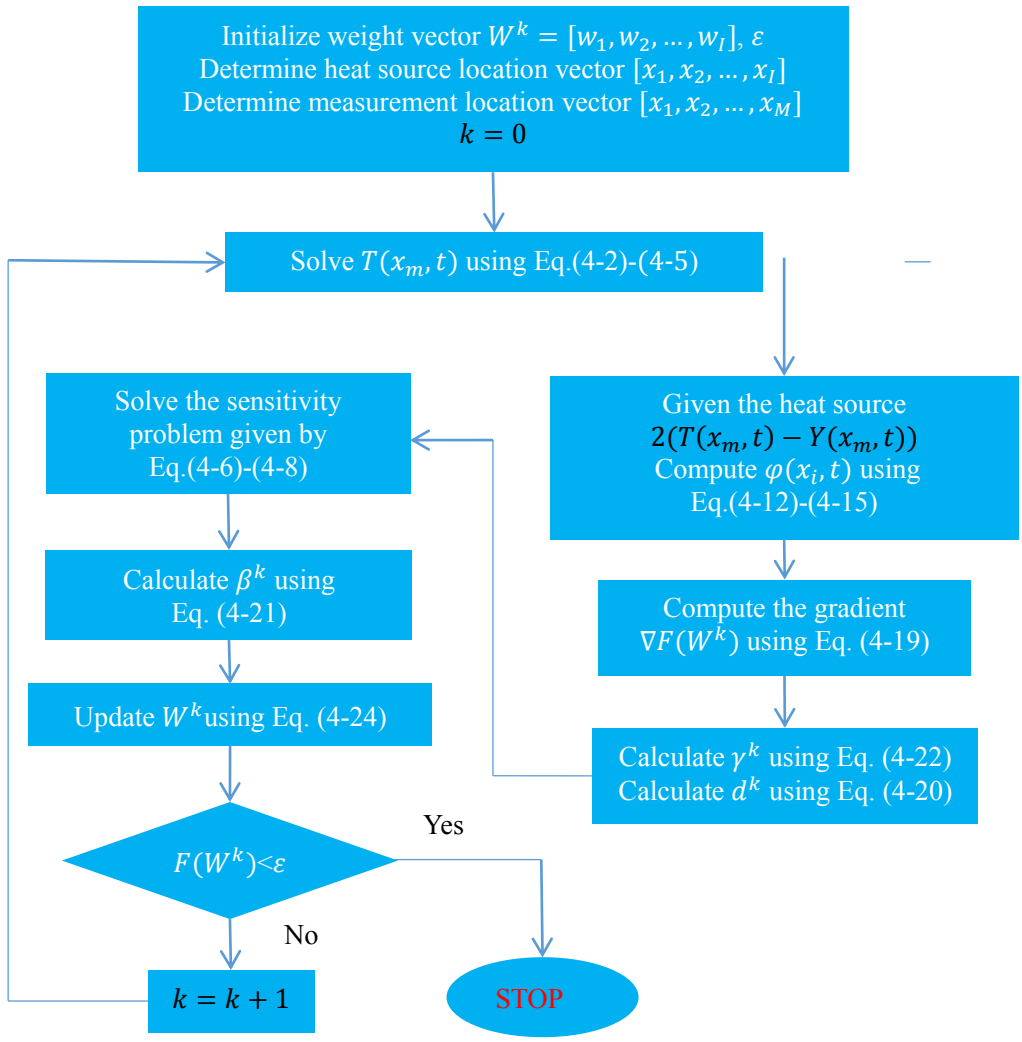

Fig. 4.1 The Flowchart for the Conjugate Gradient Method with the Adjoint Problem

Table 4.1. The Thermal Properties and Dimension of the Rod

Length (mm)	Area (mm^2)	Density (kg/m^3)	Specific heat $(J/kg\ ^\circ C)$	Thermal conductivity $(Watt/\ ^\circ C)$	Free convection coefficient $(Watt/m^2\ ^\circ C)$
1.8	0.01	2000	950	0.6	30

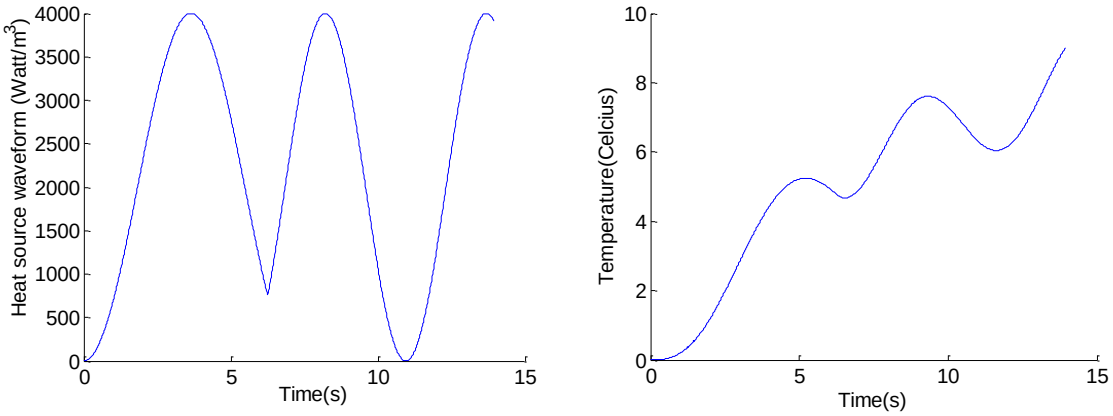

(a) (b)

Fig. 4.2 The Waveform of the Internal Heat Source (a) and Temperature History at the Right End (b)

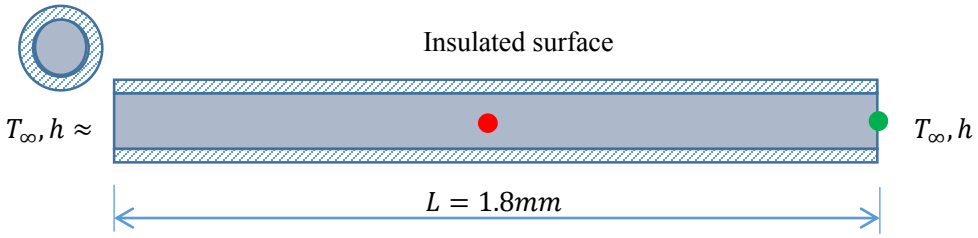

Fig. 4.3 The Schematic Representation of the Rod

The rod is divided into 10 elements (11 nodes). Given the heat source waveform, the true heat source location is determined by the position with weight *1*. Since the temperature at the right end is available, the heat source location can be estimated following the flowchart given Fig. 4.1. Initialized with uniform weights at all locations, the updated weight at each location after every 25 iterations is plotted in Fig. 4.4. The evaluation of the objective function is shown in Fig. 4.5.

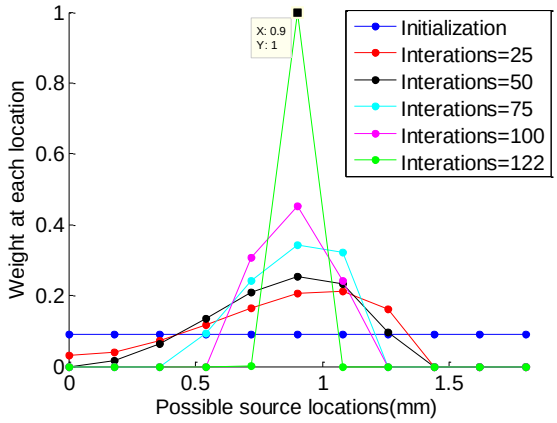

Fig. 4.4 The Estimated Weights at Possible Heat Source Locations

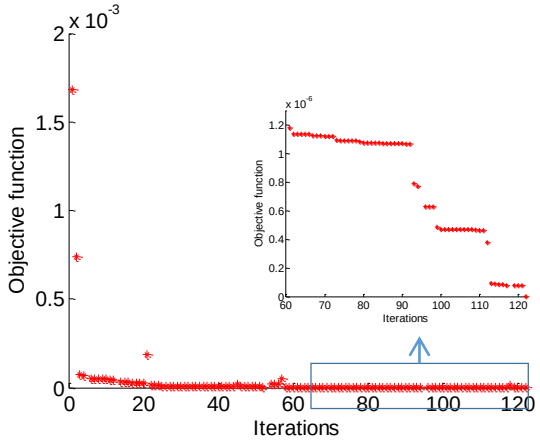

Fig. 4.5 The Evaluation of the Objective Function at Each Iteration

From Fig. 4.5, it can be observed that the objective function is monotonically decreasing during the optimization, except for a couple of points which is caused by applying the bound constraint. At the last iteration, the estimated weight(s) at $x = 0.9$ is 1 and other locations are 0 (see Fig. 4.4), which means that the detected heat source location is at the original setup location. Generally, the weight at each node can be considered as the probability of heat source existing at that particular location. An estimation procedure for the mean location of the heating source can be formulated by treating all node weights as a discrete probability distribution. If the mean value is used for estimating the true heat

source location, the estimated heat source can be expressed as

$$x_{estimated} = \bar{x} = \int xp(x)dx = \sum_{i=1}^{I} x_i\, p_i \tag{4-25}$$

where $\boldsymbol{x_i}$ is the node coordinate, $\boldsymbol{p_i}$ is the probability at that node, $\overline{x}$ is the mean source location. Clearly, this formula is applicable to the optimization results shown in Fig. 4.4. This estimation is also applicable when the heat source is not on the discretization node and an example is shown below.

Assume that the heat source is at $x = 0.555 \times 1.8mm$, which will not fall on any node if the rod is discretized less than 200 elements. Thus, there will be multiple nodes with nonzero weights (probabilities). Fig. 4.6 shows the optimized probability at each node for different number of possible heat source locations on the rod.

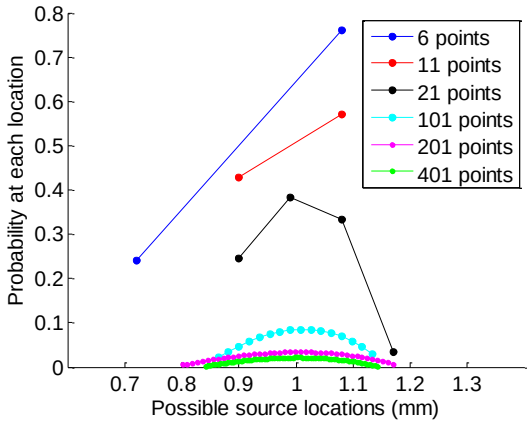

Fig. 4.6 Optimized Probability for Different Number of Possible Heat Source Locations

As seen in Fig. 4.6, there will be more nodes with nonzero probabilities if more possible heat sources are assumed along the rod. With Eq. (4-25), the mean estimation can be obtained and compared with the true value, shown in Fig. 4.7.

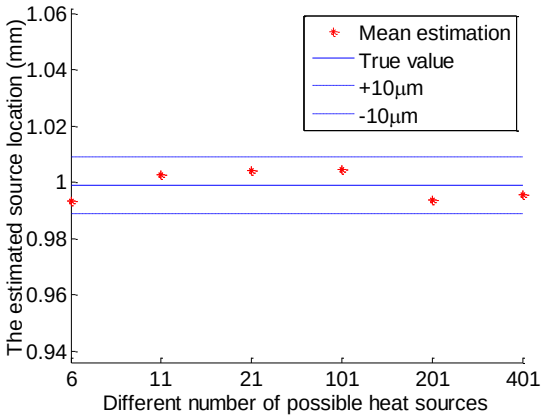

Fig. 4.7 The Comparison between Mean Prediction and the True Value

From Fig. 4.7, it can be concluded that the mean value is a good metric to achieve very accurate heat source location prediction when the true heat source is not on the grid node. Fig. 4.7 also indicates that the proposed methodology is robust with respect to the number of discretization used in the reconstruction. Thus, fewer number of elements are required if the probability distribution of the nodal weights is used for the imaging reconstruction.

4.2.3 3D Crack-Like Damage Imaging

In this section, the developed inverse heat conduction framework is applied for crack-like damage detection for both isotropic homogeneous and anisotropic heterogeneous materials for three dimensional problems. To improve the detection accuracy for 3D problems, measurements on the top and bottom surfaces are both assumed to be available. The detailed discussion is provided below.

4.2.3.1 Fish-Eye Crack Detection in High Strength Steel

In this example, a fish-eye crack is inserted in the middle of a stainless steel A304 cubic with dimension 40mm x 40mm x 40mm (illustrated in Fig. 4.8). The thermal properties of the stainless steel are listed in Table 4.2. The heat source waveform is identical with that shown in Fig. 4.2(a). All six surfaces are applied with free convection boundary conditions.

As stated before, the ultrasonic transducer can generate heat flux in the crack/delaminated areas and the crack is simulated using areas with concentrated heat flux at each node. The direct and adjoint problems of the heat conduction are solved using the commercial finite element (FE) software ABAQUS. The temperature histories at each node on the top and bottom surfaces are collected. Twenty elements are generated along each dimension. Since it takes relatively longer for the heat propagating to the surface, the simulation is run for about 28 seconds. The spatial and temporal temperature profiles from FE simulation are plotted in Fig. 4.9. The red nodes on Fig. 4.9(a) are numbered as 1-5 from the edge to the center. In the IHC framework, all internal nodes are considered as possible heat source locations and assigned with weights. The task of IHC is to estimate the weight using the available temperature history measurements on both surfaces. After optimization, weights for all nodes are plotted using OVITO 3D visualization software [111]. The final reconstructed damage imaging is illustrated in Fig. 4.10. The color bar included in Fig. 4.10 indicates the identified weight (probability) and is applicable to all the contour images in this paper. By comparing the damage imaging with ground truth, it is shown that the proposed methodology can identify the damage accurately.

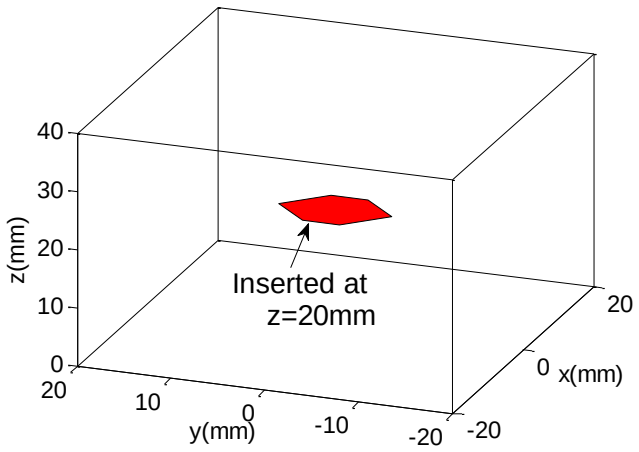

Fig. 4.8 The Fish-Eye Crack Inserted in a Stainless Steel Cubic

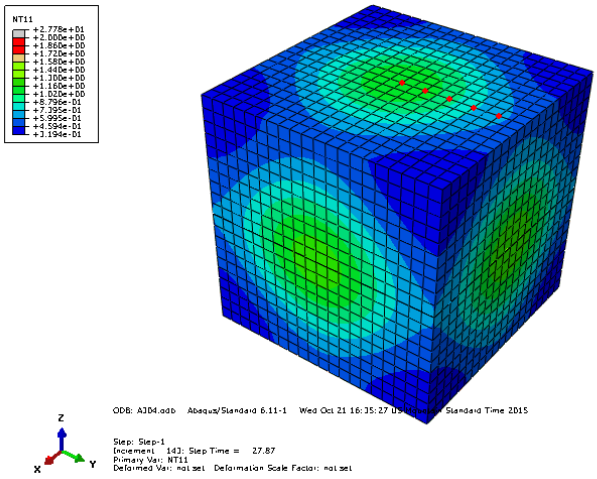

(a)

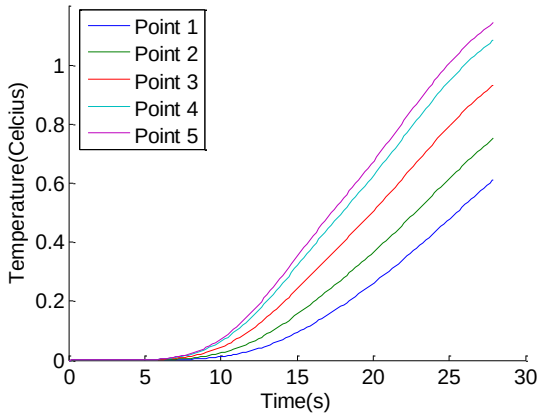

(b)

Fig. 4.9 The Spatial (a) and Temporal (b) Temperature Profiles from FE Simulation

Table 4.2. The Thermal Properties of the Stainless Steel

Density (kg/m^3)	Specific heat (J/kgC°)	Thermal conductivity ($Watt/C^\circ$)	Free convection coefficient ($Watt/m^2C^\circ$)
8000	500	16.2	30

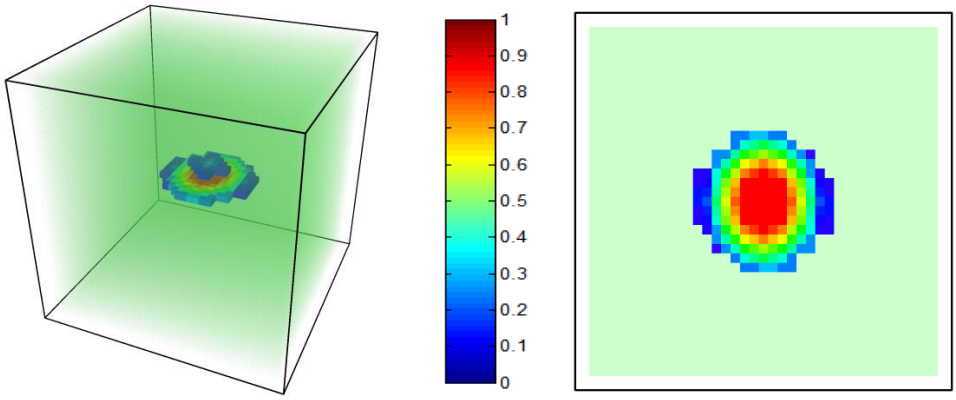

Fig. 4.10 Reconstructed Crack Damage Imaging and the Middle Slice

4.2.3.2 Delamination Detection in Carbon Fiber-Reinforced Composites

In this example, the composite coupon is made of 12 plies of composite lamina with layups $[90_2/+45_2/-45_2]$s and dimension 120mm x 120mm x 1.8mm. The thermal properties of the carbon fiber composites are listed in Table 4.3. The heat source waveform is identical with that shown in Fig. 4.2(a). The top and bottom surfaces of the composite coupon is applied with free convection boundary conditions. The other surfaces are fixed with constant reference temperature. Delamination with different shapes and areas are inserted at different interfaces (illustrated in Fig. 4.11). Analogous to section 4.2.3.1, all internal nodes are assumed to be possible heat source locations. After optimization, the estimated weights at each interface are shown in Fig. 4.12. On each picture, the number means the location of the interface where the delamination is inserted. For example, 1&2 means the interface is between the 1st and 2nd plies.

Table 4.3. The Thermal Properties of the Composite Coupon

Density (kg/m^3)	Specific heat (J/kg °C)	Transverse thermal conductivity	Longitudinal thermal conductivity ($Watt/$ °C)	Free convection coefficient
2200	950	0.6	6	30

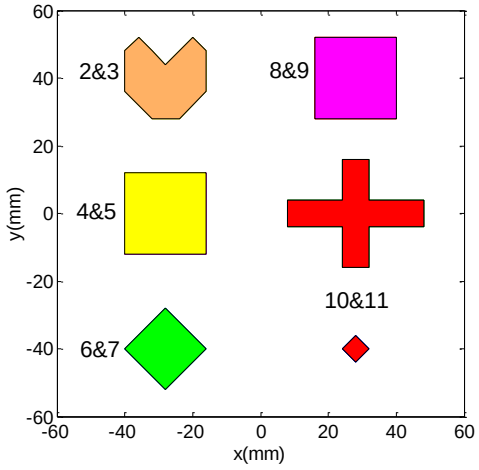

Fig. 4.11 The Area and Location of the Inserted Delamination

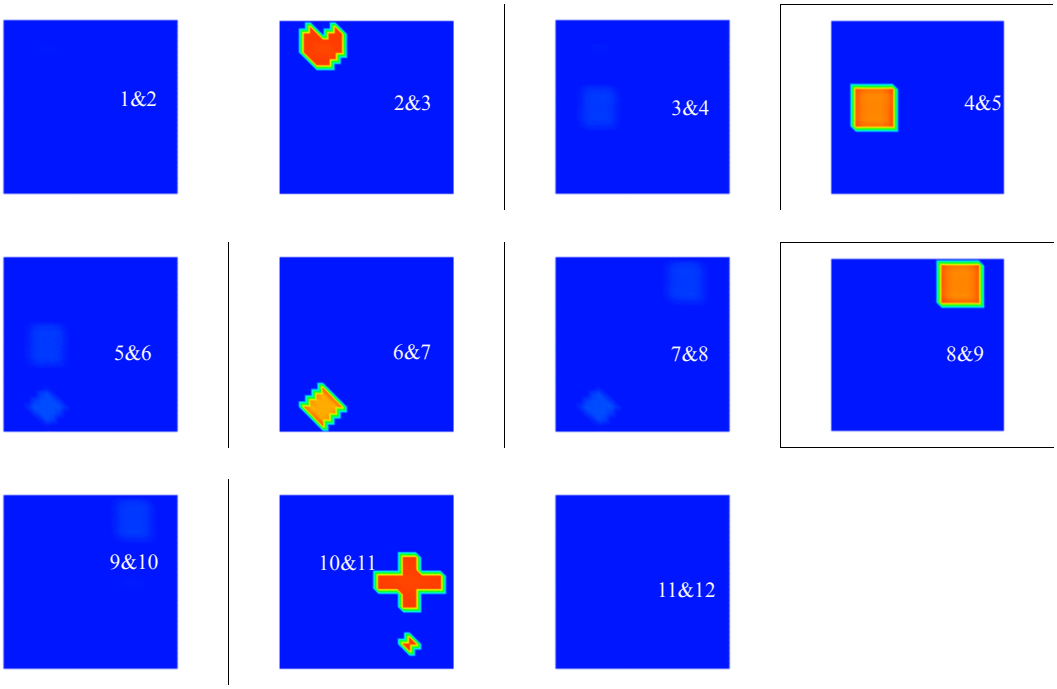

Fig. 4.12 The Estimated Weights at Each Interface

From Fig. 4.12, it can be observed that the delaminated areas can be clearly identified. Along the thickness direction, the corresponding interface that each delamination exists is also clearly and accurately detected.

4.2.3.3 Measurement Noise Effect on Damage Detection

In this section, the effect of measurement noise on the final detection performance is investigated. The collected temperature measurements are added with Gaussian random noise. The amplitude of the noise is varied and the corresponding delamination detection performance is compared. Assume the composite coupon layup is identical with section 4.2.3.2, but the dimension is reduced to 40mm x 40mm x 1.8mm. Only one delamination is inserted between the 6th and 7th plies (illustrated in Fig. 4.13). With different level of measurement noise, the weights for three adjacent interfaces are shown in Fig. 4.14. As demonstrated in Fig. 4.6, the weight at each node can be generally considered as probability. Therefore, the mean prediction can be computed using Eq.(4-25). The standard deviation for a discrete probability distribution can be expresses as

$$\boldsymbol{\sigma = \sqrt{\sum_i^n (x_i - \bar{x})^2 p_i}} \tag{4-26}$$

To measure the uncertainty, the mean and confidence bound prediction of delamination depth are demonstrated in Fig. 4.15.

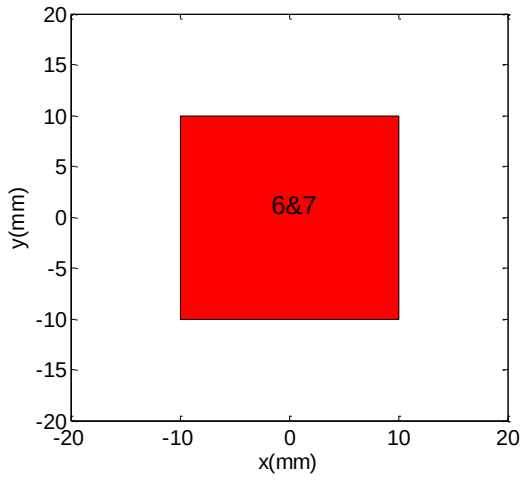

Fig. 4.13 The Area of the Inserted Delamination

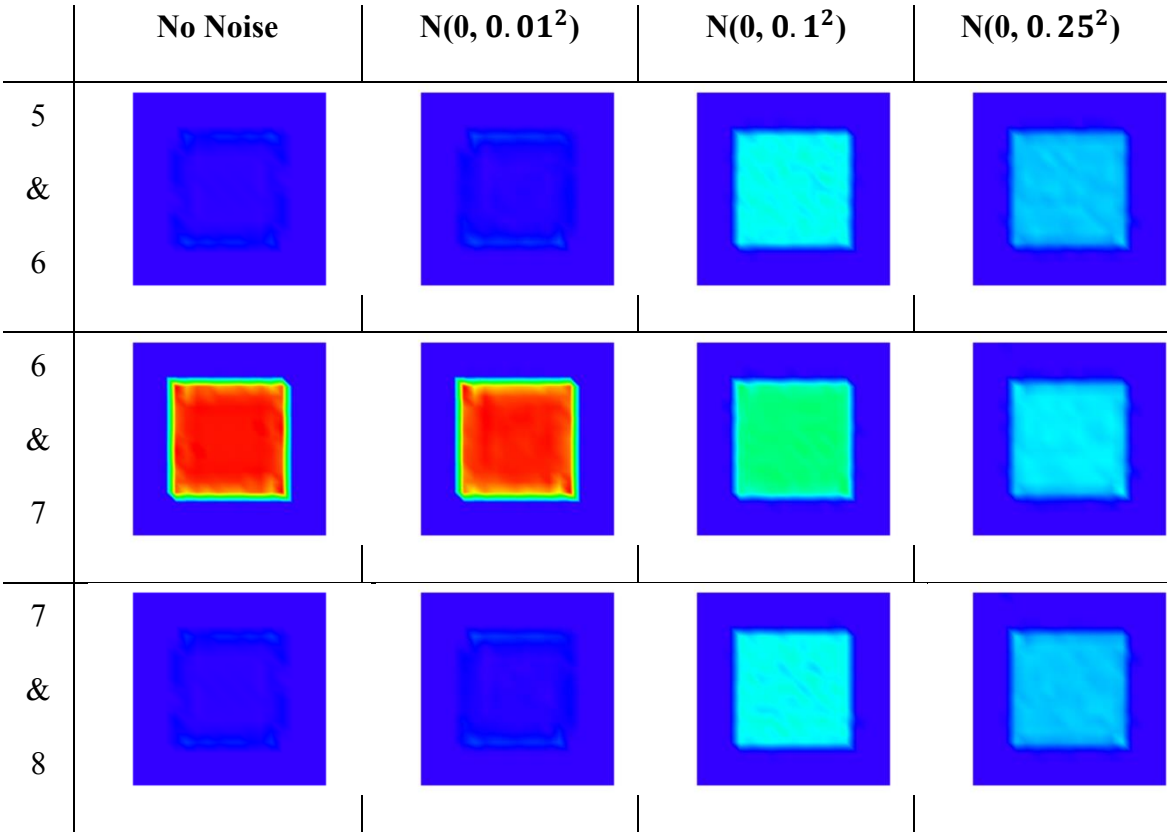

Fig. 4.14 The Delaminated Area Detection for Different Levels of Noise

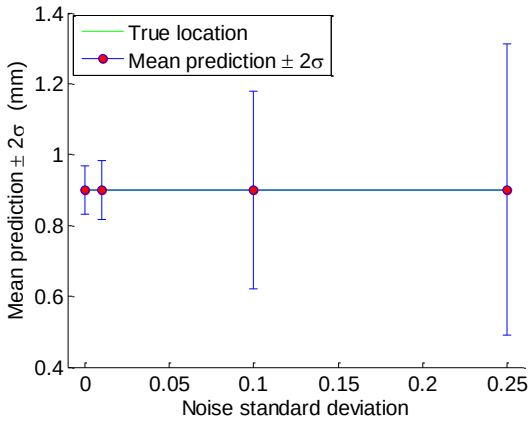

Fig. 4.15 The Mean and $\pm 2\sigma$ Prediction of Delamination Depth

As seen from Fig. 4.14, the delamination area detection is not highly affected by different level of noise. Fig. 4.15 shows that the mean location for the delamination does

not varies much with respect to different level of noises, but the confidence bounds will increase as the noise level increases.

4.3 Thermal Conductivity Diagnosis Using IHC

As discussed above, the damage detection using sonic IR technique is considered as heat source estimation for IHC problems. Additionally, damage in materials may also cause the degradation of thermal conductivity. Using appropriate formulation, some damage detection problems can be converted to thermal properties, such as thermal conductivity, density, heat capacity diagnosis if surface temperature history measurements are available. The general optimization method for IHC has be derived and discussed in [98], in which the derivation is based on the original heat conduction governing equation. To make it easier to understand, the optimization procedure is derived here using the generalized finite element equation for heat conduction problems. The idea for computing the objective function gradient will be clearly and explicitly demonstrated.

4.3.1 Problem Formulation for Thermal conductivity Diagnosis

The finite element method has been extensively used for solving physics problems governed by partial differential equations[112, 113]. As documented in [110], the heat conduction problem can be generally formulated as

$$M\dot{T}(t,\Lambda) + K(\Lambda)T(t,\Lambda) - f(t) = 0 \tag{4-27}$$

$$\lambda\frac{\partial T}{\partial x} = hT \text{ at region } \Gamma_1 \tag{4-28}$$

$$\lambda\frac{\partial T}{\partial x} = hT \text{ at region } \Gamma_2 \tag{4-29}$$

$$T(t) = 0 \text{ at } t = 0 \tag{4-30}$$

where Λ is the vector consisting of the thermal conductivity of each element, T is the vector for nodal temperature, M is the capacitance matrix, which is dependent on density and heat

capacity, $K(\Lambda)$ is the conductivity matrix, $\dot{T}$ is the time derivation of nodal temperature vector and $f(t)$ is the time dependent heat source. Taking the variation of on both sides of above equations, the sensitivity problem can be derived as

$$M\Delta\dot{T}(t,\Lambda) + K(\Lambda)\Delta T(t,\Lambda) + \Delta K(\Lambda)T(t,\Lambda) = 0 \tag{4-31}$$

$$\lambda\frac{\partial\Delta T}{\partial x} = h(\Delta T - \frac{\Delta\lambda}{\lambda}T) \text{ at region } \Gamma_1 \tag{4-32}$$

$$\lambda\frac{\partial\Delta T}{\partial x} = h(\Delta T - \frac{\Delta\lambda}{\lambda}T) \text{ at region } \Gamma_2 \tag{4-33}$$

$$\Delta T(t) = 0 \text{ at } t = 0 \tag{4-34}$$

Different from the heat source estimation problem, conductivity matrix is dependent on unknown thermal conductivity of each element and its variation will generate the equivalent heat source, which should be considered when computing the temperature variation $\Delta T(t,\Lambda)$. Additionally, the free convection boundary condition is dependent on the temperature from the direct heat conduction problem. Given the IHC problem shown in Eq.(4-1), the objective function with the direct heat conduction constraint can be expressed as

$$F(\Lambda) = \int_{t=0}^{t_f}\left(\check{I}T(t,\Lambda) - Y(t)\right)^T\left(\check{I}T(t,\Lambda) - Y(t)\right)dt +$$

$$\int_{t=0}^{t_f}\varphi^T(M\dot{T}(t,\Lambda) + K(\Lambda)T(t,\Lambda) - f(t))\,dt = 0 \tag{4-35}$$

$\check{I}$ is diagonal matrix specifying measurement nodes and φ is the nodal temperature solution for the adjoint problem. Taking the variation of Eq.(4-35) and continuously applying integration by parts, the adjoint problem can be obtained by canceling the temperature variation term$\Delta T(t,\Lambda)$.

$$M\dot{\varphi} + K(\Lambda)\varphi + 2\left(\check{I}T(t,\Lambda) - Y(t)\right) = 0 \tag{4-36}$$

$$\lambda \frac{\partial \varphi}{\partial x} = h\varphi \text{ at region } \Gamma_1 \tag{4-37}$$

$$\lambda \frac{\partial \varphi}{\partial x} = h\varphi \text{ at region } \Gamma_2 \tag{4-38}$$

$$\varphi(t) = 0 \text{ at } t = t_f \tag{4-39}$$

Similarly, using the change of variable $\tau = t_f - t$, the adjoint problem is solved intuitively as the direct heat conduction problem. Therefore, the gradient of the objective function with respect to the conductive vector can be given as

$$\frac{\partial F(\Lambda)}{\partial \Lambda} = \int_{t=0}^{t_f} \varphi^T \frac{\partial K(\Lambda)}{\partial \Lambda} T dt \tag{4-40}$$

which can be easily computed after solving the direct and adjoint heat conduction problem. The derivative of the conductivity matrix is a three dimensional matrix, which can be obtained following the similar procedure discussed in [114].

With the information of function gradient, conjugate gradient method is used to update the unknown parameters iteratively. Based on the properties of a particular problem, certain constraints on parameters can be applied to increase the speed of algorithm convergence. The equations for computing the step size and search direction are given in section 4.2.2.

4.3.2 Demonstration Examples

In this section, the above derived method is used to estimate the unknown thermal conductivity for each element of a 1D rod and a 3D cubic. For the 1D problem, the heat conduction solver is programmed using MATLAB. Some parametric studies are performed to investigate the effect of the temperature measurement duration, heat source waveform, and heat source frequency on final diagnostic performance. For the 3D problem, commercial software ABAQUS is employed here as the heat conduction solver. User subroutine UEL for the 3D linear brick element DC3D8 is developed to have full control

of the thermal conductivity for each element. Details will be discussed below.

4.3.2.1 A 1D Example and Parametric Studies

A simple 1D problem is introduced here to illustrate the feasibility of the thermal conductivity method. The material properties of the rod is chosen to be identical with that shown in Table 4.1. The rod is discretized into 10 elements. The thermal conductivity values of the second the eighth elements are assumed to be 0.3, which are used to simulate the damaged locations on the 1D rod. The direct heat conduction is formulated and solved using the finite element method documented in [110]. As mentioned before, the environment temperature is set to be $T_\infty = 0$ ˚C to facilitate the computation. The schematic representation of the rod with two damage elements is shown in Fig. 4.16. The temperature history at the right and left ends is collected for about 14 seconds, which is used for the thermal conductivity estimation (shown in Fig. 4.17(b)).

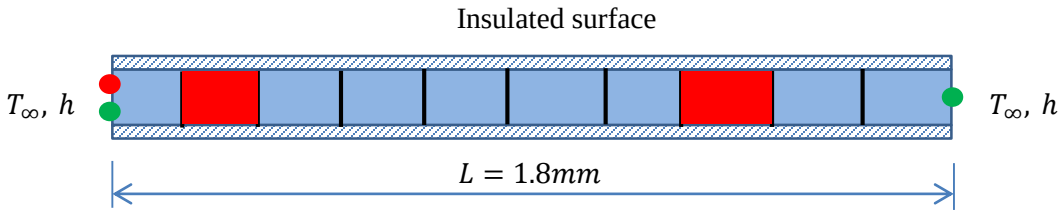

Fig. 4.16 The Schematic Representation of the Rod with Two Damaged Elements

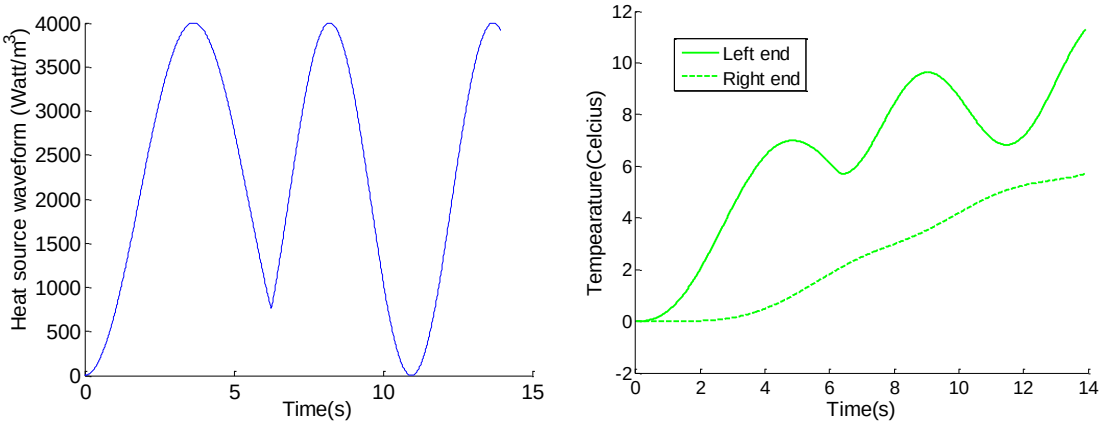

(a) (b)

Fig. 4.17 The Waveform of the Heat Source (a) and

Temperature History at Both Ends (b)

Given the heat source waveform and temperature history measurements, the thermal conductivity for each element can be estimated following the method discussed in section 4.3.1. Initialized with uniform thermal conductivity for all elements, the updated thermal conductivity for each element after every 50 iterations is plotted in Fig. 4.18.

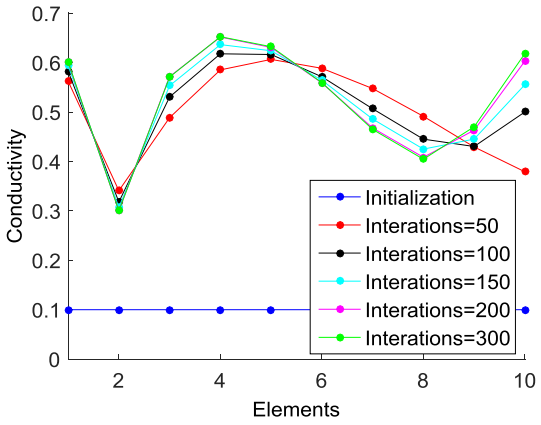

Fig. 4.18 The Estimated Thermal Conductivity for Each Element

From Fig. 4.18, it can be seen that these two damaged elements can be identified by two valleys. The estimated conductivity value for the eighth element doesn't reach 0.3 because the heat source is applied on the left end, which are relatively far away from this damaged element.

In the example above, some configuration parameters, such as the heat source waveform, measurement duration, and number of measurement locations are selected conceptually. To comprehensively understand the effect of them on final diagnosis performance, the parametric study is performed on these parameters. With the same

damage assumption shown in

, the final estimated conductivity using different heat source waveforms is illustrated in Fig. 4.17. The effect of the collected measurement duration on the final diagnosis results is given in Fig. 4.20. Currently, only two measurement locations on both ends are assumed. If there are different number of evenly spaced measurement locations, the final estimated conductivity for each element is plotted in Fig. 4.21.

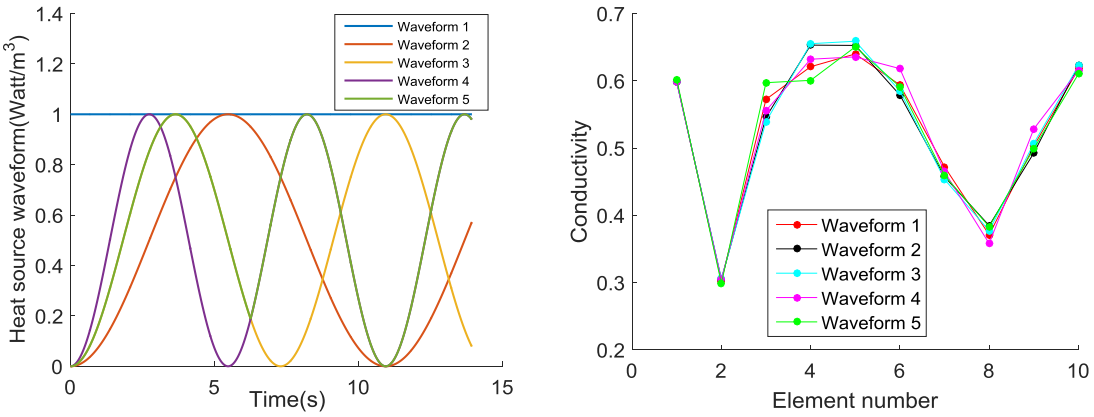

(a) (b)

Fig. 4.19 Heat Source Waveforms (a) and Final Estimated Conductivity for Each Waveform (b)

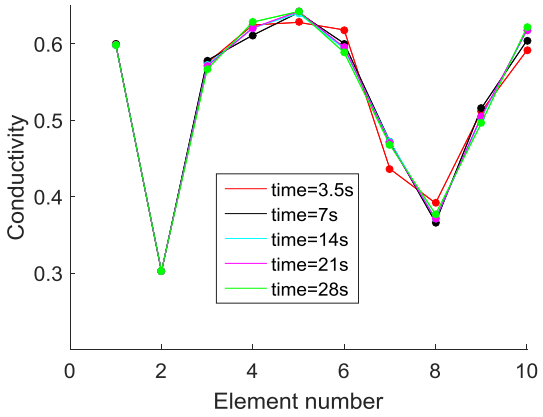

Fig. 4.20 The Estimated Conductivity for Different Measurement Durations

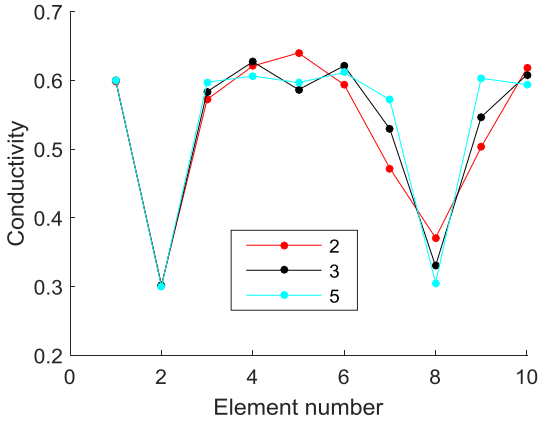

Fig. 4.21 The Estimated Conductivity for Different Number of Measurement Locations

From those three figures above, it can be concluded that the changes of heat source waveform doesn't have significant effect on the final diagnosis performance. As long as it is not too short, no obvious improvement can be observed when changing the measurement duration. However, the diagnosis performance is clearly improved when increasing the number of measurement locations.

4.3.2.2 A 3D Example

In this example, internal damage is simulated using some elements with reduced thermal conductivity inside a stainless steel A304 cubic (illustrated in Fig. 4.22). The thermal properties of the stainless steel are identical with that listed in Table 4.2. Since waveform doesn't have much effect the final diagnosis results, it is assumed to be waveform 1 in Fig. 4.9(a). The heat flux is applied on the bottom surface. Meanwhile, the temperature history measurements on the top and bottom surfaces are collected. The direct and adjoint problems of the heat conduction are solved using the commercial finite element (FE) software ABAQUS. The element conductivity is specified using ABAQUS user subroutine UEL. Following the same procedure discussed before, the thermal conductivity for each element can be estimated using the IHC framework. After optimization, the

estimated conductivity values for all elements are plotted using OVITO 3D visualization software [111]. The final reconstructed damage imaging is illustrated in Fig. 4.23. The color bar included in Fig. 4.22 indicates the value of the thermal conductivity.

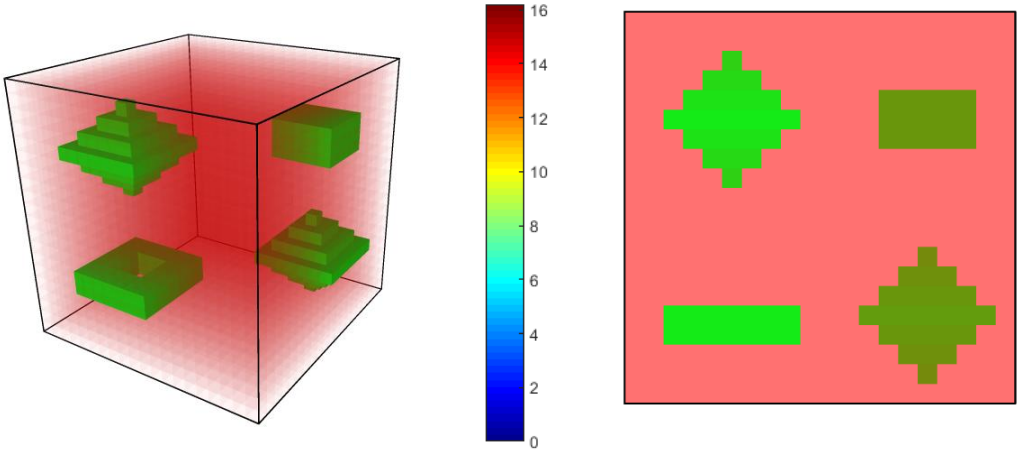

(a) (b)

Fig. 4.22 The 3D View (a) and X-Z Projection (b) of the Simulated True Damage

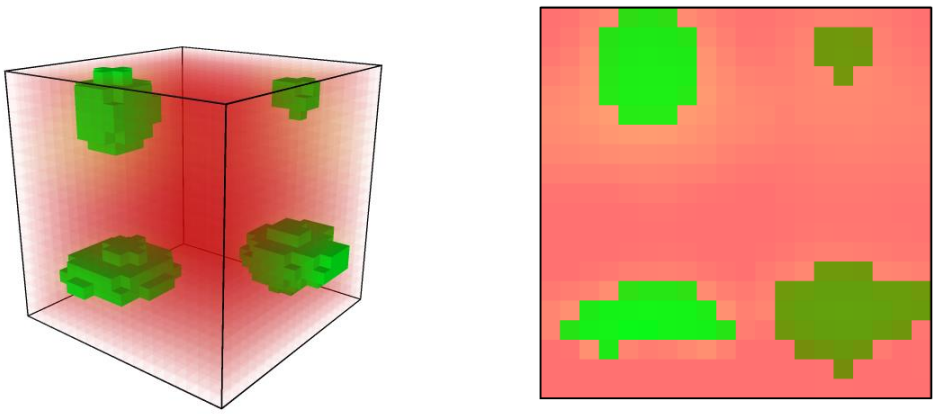

Fig. 4.23 The Reconstructed Damage Imaging

From above figures, it can been seen that the damage location can be approximately estimated with measurements on the top and bottom surfaces, but the accurate profiling about the damage can't be achieved. Currently, it takes very long time for 3D damage reconstruction and most portion of the computational efforts are spent on the heat

conduction simulation. Extra work is needed for solving the heat conduction problem more efficiently.

4.4 Modulus Diagnosis for Wave Propagation Problems

In section 3.5, it has been demonstrated that the damage accumulation in materials will lead to stiffness/modulus degradation, which can highly affect the physics of elastic wave propagation. Following the similar procedure of thermal conductivity estimation using IHC, the material modulus detection using wave propagation can be derived by replacing the heat conduction equation with the elastic wave propagation governing equation. It is assumed there are embedded sensors that can measure the x-y nodal displacement of 2D plates. That is a reasonable hypothesis, because PZT sensors are currently widely used for damage diagnosis and they can covert strain (displacement gradient) into electrical potential which can be measured easily. The piezoelectric effect is not considered in this framework. The formulation for modulus diagnosis is briefly discussed and parametric studies are performed to investigate the detection algorithm performance for different parameters.

4.4.1 Problem Formulation for Modulus Diagnosis

Based on the finite element method, the dynamic response of materials can be modeled as

$$M\ddot{u}(t,P) + K(P)u(t,P) - f(t) = 0 \tag{4-41}$$

where M is the mass matrix, $K(P)$ is the stiffness matrix, $u(t,P)$ is the vector for nodal displacement, $\ddot{u}$ is the second order time derivative of displacement vector. P is the vector consisting of the modulus of each element and $f(t)$ is the applied time dependent dynamic loading.

It can be seen that the above dynamic governing equation has almost the same form with that of the heat conduction problem. Thus, all the derivation discussed above can be applied to derive the objective function gradient with respect to the element modulus, which is eventually given as

$$\frac{\partial F(\mathrm{P})}{\partial \mathrm{P}} = \int_{t=0}^{t_f} \varphi^T \frac{\partial K(\mathrm{P})}{\partial \mathrm{P}} u(t,P)dt \tag{4-42}$$

where φ means the nodal displacement solution for the adjoint problem. Given the discussion in section 4.3.1, it is trivial to derive the above formula. Thus, the detailed procedures are omitted here for simplicity and clarity.

4.4.2 Demonstration Examples

4.4.2.1 Modulus Diagnosis of 2D Plates

In this section, examples are given to demonstrate the shear modulus detection for ultrasonic wave propagation. The dimension (100×100mm) of the 2D plate and the sensor network layout is given in Fig. 4.24. The 2D plates is assumed to be made of aluminum. The red dot represents the ultrasonic signal actuator and the green ones are the sensors that can collect displacement measurements along x and y directions. These sensors are numbered from left to right as 1--14. Dynamic concentrated loading along y direction is applied on the signal actuator and its waveform is illustrated in Fig. 4.25. Clamped boundary condition is applied on the bottom edge marked as blue.

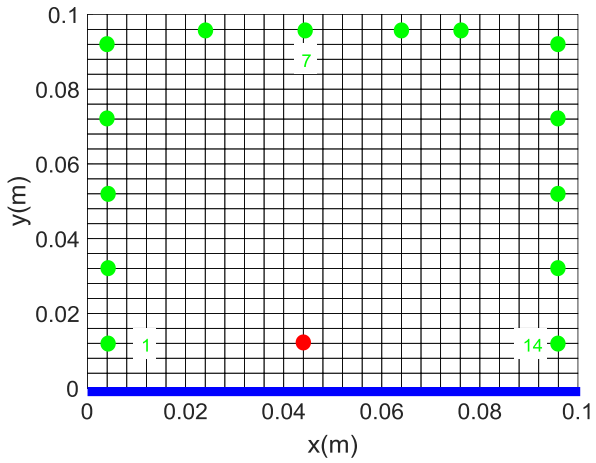

Fig. 4.24 The Dimension and Sensor Network Layout

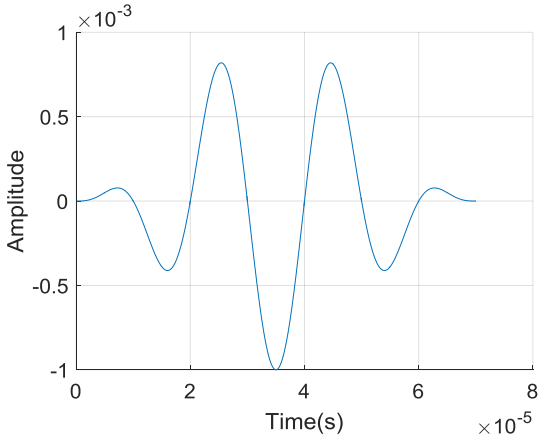

Fig. 4.25 A Tone Burst Signal of 3.5 Cycles with 50 kHz Central Frequency

Damage on the 2D plate is simulated using certain elements with reduced Young's modulus. The nodal temperature solution for the direct and adjoint problems are essential for computing the gradient with respect to unknown parameters. The dynamic problem can be solved using any finite element/ finite difference solver selected by the investigator. In this study, the dynamic analysis code documented in [115] is employed to solve the governing equation (4-41). The simulation is run for $80\mu s$ and at the same time, the measurements at all sensor locations are collected. The displacement measurements at selected sensor locations are plotted in Fig. 4.26. After the simulation, the true and

reconstructed damage images for 2 examples are shown in Fig. 4.27 and Fig. 4.28, respectively.

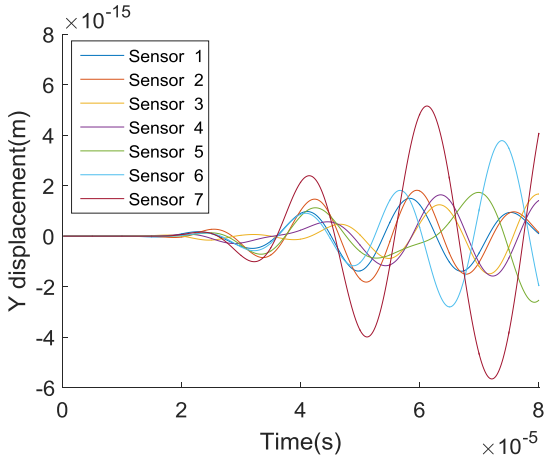

Fig. 4.26 The Y Displacement for Selected Sensors

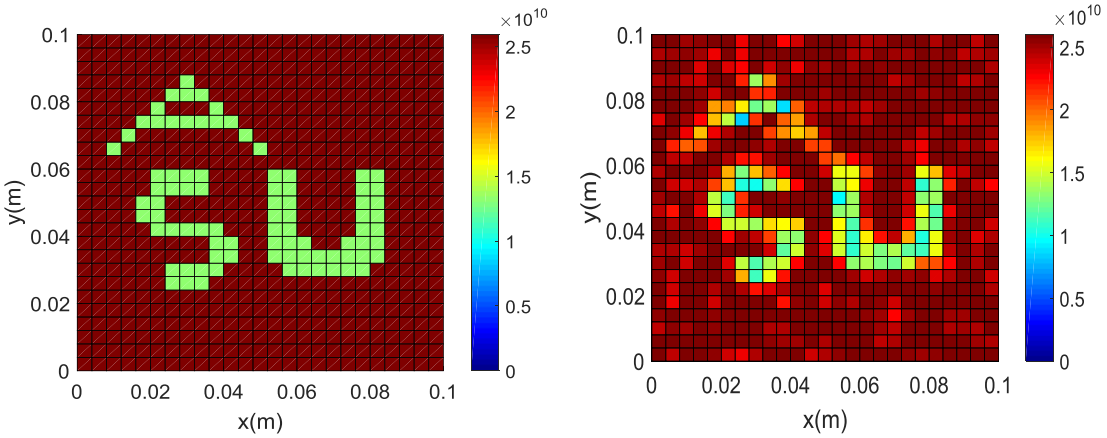

(a) (b)

Fig. 4.27 The True (a) and Reconstructed (b) Damage Images for Example 1

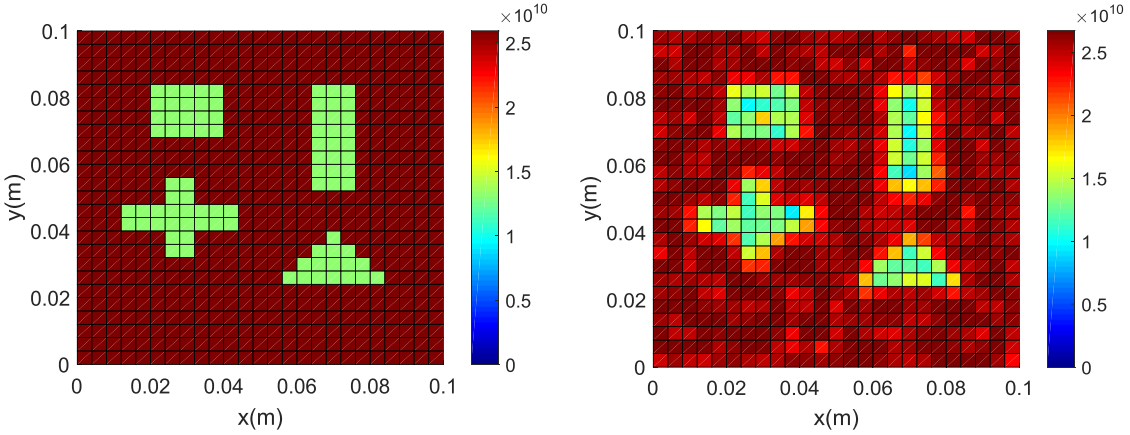

(a) (b)

Fig. 4.28 The True (a) and Reconstructed (b) Damage Images for Example 2

In example 1, the undamaged area is enclosed by damaged elements, which is not common in real practice. It is only used to show the efficacy of this developed method. The driving force for minimizing the objective function is the effect of damage on final nodal displacement measurements. For letter 'A', only one layer of damaged elements are assumed and they don't have significant effect on the received temperature measurements. In the second example, the damage shapes shown in Fig. 4.28 are the most common damage patterns encountered in practice. It can be seen that all the damage areas can be clearly identified.

In order to quantitatively substantiate the reconstructed results, the correlation coefficient between the true and reconstructed damage images is computed and shown in Fig. 4.29. It can be seen that over 70% reconstruction can be achieved after 100 iterations. Within 2000 interactions, around 80% and 90% of the true damage can be reconstructed for example 1 and example 2, respectively.

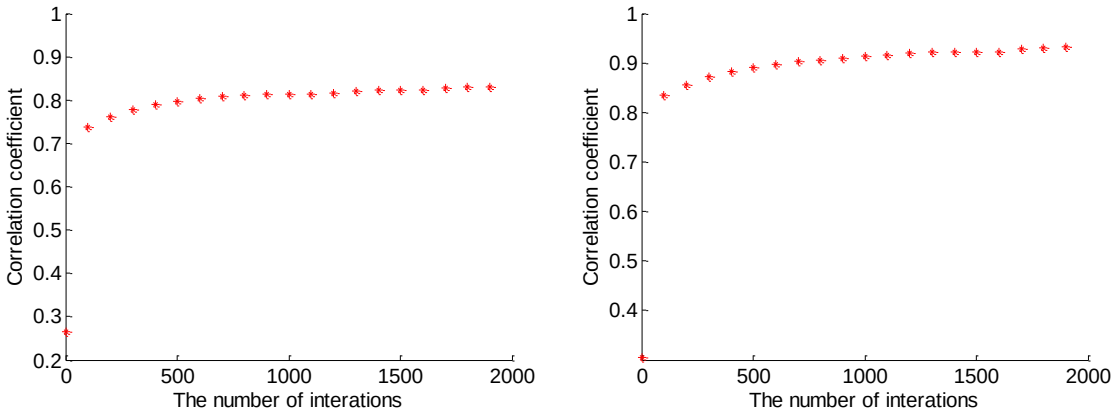

(a) (b)

Fig. 4.29 The Correlation Coefficient for (a) Example 1 and (b) Example 2

4.4.2.2 Parametric Studies

In this section, the effect of several simulation configurations, such as the measurement duration, number of measurement sensors, and measurement noise will be investigated to have a comprehensive understanding of the damage detection algorithm. The damage patterns in example 2 is used in the parametric study. The matrix for the parametric studies can be summarized in Table 4.4. The damage configuration in example 2 is used throughout the parametric studies.

Table 4.4. The Matrix for the Parametric Studies

Parametric studies	Duration(μs)		# of sensors		Noise level(%)			
Duration	40	120	80		80			
# of sensors	13		4	7	13			
Noise level	0		0		2.5	5	7.5	10

Measurement duration effect

Since the efficiency of the algorithm is controlled by the dynamic simulation solver, the collected measurement duration is investigated initially. The idea is to see if similar diagnosis performance is achieved if the simulation is run for a shorter time duration. The displacement measurements of selected sensors for different measurement durations are

shown in Fig. 4.30.The corresponding final reconstructed damage images are compared in Fig. 4.31. The corresponding correlation coefficient is plotted in Fig. 4.32.

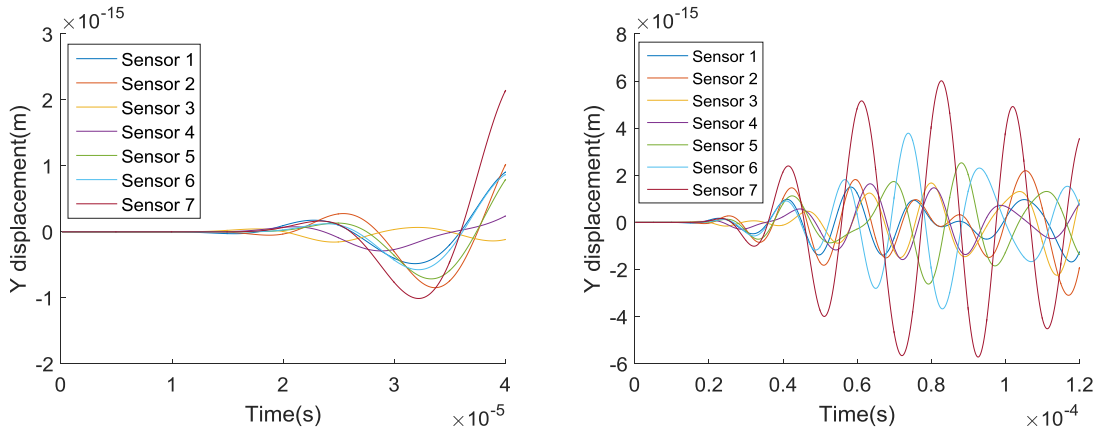

Fig. 4.30 The Y Displacement of Selected Sensors Measured for 40 μs(a) and 120 μs (b)

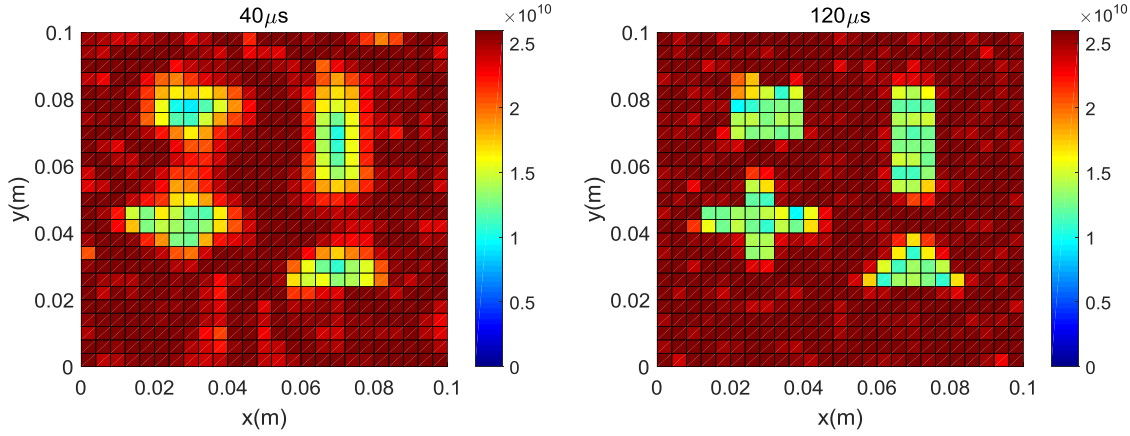

Fig. 4.31 The Reconstructed Damage Images for Difference Measurement Durations

Combining Fig. 4.28(b) and Fig. 4.31, it can be concluded that the contrast of the reconstructed multiple damage is increased when increasing the measurement duration, which can also be substantiated using the correlation coefficient results shown in Fig. 4.32. Given the sensor network layout in Fig. 4.24, there will be reflected waves when the displacement is collected for 120μs. The detection result also means that the reflected

waves will not affect the performance of the algorithm, which is superior to the classical wave propagation-based damage detection method.

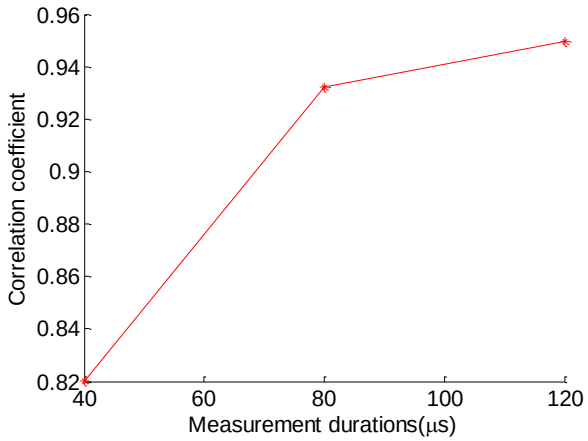

Fig. 4.32 The Correlation Coefficient for Different Measurement Durations

Number of sensors effect

The accessible locations of engineering components are usually limited or restricted in practice. Therefore, the number of sensors used for collecting the displacement measurements is changed and the corresponding the diagnosis performance is compared here. The number of sensors is reduced to 7 and 4 and they are placed evenly spaced along the plate edges shown in Fig. 4.33. The final reconstructed damage images for these two configurations are compared in Fig. 4.34. The corresponding correlation coefficient is shown in Fig. 4.35. Over 80% of the true damage can be identified and reconstructed using only 4 sensors located at corners. However, higher contrast and resolution is observed if more sensors are used.

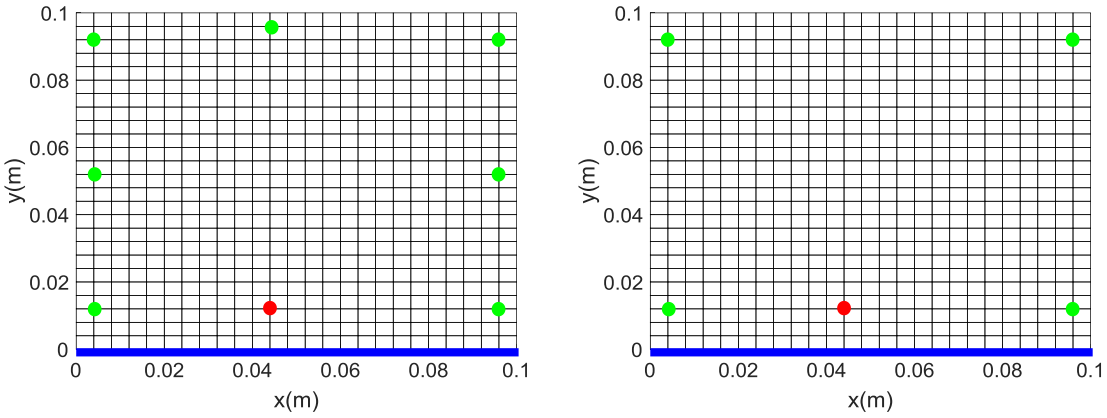

(a) (b)

Fig. 4.33 The Network Layout for 7 Sensors (a) and 4 Sensors (b)

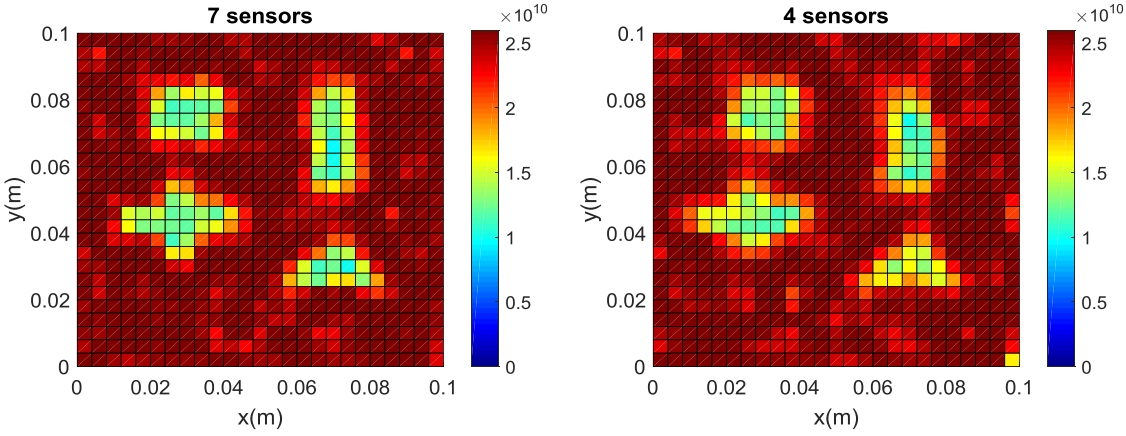

Fig. 4.34 The Reconstructed Damage Images for 7 Sensors (a) and 4 Sensors (b)

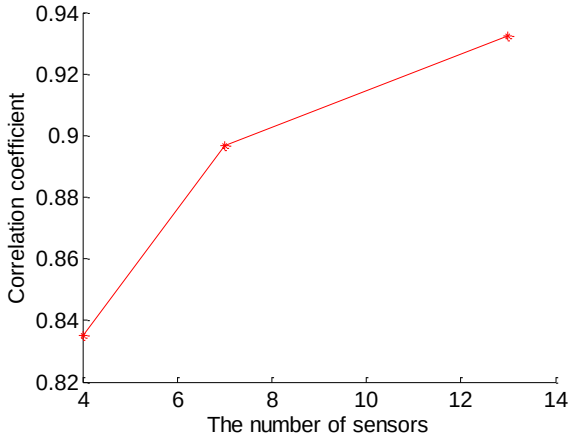

Fig. 4.35 The Correlation Coefficient for Different Number of Sensors

Measurement noise effect

Additionally, true sensor measurements are directly used above to estimate the modulus of each element. However, sensor measurements are usually corrupted with noise in real applications. To investigate the measurement noise effect, the collected temperature measurements are added with Gaussian random noise. The y displacement measurements with $10\% \times 10^{-15}$ Gaussian random noise are plotted in Fig. 4.36. The amplitude of the noise is varied and the corresponding damage detection performance is compared and demonstrated in Fig. 4.37. The corresponding correlation coefficient for different levels of noise is illustrated in Fig. 4.38.

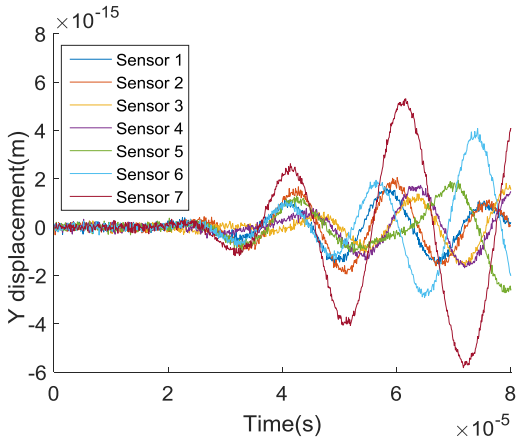

Fig. 4.36 The Y Displacement with 10% Gaussian Noise for Selected Sensors

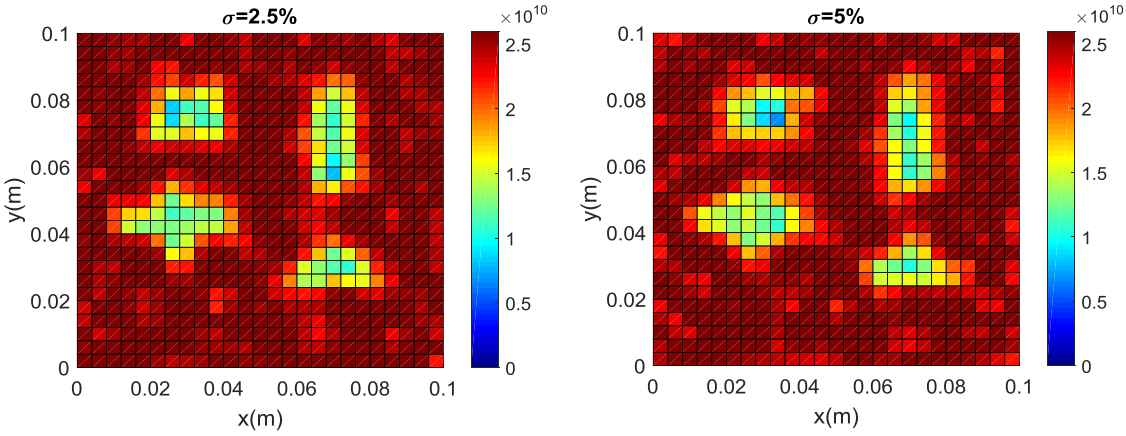

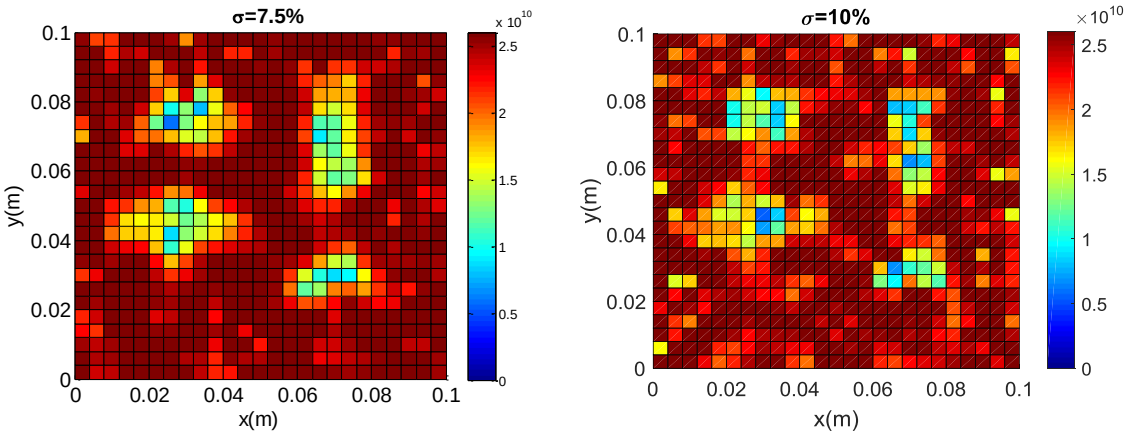

Fig. 4.37 The Reconstructed Damage Images for Different Levels of Noise

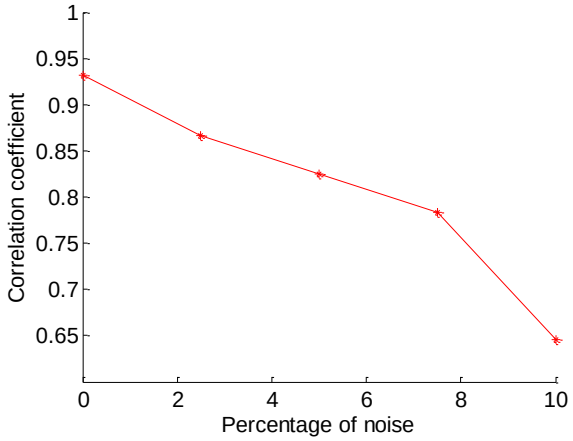

Fig. 4.38 The Correlation Coefficient for Different Levels of Noise

From Fig. 4.37, it can be seen that the shapes of multiple damage can be detected when the noise level is less than 10%. As shown in Fig. 4.38, the damage reconstruction ability is decreasing with the increased level of noise. However, in practice, each sensor can be used for actuating the signal the others are used for collecting the displacement response. Each simulation run can be performed for each actuator-sensor configuration. By taking the average of different simulation runs, the effect of the noise can be cancelled or minimized. The reconstructed results for taking the average of different number of simulation runs are shown in Fig. 4.39.

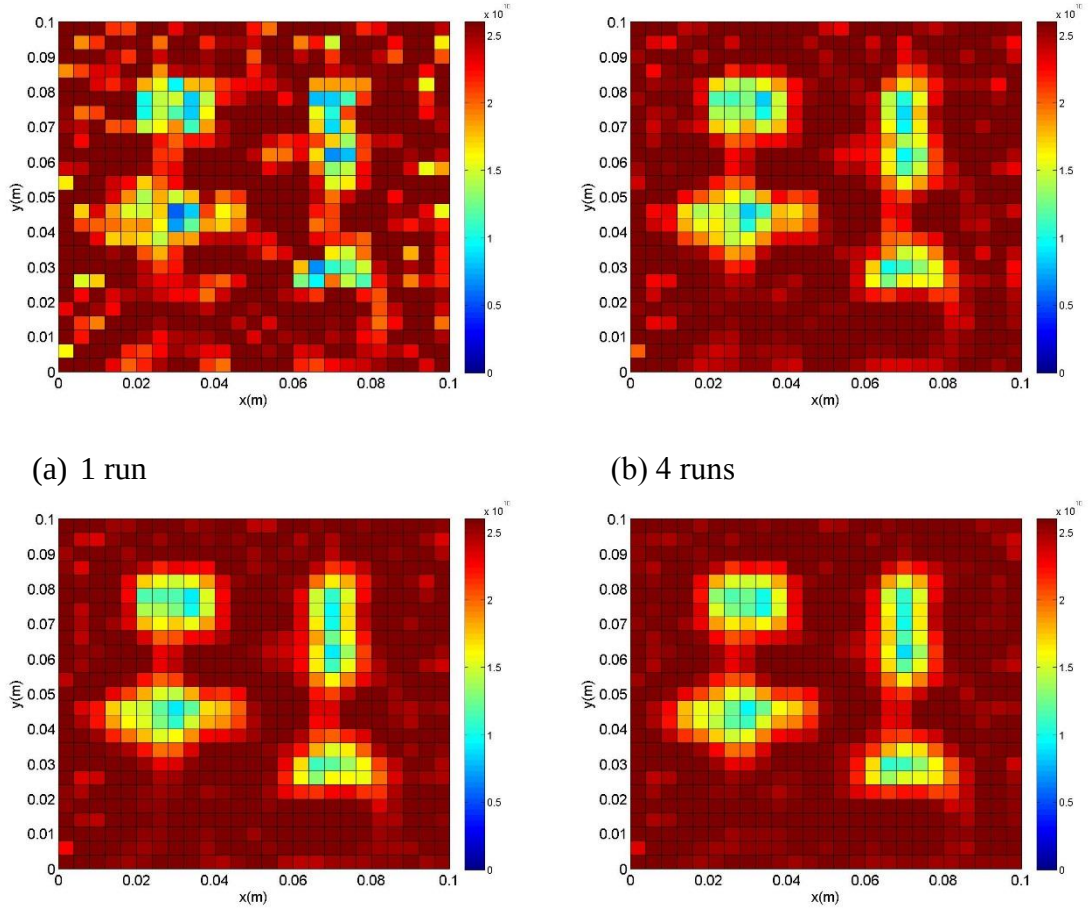

(a) 1 run (b) 4 runs

(c) 8 runs (d) 12 runs

Fig. 4.39 The Reconstructed Results for Taking the Average of Different Number of Simulation Runs

As shown above, the reconstructed damage image becomes clearer and closer to the true damage by taking the average of more simulation runs. Other methods such as filter algorithms can also be used to reduce the level of noise before plugging into the optimization algorithm. Generally, the inverse method is quite noise sensitive, thus the noise level should be carefully controlled in order to achieve optimal detection performance.

4.5 Conclusions

In this chapter, the damage diagnosis problem is considered in other perspectives, such as heat source locations detection, thermal conductivity detection, mechanical modulus detection. With these assumptions, the adjont method is employed to show the feasibility of damage detection of arbitrary configurations (i.e. shape and location).

A novel inverse heat conduction framework is proposed for 3D crack-like damage diagnosis. This method is successfully applied on fish-eye crack and delamination damage detection. Accurate damage detection can be achieved both in plane and along the thickness direction locations using the HC formulation. From the probabilistic point of view, the proposed mean location identification is insensitive to the discretization of the reconstruction. Measurement noise has little effect on the mean damage location identification, but it will impact the confidence bound prediction for the detected damage.

The derivation for thermal conductivity detection is provided based on the finite element method in heat conduction analysis. For thermal conductivity detection, the algorithm is not sensitive to the heat source waveform and collected measurement duration, but the diagnosis contrast is highly dependent on the number of measurement locations. It can be seen that increasing the measurement locations can highly improve the diagnosis accuracy. A 3D example is given to demonstrate the feasibility of this method for complex internal damage reconstruction.

The derivation of the material modulus detection is similar with that of the thermal conductivity detection. Damage detection with multiple locations and shapes is achieved by considering the physics of elastic wave propagation, which improves the flexibility and detection ability of the classical wave propagation-based damage detection method. With

increased level of Gaussian random noise, the reconstructed damage image contrast is reduced. Similar detection trend can be observed when decreasing of the number of measurement sensors, but satisfactory results are achieved using only limited number of sensors. Therefore, in order to achieve the optimal diagnosis performance, the noise level should be carefully controlled and more sensors should be used if possible.

5 CONCLUSIONS AND FUTURE WORK

5.1 Significant Contributions

Based on current investigation, the research objectives proposed at the beginning of the dissertation are achieved, but some promising future research directions are also generated. The significant contributions of this dissertation can be summarized below.

Firstly, an integrated fatigue damage diagnosis and prognosis methodology for lap joints has been proposed, which combines a piezoelectric sensor network-based damage detection method, a physics-based fatigue crack propagation model, and a Bayesian updating framework. The uncertainties of the feature integration model, physics model parameters, system response measurements are incorporated. The feature integration model should be carefully selected and it has significant effect on the final diagnosis performance. Satisfactory results are achieved for fuselage lap joints remaining useful life (RUL) prognosis based on the validation of the prognosis metrics. The discussed deterministic Lamb wave-based damage detection method is extended for crack size and location diagnosis. The proposed method is demonstrated using the datasets from finite element method with different damage configurations. It can provide accurate prediction for both centered crack and random crack location cases.

Secondly, the co-simulation framework for finite element method is developed to simultaneously include the effect of both delamination and matrix cracking using Lamb wave propagation within composites. The simulation results are quantitatively compared with the experimental results for validation. Based on the simulation results, the effect of delamination and matrix cracking must be simultaneously included in a FEM simulation in order to fully quantify the changes in the wave signal observed from experiments. The

normalized amplitude change, correlation coefficient, and phase change are shown to be good candidates for the damage detection in composite plates, both numerically and experimentally. Gaps between matrix cracks (crack density), crack lengths, and delamination size have significant effect on the received signal and, therefore, should be estimated accurately.

Thirdly, a new probabilistic damage size and location updating algorithm is proposed, which incorporates the Lamb wave-based signal features into the Bayesian updating framework. The proposed Bayesian Imaging Method can simultaneously estimate the damage size and location information and their uncertainty bonds. The uncertainty bonds get stabilized after about 6~8 updating points. This method is also proved to be applicable to multiple specimens with very different feature trends. To predict the RUL of composite materials, an efficient overall stiffness degradation model is incorporated in Bayesian inference for fatigue life prognosis. The proposed stiffness degradation model is able capture the general trend of the overall stiffness reduction of open-hole specimens. With this model, the complexity of incorporating the detailed damage information in RUL prediction can be avoided and the computation effort is highly reduced for Bayesian inference. This proposed framework is demonstrated and validated using the experiment testing results of open-hole specimens.

Finally, damage detection problems are considered from new perspectives, such as heat source locations detection, material properties detection. Efficient computation of the objective function gradient is achieved by employing the adjoint method. Using ultrasonic transducer excitation, the proposed crack-like damage detection method shows satisfactory performance for both in plane and out of plane damage detection. Increasing the random

noise level will increase confidence bound prediction of the thickness direction profiling, but it can provide almost identical mean prediction. For thermal conductivity detection, increasing the measurement locations will highly improve the diagnosis accuracy. On the contrary, the heat source waveform and collected measurement duration show much less effect on the diagnosis results. For modulus detection, similar diagnosis performance trend is observed when changing the number of measurement locations. The reconstructed damage shows improved contrast when increasing the collected measurement duration, which also means that the reflected waves from the boundaries have no effect on the detection algorithm. With higher random noise level, the reconstructed damage images show reduced contrast as well as the diagnosis accuracy.

5.2 Future Work

Currently, an integrated damage diagnosis and prognosis framework has been proposed for both metallic and composite materials. Some promising future research directions can be generated based on current investigation.

Firstly, further efforts are needed for more general crack growth model of metallic materials, which can predict the crack growth at different locations considering the interaction between cracks.

Secondly, more studies are necessary to develop an efficient damage evolution model of composites, which allows the incorporation of true delamination and matrix cracking diagnosis for more accurate future remaining useful life prognosis.

Thirdly, large uncertainties across different specimens, environment, and manufacturing process should be quantified and considered for RUL prognosis.

Finally, it requires at least several hundreds of iterations to get satisfactory diagnosis performance for the adjoint method-based damage diagnosis. Therefore, the efficiency of the physics problems solver will highly affect the diagnosis efficiency. More studies are required to solve the governing equations more efficiently, such as from frequency domain.

REFERENCES

1. Mielozyk, M., et al., *Active therography method for delamination detection and localisation in composite structures.* 6th European Workshop on Structural Health Monitoring 2012.

2. Koruk, M. and M. Kilic, *The usage of IR thermography for the temprature measurements inside an automobile cabin.* International Communication in Heat and Mass Tansfer 2009. **36**: p. 872-877.

3. Kazys, R. and L. Svilainis, *Ultrasonic detection and characterization of delaminations in thin composite plates using signal processing technique.* Ultrasonics, 1997. **35**: p. 367-383.

4. Nicolleto, A. and K. Hola, *X-ray computed tomography vs. metallography for pore sizing and fatigue of cast Al-alloys.* Pocedia Engineering, 2010. **2**(1): p. 8.

5. Grimberg, R., et al., *Eddy current holography evaluation of delamination in carbon-epoxy composites.* Insight, 2001. **43**(4): p. 260-264.

6. Sophian, A., et al., *Electromag-netic and eddy current NDT: a review.* Insight, 2001. **43**(5): p. 302-306.

7. Raghavan, A. and C.E.S. Cesnik, *Review of guided-wave structural health monitoring.* . Shock and Vibration Digest, 2007. **39**(2): p. 91-116.

8. Su, Z. and L. Ye, *Identification of damage using Lamb waves: From fundamentals to applications.* London: Springer-Verlag GmbH & Co., 2009: p. 346.

9. Zhou, C., et al., *Evaluation of fatigue cracks using nonlinearities of acousto-ultrasonic waves acquired by an active sensor network.* Smart materials and structures, 2013. **22**(1): p. 015018.

10. He, J., et al., *A multi-feature integration method for fatigue crack detection and crack length estimation in riveted lap joints using Lamb waves* Smart Materials and Structures, 2013. **22**(10): p. 105007.

11. Dempster, A., *A generation of Bayesian inference.* Classic Works of the Dempster Shafer Theory of Belief Functions, 2008: p. 73-104.

12. Box, G. and G. Tiao, *Bayesian inference in statistical analysis.* Wiley New Work, 1992.

13. Gilboa, I. and D. Schmeidler, *Updating ambiguous beliefs.* Morgan Kaufmann Publishers Inc, 1992: p. 143-162.

14. Press, S., *Subjective and objective Bayesian statistics: principles, models, and applications.* Wiley-Interscience, Hoboken, NJ, 2003.

15. Caticha, A. and A. Giffin, *Updating probabilities. Bayesian Inference and Maximum Entropy Methods in Science and Engineering.* AIP Conf. Proc, 2006. **31**: p. 872.

16. Au, S.-K. and J.L. Beck, *A new adaptive importance sampling scheme for reliability calculations.* Structural safety, 1999. **21**(2): p. 135-158.

17. Gelman, A. and X. Meng, *Simulating normalizing constants: From importance sampling to bridge sampling to path sampling.* Statistical science, 1998. **13**(2): p. 163-185.

18. Melchers, R.E., *Importance sampling in structural systems.* Structural safety, 1989. **6**(1): p. 3-10.

19. Neal, R., *Annealed importance sampling.* Statistics and Computing, 2001. **11**(2): p. 125-139.

20. Hasting, W.K., *Monte Carlo sampling methods using Markov Chain and their applications.* Biometrika, 1970. **57**: p. 97-109.

21. Metropolis, N., et al., *Equations of State Calculations by Fast Computing Machines.* Journal of Chemical Physics 1953. **21**(6): p. 1087-1092.

22. Green, P.J. and A. Mira, *Delayed rejection in reversible jump Metropolis-Hastings.* Biometrika, 2001b. **88**: p. 1035-1053.

23. Mira, A., *On Metropolis-Hastings algorithm with delayed rejection.* Metron, 2011a. **LIX**(3-4): p. 231-241.

24. Haario, H., E. Saksman, and J. Tamminen, *An adaptive Metropolis algorithm.* Bernoulli, 2001. **7**: p. 223-242.

25. Tierney, L. and A. Mira, *Some adaptive Monte Carlo methods for Bayesian inference.* Statistics in Medicine, 1999. **18**: p. 2507-2515.

26. Haario, H., et al., *DRAM: Efficient adaptive MCMC.* Statistics and Computing 2006: p. 339-354.

27. Scalea, d., et al., *Guided wave ultrasonics for NDE of aging aircraft components* Proc. SPIE, 2002. **4704**: p. 123-32.

28. Sun, K., et al., *Damage Identification in Thick Steel Beam Based on Guided Ultrasonic Waves.* Journal of Intelligent Material Systems and Structures, 2010.

21(3): p. 225-232.

29. Park, G., et al., *Performance assessment and validation of piezoelectric active-sensors in structural health monitoring.* Smart materials and structures, 2006. **15**: p. 1673.

30. Lowe, M. and O. Diligent, *Low-frequency reflection characteristics of the s Lamb wave from a rectangular notch in a plate.* The Journal of the Acoustical Society of America, 2002. **111**: p. 64-74.

31. Raghavan, A. and C.E.S. Cesnik, *Review of guided-wave structural health monitoring.* Shock and Vibration Digest, 2007. **39**(2): p. 91-116.

32. Zhao, X., et al., *Active health monitoring of an aircraft wing with embedded piezoelctric sensor/actuator network:I.Defect detection, localization and growth monitoring* Smart MATER. STRUCT., 2007. **16**(1208-17).

33. Wang, Q. and S. Yuan, *Baeline-free imaging method based on new pzt sensor arrangements.* Journal of Intelligent Material Systems and Structures, 2009. **20**(1663-1673).

34. SU, Z. and L. Ye, *Identification of damage using Lamb waves.* Springer, 2009. **LNACM 48**: p. 195-254.

35. Rasmussen, C.E. and C.K.I. Williams, *Gaussian Process for Machine Learning.* The MIT press, 2006.

36. Ebden, M., *Gaussian Processes for Regression.* 2008.

37. Dietrich, F. and C. List, *Reasons for (Prior) belief in Bayesian epistermology.* Synthese, 2013. **190**: p. 787-808.

38. Adam, M.T., *G104-A2L Guide for estimation of measurement uncertainty in testing.* American Association of Laboratory Accreditation Manual, 2002: p. 10-18.

39. Bell, S., *A Beginner's Guide to Uncertainty of Measurement.* The National Physical Laboratory, 2001. **2**: p. 9-16.

40. Cowles, M.K. and B.P. Carlin, *Markov Chain Monte Carlo Convergence Diagnostics: A Comparative Review.* Journal of the American Statistical Association, 1996. **91**(434).

41. Fort, G., E. Moulines, and P. Priouret, *Convergence of adaptive and interacting Markov chain Monte Carlo algorithms.* Annals of Statistics, 2012. **39**(6): p. 3262-3289.

42. Peskun, P.H., *Aptimum Monte Carlo sampling using Markov chains.* Biometrika, 1973. **57**: p. 97-109.

43. Yibing, X. and L. Yongming, *An equivalent stress level model for efficient fatigue crack growth prediction*, in *52nd AIAA/ASME/ASCE/AHS/ASC Structures, Structural Dynamics and Materials Conference*. 2011, American Institute of Aeronautics and Astronautics.

44. Liu, Y. and S. Mahadevan, *Probabilistic fatigue life prediction using an equivalent initial flaw size distribution.* International Journal of Fatigue, 2009. **31**(3): p. 476-687.

45. hijazi, A.L., B.L. Smith, and T.E. Lacy, *Linkup strength of 2024-T3 bolted lap joint panels with multiple-site damage.* Journal of Aircraft, 2004. **41**(2): p. 359-364.

46. Saxena, A., et al., *Metrics for evaluating performance of prognostic techniques.* In Aerospace conference, 2009 IEEE, 2008: p. 1-13.

47. Guan, X., et al., *Comparison of Two Probabilistic Fatigue Damage Assessment Approaches Using Prognostic Performance Metrics.* International Journal of prognositics and health management, 2011. **2**(1): p. 11.

48. Saxena, A., et al., *Uncertainty Quantification in Fatigue Crack Growth Prognosis.* International Journal of prognositics and health management, 2011. **2**(1): p. 15.

49. Saxena, A., et al., *Metrics for Offline Evaluation of Prognostic Performance.* international Journal of prognositics and health management, 2010. **1**(1): p. 20.

50. Huang, G., F. Song, and X. Wang, *Quantitative Modeling of Coupled Piezo-Elastodynamic Behavior of Piezoelectric Actuators Bonded to an Elastic Medium for Structural Health Monitoring: A Review.* Sensors, 2010. **10**: p. 3681-3702.

51. Yang, C., et al., *Some aspects of numerical simulation for Lamb wave propagation in composite laminates.* Composite Structures, 2006. **75**: p. 267-275.

52. Samaratunga, D. and R. Jha, *Lamb wave propagation simulation in smart composite structures.* 2012 SIMULIA Community Conference, 2012.

53. Zhigun, I.G. and V.V. Mikhailov, *Tensile testing of high-strength unidirectional composites.* Polymer Mechanics, 1978. **14**(4): p. 586-591.

54. Lucas, R. and H. Danford, *Case Studies: Low Cost, High-Strength, Large Carbon Foam Tooling.* SMPLE Journal, 2009. **45**(1).

55. Halverson, D.C., et al., *Processing of Boron Carbide-Auminum Composites.* J. Am. Ceram. Soc. , 1989. **72**(5): p. 775-80.

56. Manocha, L.M., *High performance carbon-carbon composites.* Sadhana, 2003. **28**: p. 349-358.

57. di Scalea, F.L., et al., *Guided-wave ultrasonics for NDE of aging aircraft components.* 2002: p. 123-132.

58. Diamanti, K. and C. Soutis, *Stuctural health monitoring techniques for aircraft composite structures.* Progress in Aerospace Sciences, 2010. **46**: p. 342-352.

59. Ben, B.S., et al., *Damage identification in composite materials using ultrasonic based Lamb wave method.* Measurement, 2013. **46**: p. 904-912.

60. Kessler, S.S., S.M. Spearing, and C. Soutis, *Damage detection in composite material using Lamb wave methods.* Smart materials and structures, 2002. **11**: p. 269-278.

61. *Scattering characteristics of Lamb waves from debondings at structural features in composite laminates.* The Journal of the Acoustical Society of America, 2012. **132**(1): p. 115.

62. Ramadas, C., et al., *Interaction of the primary anti-symmetric Lamb wave A0 with symmetric delamination: Numerical and experimental studies.* Smart Materials and Structures, 2009. **18**(1-7).

63. Islam, A.S. and K.C. Craig, *Damage detection in composite structures using piezoelectric materials.* Smart Mater. Struct., 1994. **3**: p. 318-328.

64. Sause, M.G.R., M.A. Hamstad, and S. Horn, *Finite element modeling of lamb wave propagation in anisotropic hybrid materials.* Composite Part B, 2013. **53**: p. 249-257.

65. Wang, L. and F.G. Yuan, *Lamb wave propagation in composite laminates using a higher-order plate theory.* Proc. SPIE, 2007: p. 10I.1–10I.12.

66. Kang, K.-T., et al., *Damage Detection of Composite Plates Using Finite Element Analysis Based on Structural Health Monitoring.* Journal of Materials Science & Engineering 2011. **1**(B): p. 14.

67. Ke, W., M. Castaings, and C. Bacon, *3D finite element simulation so fan air-coupled ultrasonic NDT system.* NDT&E International, 2009. **42**: p. 524-533.

68. Hosseini, S.M.H. and U. Gabbert, *Numerical simulation of the Lamb wave propagation in honeycomb sandwich panels: A parametric study.* Composite Structures, 2013. **97**: p. 189–201.

69. Hosseini, S.M.H., et al., *Numerical simulation of Lamb wave propagation in*

metallic foam sandwich structures: a parametric study Composite Structures, 2013. **97**: p. 387–400.

70. Nadella, K.S. and C.E.S. Cesnik, *Local interaction simulation approach for modeling wave propagation in composite structures.* CEAS Aeronaut J. , 2013. **4**: p. 35-48.

71. Ruzzene, M., et al., *Simulation and measurement of ultrasonic waves in elastic plates using laser vibrometry.* Review of Progress in QNDE 23 ed D O Thompson and D E Chimenti (American Institute of Physics), 2004.

72. Nixon-Pearson, O.J., et al., *Damage development in open-hole composite specimens in fatigue. Part 2: Numerical modelling.* Composite Structures, 2013. **106**(0): p. 890-898.

73. RINDERKNECHT, S. and B. KROPLIN, *A finite Element Model for Delamination in Composite Plates.* Mechanics of Composite Materials and Structures, 2007. **2**(1): p. 19-47.

74. Keshava Kumar, S., R. Ganguli, and D. Harursampath, *Partial delamination modeling in composite beams using a finite element method.* Finite Elements in Analysis and Design, 2013. **76**(0): p. 1-12.

75. Zhang, J., et al., *Crack initiation and fatigue life prediction on aluminum lug joints using statistical volume element–based multiscale modeling.* Journal of Intelligent Material Systems and Structures 2013. **24**(17).

76. Zhang, J., J. Johnston, and A. Chattopadhyay, *Physics‐based multiscale damage criterion for fatigue crack prediction in aluminium alloy.* Fatigue & Fracture of Engineering Materials & Structures, 2014. **37**(2): p. 119-131.

77. Wu, Q. and M.A. Zikry, *Microstructural modeling of crack nucleation and propagation in high strength martensitic steels.* International Journal of Solids and Structures, 2014. **51**(25–26): p. 4345-4356.

78. Highsmith, A. and K.L. Reifsnider, *Stiffness reduction mechanisms in composite laminates.* In: Reifsnider KL, editor. Damage in Composite Materials. ASTM STP 775. American Society for Testing and Materials, 1982(103-117).

79. Philippidis, T.P. and A.P. Vassilopoulos, *Fatigue design allowable for GRP laminates based on stiffness degradation measurements* Composites Science and Technology, 2000. **60**: p. 2819-2828.

80. Agarwal, B.D. and S.K. Joneja, *Flexural fatigue properties of Unidirectional GRP in the transverse direction.* Composites, 1979. **10**(1): p. 28-30.

81. Ambu, R., F. Aymerich, and F. Bertolino, *Investigation of the effect of damage on the strength of notched composite laminates by digital image correlation.* The Journal of Strain Analysis for Engineering Design, 2005. **40**(5): p. 451-461.

82. Whitworth, H.A., *A stiffness degradation model for composite laminates under fatigue loading.* Composite Structures, 1998. **40**(2): p. 95-101.

83. Yang, J.N., et al., *A stiffness degradation model for Graphite/Epoxy laminates.* Journal of Composite Material, 1990. **24**(753).

84. Shirazi, A. and A. Varvani-Farahani, *A Stiffness Degradation Based Fatigue Damage Model for FRP Composites of (0/θ) Laminate Systems.* Applied Composite Materials, 2010. **17**: p. 137-150.

85. Saxena, A., et al., *Accelerated Aging Experiments for Prognostics of Damage Growth in Composite Materials.* Proceedings of the 8th International Workshop on Structural Health Monitoring, 2011. **1**: p. 1139-1149.

86. Giurgiutiu, V., *Tuned Lamb wave excitation and detection with piezoelectric wafer active sensors for structural health monitoring* J. Intell. Mater. Syst. Struct., 2005. **16**: p. 291-305.

87. Han, S., *Finite element analysis of Lamb wave acting within a thin aluminum plate.* AIR FORCE INSTITUTE OF TECHNOLOGY 2007.

88. Ozisik, M.N. and H.R.B. Orlande, *Inverse Heat Transfer: Fundamentals and Applications.* Talor & Francis, 2000.

89. Caticha, A. and A. Giffin, *Updating probabilities. Bayesian Inference and Maximum Entropy Methods in Science and Engineering.* AIP Conference Proceedings 2006. **31**: p. 872.

90. Peng, T., et al., *A novel Bayesian imaging method for probabilistic delamination detection of composite materials.* Smart materials and structures, 2013. **22**(12): p. 125019.

91. Kurz, J.H., et al., *Reliability considerations of NDT by probability of detection (POD) determination using ultrasound phased array.* Engineering Failure Analysis, 2013. **35**(0): p. 609-617.

92. *ASTM E647-13ae1, Standard Test Method for Measurement of Fatigue Crack Growth Rates, ASTM International, West Conshohocken, PA, 2013, www.astm.org.*

93. Han, X., L.D. Favro, and R.L. Thomas, *Sonic IR Imaging of delaminations and disbonds in composites.* J. Phys. D: Appl. Phys., 2011. **44**: p. 034013.

94. Favro, L.D., et al., *Sonic IR Imaging of Cracks and Delamination.* Analytical Sciences, 2001. **17**: p. 451-453.

95. Mian, A., et al., *Fatigue damage detection in graphite/epoxy composites using sonic infrared imaging technique.* Composites Science and Technology, 2004. **64**: p. 657–666.

96. Zhao, S.X., et al., *Composite delamination depth profiling in sonic-IR imaging.* AIP Conference Proceedings, 2012. **1430**(1): p. 533-539.

97. Beck, J.V., B. Blackwell, and C.R.S.C. Jr., *Inverse Heat Conduction: Ill-Posed Problems.* Wiley-Interscience, Hoboken, NJ, 1985.

98. JARNY, Y., M.N. OZISIK, and J.P. BARDON, *A general optimization method using adjoint equation for solving multidimensional inverse heat conduction.* International Journal of Heat and Mass Transfer, 1991. **34**(11): p. 2911-2919.

99. Huang, C.-H. and Y. Jan-Yuan, *An inverse problem in simultaneously measuring temperature-dependent thermal conductivity and heat capacity.* International Journal of Heat and Mass Transfer, 1995. **38**(18): p. 3433-3441.

100. Shidfar, A., A. Zakeri, and A. Neisi, *A TWO-DIMENSIONAL INVERSE HEAT CONDUCTION PROBLEM FOR ESTIMATING HEAT SOURCE.* International Journal of Mathematics and Mathematical Sciences, 2005. **10**: p. 1633-1641.

101. Su, J. and A.J. Silva Neto, *Two-dimensional inverse heat conduction problem of source strength estimation in cylindrical rods.* Applied Mathematical Modelling, 2001. **25**(10): p. 861-872.

102. Yang, C.-y., *Estimation of the temperature-dependent thermal conductivity in inverse heat conduction problems.* Applied Mathematical Modelling, 1999. **23**(6): p. 469-478.

103. Yang, C.-y., *A linear inverse model for the temperature-dependent thermal conductivity determination in one-dimensional problems.* Applied Mathematical Modelling, 1998. **22**(1–2): p. 1-9.

104. Fichtner, A., H.P. Bunge, and H. Igel, *The adjoint method in seismology: I. Theory.* Physics of the Earth and Planetary Interiors, 2006. **157**(1–2): p. 86-104.

105. Fichtner, A., H.P. Bunge, and H. Igel, *The adjoint method in seismology—: II. Applications: traveltimes and sensitivity functionals.* Physics of the Earth and Planetary Interiors, 2006. **157**(1–2): p. 105-123.

106. Bro, R. and S.D. Jong, *A fast non-negativity-constrained least squares algorithm.* Journal of Chemometrics, 1999. **11**(5): p. 393-401.

107. Kim, D., S. Sra, and I.S. Dhillon, *A New Projected Quasi-Newton Approach for the Nonnegative Least Squares Problem.* Department of Computer Sciences, The University of Texas at Austin, Technical Report # TR-06-54, 2006.

108. Slawski, M. and M. Hein, *Non-negative least squares for high-dimensional linear models: Consistency and sparse recovery without regularization.* 2013: p. 3004-3056.

109. Chen, D. and R.J. Plemmons, *Nonnegativity constraints in numerical analysis.* The Birth of Numerical Analysis, 2009: p. 109-139.

110. Lewis, R.W., et al., *The Finite Element Method in Heat Transfer Analysis.* John Wiley & Sons Ltd., 1996.

111. Alexander, S., *Visualization and analysis of atomistic simulation data with OVITO–the Open Visualization Tool.* Modelling and Simulation in Materials Science and Engineering, 2010. **18**(1): p. 015012.

112. Belytschko, T., W.K. Liu, and B. Moran, *Nonlinear Finite Elements for Continua and Structures.* John Wiley & Sons Ltd., 2000.

113. Logan, D.L., *A First Course in the Finite Element Method.* Boston: PWS Engineering, 1986.

114. S. Reh, F.B., A. Brückner-Foit, and H. Riesch-Oppermann, *First Order Reliability Analysis Using Stochastic Finite Element Methods.* Computational Stochastic Mechanics. Springer Netherlands, 1991: p. 385-394.

115. Bower, A.F., *http://solidmechanics.org/FEA.php*.